

AD-A281 726 TATION PAGE

Form Approved  
OMB No. 0704-0188

1. To average 1 hour per response, including the time for reviewing instructions, searching existing data sources, gathering the collection of information, Send comments regarding this burden estimate or any other aspect of this form, to Washington Headquarters Services, Directorate for Information Operations and Reports, 1215 Jefferson Ave. of Management and Budget, Paperwork Reduction Project (0704-0188), Washington, DC 20503.

DATE

1994-04-25

3. REPORT TYPE AND DATES COVERED

FINAL REPORT 1 May 90 - 31 Dec 93

## 4. TITLE AND SUBTITLE

Optical and Magnetic Resonance Investigations of 3d  
Ions in Single Crystal Hosts: Candidates for Tunable  
Solid-State Lasers

## 5. FUNDING NUMBERS

DAAL03-90-G-0113

## 6. AUTHOR(S)

David J. Singel

## 7. PERFORMING ORGANIZATION NAME(S) AND ADDRESS(ES)

Department of Chemistry President and Fellows of  
Harvard University Harvard College  
12 Oxford Street Office of Sponsored Research  
Cambridge, MA 02138 Holyoke Center, 4th Floor

## 8. PERFORMING ORGANIZATION

REPORT NUMBER

JUL 13 1994

B D

## 9. SPONSORING/MONITORING AGENCY NAME(S) AND ADDRESS(ES)

U. S. Army Research Office  
P. O. Box 12211  
Research Triangle Park, NC 27709-2211

10. SPONSORING/MONITORING  
AGENCY REPORT NUMBER

ARO 27425.5-PH

## 11. SUPPLEMENTARY NOTES

The view, opinions and/or findings contained in this report are those of the  
author(s) and should not be construed as an official Department of the Army  
position, policy, or decision, unless so designated by other documentation.

## 12a. DISTRIBUTION/AVAILABILITY STATEMENT

Approved for public release; distribution unlimited.

## 12b. DISTRIBUTION CODE

## 13. ABSTRACT (Maximum 200 words)

A comprehensive report is presented on EPR and correlated optical spectroscopic studies conducted in our laboratory on a new class of solid-state materials with potential utility as near IR lasers. All of the studied materials involve oxide host lattices (silicates, vanadates, and germanates) doped with 3d transition metal-ions (chromium and manganese). The novelty of the materials is connected to the tetrahedral coordination and unusual oxidation states of the dopant ions. EPR spectroscopy is to determine the elemental identity of the dopant ions, the "spin" of the ions and hence their oxidation numbers, and the crystallographic position of the ion, hence its coordination number. These properties are then attached to relevant optical centers through magnetic resonance correlated optical spectroscopies, such as optical Zeeman spectroscopy. In the Cr:forsterite laser system, our results prove that the near IR lasing center is tetrahedral Cr<sup>4+</sup>. In Mn:Ba<sub>3</sub>(VO<sub>4</sub>)<sub>2</sub> EPR spectroscopy shows that tetrahedral Mn<sup>5+</sup> and Mn<sup>4+</sup> centers are both present in the material; a novel spin-echo pulsed laser double resonance method is introduced to prove that the tetrahedral Mn<sup>5+</sup> is the active center. Previously unpublished results of chromium-doped gehlenites and garnets are also reported.

## 14. SUBJECT TERMS

## 15. NUMBER OF PAGES

184

## 16. PRICE CODE

17. SECURITY CLASSIFICATION  
OF REPORT

UNCLASSIFIED

18. SECURITY CLASSIFICATION  
OF THIS PAGE

UNCLASSIFIED

19. SECURITY CLASSIFICATION  
OF ABSTRACT

UNCLASSIFIED

## 20. LIMITATION OF ABSTRACT

UL

NSN 7540-01-280-3500

Standard Form 298 (Rev. 2-89)  
Prescribed by ANSI Std. Z39-18  
298-102

94 7 12 353

**Optical and Magnetic Resonance Investigations of  
3d Ions in Single Crystal Hosts:  
Candidates for Tunable Solid-State Lasers**

**FINAL REPORT**

**David J. Singel**

**1994-03-25**

**U. S. Army Research Office**

**DAAL03-90-G-0113**

**Harvard University**

**Department of Chemistry**

**Approved for Public Release;  
Distribution Unlimited**

**DTIC QUALITY INSPECTED 5**

## Scientific Personnel

David J. Singel	Principal Investigator
Michael H. Whitmore	Research Assistant
	Ph.D. Harvard University 1993
A. Sacra	Research Aide
	B.S. Harvard University 1992

## Publications

1. Comparison of Chromium-Doped Forsterite and Åkermanite Laser Host Crystals. H.M. Garrett, V.-H. Chan, H. Jenssen, M.H. Whitmore, D.J. Singel, and D. J. Simkin, in *OSA Proceedings on Advanced Solid-State Lasers*, edited by G. Dube and L. Chase (Optical Society of America, Washington, D.C. 1991) Vol. 10 p. 76.
2. Unequivocal Identification of the Near IR Lasing Center in Cr:Forsterite T.S. Rose, R.A. Fields, M.H. Whitmore, and D.J. Singel, in *OSA Proceedings on Advanced Solid-State Lasers*, edited by A. Pinto and L. Chase (Optical Society of America, Washington, D.C. 1992) Vol. 13 p. 17.
3. Electron Paramagnetic Resonance Spectroscopy of Tetrahedral Cr<sup>4+</sup> in Chromium-Doped Forsterite and Åkermanite, M.H. Whitmore, A. Sacra, and D.J. Singel, *Journ. Chem. Phys.* **98**, 3656 (1993).
4. Electron Paramagnetic Resonance Spectroscopy of Manganese-Doped Ba<sub>3</sub>(VO<sub>4</sub>)<sub>2</sub> : Identification of Tetrahedral Mn<sup>5+</sup> and Mn<sup>4+</sup> Centers, M.H. Whitmore, H. Verdun, and D.J. Singel, *Phys. Rev. B* **47**, 11479 (1993).
5. Optical Zeeman Spectroscopy of the Near IR Lasing Center in Chromium Forsterite. T.S. Rose, R.A. Fields, M.H. Whitmore, and D.J. Singel, *Journ. Opt. Soc. Amer. B*, **11**, 000 (1994).
6. Characterization of Optical Centers in Mn:Ba<sub>3</sub>(VO<sub>4</sub>)<sub>2</sub> by Spin-Echo EPR Spectroscopy. M.H. Whitmore, C.T. Farrar, B. Buyse, J. Coremans, J. Schmidt, and D.J. Singel, in *OSA Proceedings on Advanced Solid-State Lasers*, edited by T.-Y. Fan and B. Chai (Optical Society of America, Washington, D.C. 1994), in press.

*in preparation*

7. Electron Paramagnetic Resonance Spectroscopy of Chromium-Doped Lanthanum Lutetium Gallium Garnet, M. H. Whitmore and D.J. Singel
8. <sup>51</sup>V modulation of Mn<sup>5+</sup> electron spin echoes in Mn:Ba<sub>3</sub>(VO<sub>4</sub>)<sub>2</sub>: Identification of the Mn<sup>5+</sup> Substitution Site, C.T. Farrar and D.J. Singel
9. Spin-Echo and Optical Zeeman Spectroscopy of the Laser Active Center in Mn:Ba<sub>3</sub>(VO<sub>4</sub>)<sub>2</sub>, B. Buyse, J. Coremans, J. Schmidt, and D.J. Singel.

Accession For	
NTIS GRA&I	<input checked="" type="checkbox"/>
DTIC TAB	<input type="checkbox"/>
Unannounced	<input type="checkbox"/>
Justification	
By _____	
Distribution/	
Availability Codes	
Dist	Avail and/or Special
A-1	

## Table of Contents

Chapter 1	Introduction	1
Chapter 2	Electron Paramagnetic Resonance Spectroscopy of Tetrahedral $\text{Cr}^{4+}$ in Chromium-Doped Forsterite and Åkermanite	3
Chapter 3	Optical Zeeman Spectroscopy of the Near IR Lasing Center in Chromium Forsterite	64
Chapter 5	Comparison of Chromium-Doped Forsterite and Åkermanite Laser Host Crystals	93
Chapter 6	Electron Paramagnetic Resonance Spectroscopy of Chromium-Doped Gehlenites	100
Chapter 7	Electron Paramagnetic Resonance Spectroscopy of Manganese-Doped $\text{Ba}_3(\text{VO}_4)_2$ : Identification of Tetrahedral $\text{Mn}^{5+}$ and $\text{Mn}^{4+}$ Centers	106
Chapter 8	Electron Paramagnetic Resonance Spectroscopy of Chromium-Doped Lanthanum Lutetium Gallium Garnet	144
Chapter 9	Characterization of Optical Centers in $\text{Mn}:\text{Ba}_3(\text{VO}_4)_2$ by Spin-Echo EPR Spectroscopy	178

## **Chapter 1**

---

### **Introduction**

## Introduction - Research Highlights

This report provides a comprehensive summary of EPR and correlated optical spectroscopic studies conducted in our laboratory on a new class of solid-state materials with potential utility as near IR lasers. All of the studied materials involve oxide host lattices (silicates, vanadates, and germanates) doped with 3d transition metal-ions (chromium and manganese). The novelty of the materials is connected to the tetrahedral coordination and unusual oxidation states of the dopant ions. The objective in our studies is to determine these properties *of the laser active ions*. We rely on EPR spectroscopy to determine the elemental identity of dopant (and impurity) ions, the "spin" of the ions and hence their oxidation numbers, and the crystallographic position of the ion, hence the coordination number of the ion (barring crystallographic ambiguities). Correlated optical spectroscopies - such as optical Zeeman spectroscopy - are used to establish a link between magnetic resonance and optical properties: by linking a relevant optical center to an EPR spectrum, all of the characteristics ascertained through EPR can be attached to the optical center.

The impetus for this work stemmed from the discovery of laser action in chromium-doped forsterite, and the ensuing controversy regarding the coordination number and oxidation state of the chromium ion. *A key highlight of our research is the experimental proof that the tetrahedral  $\text{Cr}^{4+}$  is the active center in Cr:forsterite.* Chapters 2-5 in the report pertain to the forsterite problem. Chapter 2 provides a detailed introduction of the forsterite problem and an extended account of the EPR results and analysis through which we demonstrated the presence of tetrahedral  $\text{Cr}^{4+}$  in Cr:forsterite. (An abbreviated version of this work has been published: Journ. Chem. Phys. **98**, 3656 (1993)). Chapter 4 - a preprint of an article soon to appear in the literature (Journ. Opt. Soc. Amer. B **11** (1994)) - is a detailed account of the optical Zeeman spectroscopy, with fluorescence line-narrowing, that proves that the  $\text{Cr}^{4+}$  centers observed by EPR are also responsible for the near IR luminescence and laser activity. This work includes an analysis of the Zeeman splittings as well as a simple model to account for the intensities of the FLN spectral lines. Chapters 3 and 5 are reprints of preliminary reports of these studies, published in the *OSA Proceedings on Advanced Solid-State Lasers*; these brief papers are included here for completeness.

The results on forsterite - specifically, the discovery of tetra-oxo ion lasing centers - rapidly lead to *studies of numerous other materials conceived to incorporate  $3d^2$  ions at tetrahedral sites in oxide lattices.* The most significant of the surveyed materials is the manganese-doped barium vanadate system (Chapters 7 and 9), because of the demonstration of laser action in this material. We present an extended account of our EPR studies of  $(\text{Mn}:\text{Ba}_3(\text{VO}_4)_2)$  in Chapter 7. (An abbreviated version of this work has been published: Phys. Rev. B **47**, 11479 (1993)). This EPR study reveals the presence of both tetrahedral  $\text{Mn}^{5+}$  and  $\text{Mn}^{4+}$  in this material. In Chapter 9 we present a brief account - to be published in 1994 *OSA Proceedings on Advanced Solid-State Lasers* - of a novel optical/spin-echo double resonance study that proves that  $\text{Mn}^{5+}$  is the laser center in this material. This work represents the first application of time-domain EPR methods with pulsed laser excitation in these materials. We also present previously unpublished EPR results on Cr:gehlenites (Chapter 6) and Cr:LLGG (lanthanum lutetium gallium garnet) (Chapter 8). The gehlenite spectra do not appear to derive from isolated ions, a fact that might be related to its di-orthosilicate (sorosilicate) structure. The LLGG system reveals a  $\text{Cr}^{3+}$  rather than a  $\text{Cr}^{4+}$  center, because of the expansion of the garnet lattice LLGG, however, the  $\text{Cr}^{3+}$  is lodged at the tetrahedral, gallium site.

## Chapter 2

**Electron Paramagnetic Resonance Spectroscopy of Tetrahedral Cr<sup>4+</sup> in Chromium-Doped Forsterite and Åkermanite.**

**Electron Paramagnetic Resonance Spectroscopy of Tetrahedral  
Cr<sup>4+</sup> in Chromium-Doped Forsterite and Åkermanite.**

Michael H. Whitmore, Ann Sacra, and David J. Singel

Department of Chemistry, Harvard University,  
12 Oxford Street, Cambridge, Massachusetts 02138

**ABSTRACT**

The observation of near IR laser action in chromium activated forsterite by Petričević, *et al.*, (Appl. Phys. Lett. 52, 1040 (1988)) has spawned considerable interest in identifying and characterizing the quadrivalent chromium centers purportedly responsible for laser action in this material. The EPR (electron paramagnetic resonance) spectroscopy reported here of chromium-doped forsterite and structurally related Åkermanite provides compelling evidence for the presence of tetrahedral Cr<sup>4+</sup> centers in both materials. The EPR spectra reveal substitutional incorporation of chromium ions with triplet spin multiplicity, assignable to Cr<sup>4+</sup>. The fine structure and electron Zeeman interaction parameters of the centers in both materials are found to be very similar. In Åkermanite, the Cr<sup>4+</sup> center is unequivocally accommodated at tetrahedral lattice sites. The similarity of the spectroscopic properties of the Cr<sup>4+</sup> ions in the two materials thus implicates incorporation at the analogous tetrahedral sites in forsterite. In conjunction with the findings of recent optical Zeeman studies (K. R. Hoffman, *et al.*, Phys. Rev. B 44, 12589 (1991); T. S. Rose, *et al.* OSA Proceedings on Advanced Solid State Lasers 13, 17 (1992)), these EPR results demonstrate that tetrahedral Cr<sup>4+</sup> is responsible for the near IR laser activity in chromium-doped forsterite.



## I. INTRODUCTION

In recent years there has been considerable interest in the development of materials suitable for tunable solid state lasers, particularly those with emission in the NIR (near infrared) region of the electromagnetic spectrum. One material of particular significance is chromium activated forsterite,  $\text{Mg}_2\text{SiO}_4$ . Laser action was first demonstrated in chromium-doped forsterite by Petričević *et al.*,<sup>1</sup> who obtained coherent emission at 1235 nm upon pumping at 532 nm; they assigned the active center to  $\text{Cr}^{3+}$  substituting for  $\text{Mg}^{2+}$ . A broad absorption band between 850 nm and 1150 nm was also observed and attributed to impurities present in the crystal.<sup>1</sup> After Petričević *et al.*<sup>2</sup> and Verdún *et al.*<sup>3</sup> reported that NIR lasing could also be achieved by excitation directly within this absorption band, in particular at a wavelength of 1064 nm, an alternative assignment for the active center was suggested, namely  $\text{Cr}^{4+}$  substituting for silicon at tetrahedral lattice sites. This suggestion was supported by the contemporaneous identification of tetrahedral  $\text{Cr}^{4+}$  as the species responsible for parasitic NIR absorption in Nd:YAG lasers.<sup>4</sup>

In order to substantiate this view of  $\text{Cr}^{4+}$  substitution in forsterite, a number of detailed optical studies<sup>5-14</sup> have been undertaken. The optical spectra of chromium-doped forsterite are not highly diagnostic, however, owing largely to the breadth and lack of resolution of the spectral components — an inherent problem associated with laser materials with broadly tunable emission. The optical studies have therefore not completely resolved the identity of the active center.

The utility of EPR spectroscopy for the determination of the identity and oxidation state of metal ions in crystal hosts is well established. The forsterite system itself provides an excellent example of this utility: Rager and co-workers<sup>15-17</sup> have demonstrated the presence and discerned the incorporation mode of numerous paramagnetic ions in forsterite, including  $\text{Cr}^{3+}$ . In this article we report EPR spectral studies of chromium-doped forsterite that demonstrate the presence of  $\text{Cr}^{4+}$  ions. We present analogous EPR results for the

chromium-doped åkermanite,  $\text{Ba}_2\text{MgGe}_2\text{O}_7$  (BMaG), which possesses tetrahedral cation sites nearly identical to those of forsterite. The similarity of the EPR spectral properties found for the  $\text{Cr}^{4+}$  centers in these crystals, whose only common feature is the resemblance of their tetrahedral cation sites, strongly implicates these sites as the position of  $\text{Cr}^{4+}$  substitution in both BMaG and forsterite.

## II. THE CRYSTAL SYSTEMS.

### A. Crystal Structures

#### 1. Forsterite

The forsterite crystal is of orthorhombic symmetry with the space group  $\text{Pbnm}$  (see Figure 2.1).<sup>18</sup> The structure is composed of six-coordinate  $\text{Mg}^{2+}$  ions that link discrete  $\text{SiO}_4^{4-}$  tetrahedra (orthosilicate structure). Four  $\text{Mg}_2\text{SiO}_4$  formula units constitute the unit cell. Crystallographic data for forsterite is given in Table 2.1 and the crystal lattice viewed along each of the three crystallographic axes is shown in Figures 2.2, 2.3, and 2.4.

The  $\text{Si}^{4+}$  ions are situated at the crystallographic 4c position; the  $\text{Mg}^{2+}$  ions lie at two distinct equivalent positions, 4a and 4c (designated M1 and M2 respectively).<sup>18</sup> Accordingly, incorporation of  $\text{Cr}^{4+}$  through cationic substitution can occur only at the 4a or 4c positions. The former have site symmetry  $C_i$ , whereas the latter are situated on the mirror planes perpendicular to the crystallographic c axis and have site symmetry  $C_s$ . For an ion in the 4c position, the mirror symmetry requires that a magnetic principal axis — a principal axis of all electron spin interaction matrices — coincide with the c axis (see Figure 2.1 bottom). Inversion symmetry relations among the 4c positions lead to their pairwise magnetic equivalence for arbitrary orientation of the external magnetic field within the crystal. Moreover, all four centers are magnetically equivalent when the field lies in the ac or bc planes as a consequence of the dyad axes that interrelate the ions. In contrast, ions lodged at the 4a sites are pairwise magnetically equivalent when the field is oriented in the

Ion	Site	Sym.	Coordinates			q
			x	y	z	
Mg <sub>1</sub>	4a	T	0	0	0	+2
Mg <sub>2</sub>	4c	m	0.9687	0.2792	1/4	+2
Si	4c	m	0.4287	0.0957	1/4	+4
O <sub>1</sub>	4c	m	0.7661	0.0918	1/4	-2
O <sub>2</sub>	4c	m	0.2127	0.4514	1/4	-2
O <sub>3</sub>	8d	1	0.2844	0.1633	0.0357	-2

**TABLE 2.1.** Crystallographic data for forsterite. Orthorhombic Pbnm.  $a=4.756 \text{ \AA}$ ,  
 $b=10.207 \text{ \AA}$ ,  $c=5.980 \text{ \AA}$ .<sup>18</sup>

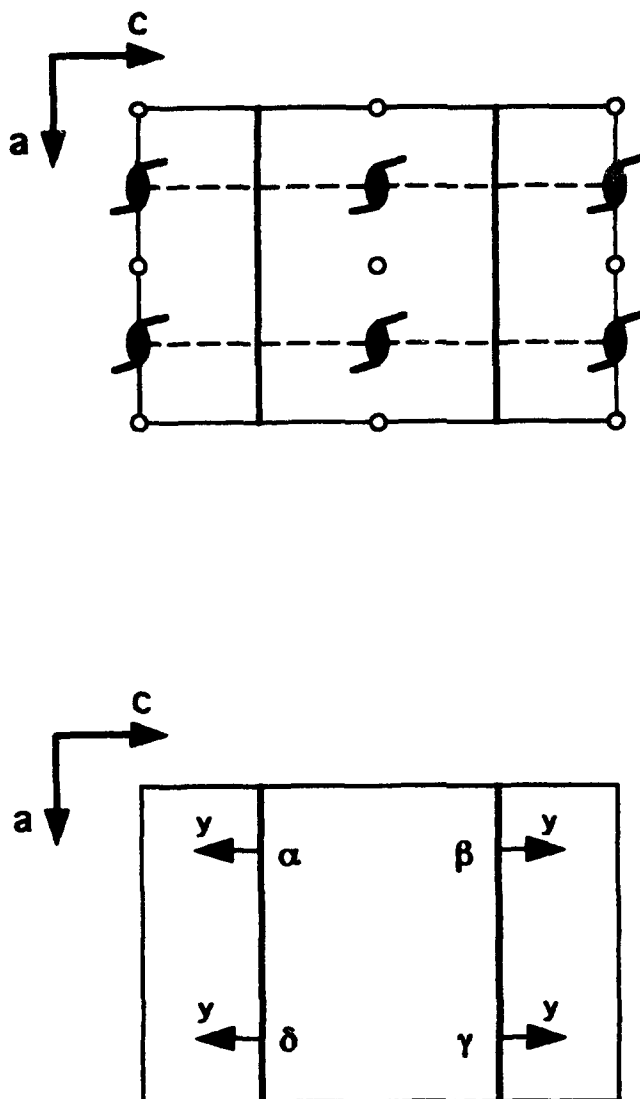


**FIG 2.1.** Diagrams of space group Pbnm showing orientation of crystal axis system. The heavy lines are mirror planes. The top figure shows the various space group operations with circles representing inversion centers, lozenges representing screw tetrads, and dashed lines representing glide planes. The bottom figure shows the four 4c sites (labeled with Greek letters) each with the mandatory magnetic axis, here labeled y, perpendicular to the mirror plane.<sup>49</sup>

**FIG 2.2. Forsterite crystal lattice showing silicon tetrahedra. View is parallel to the a-axis with the b-axis vertical.**

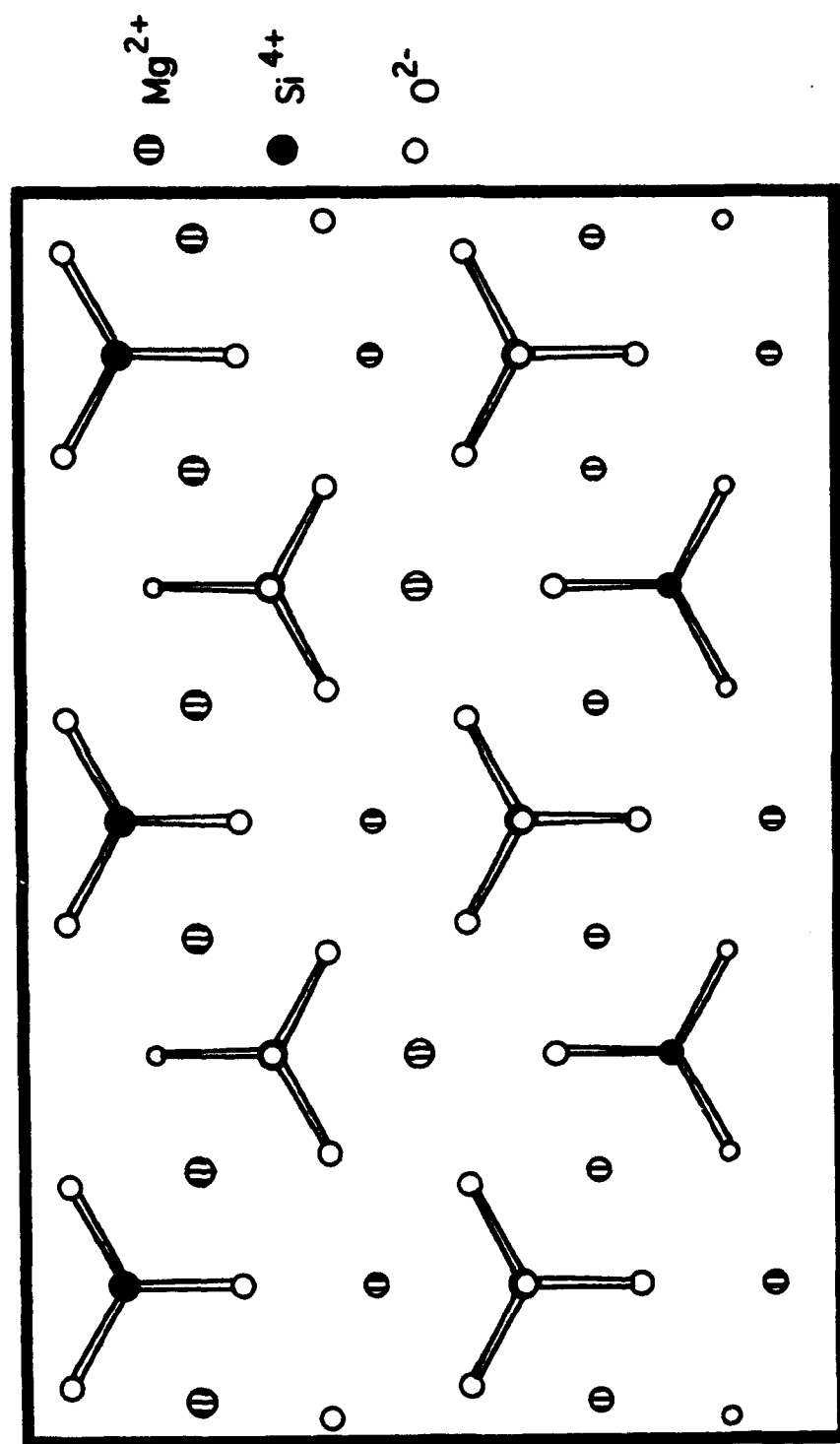


**FIG 2.3.** Forsterite crystal lattice showing silicon tetrahedra. View is parallel to the b-axis with the c-axis vertical.

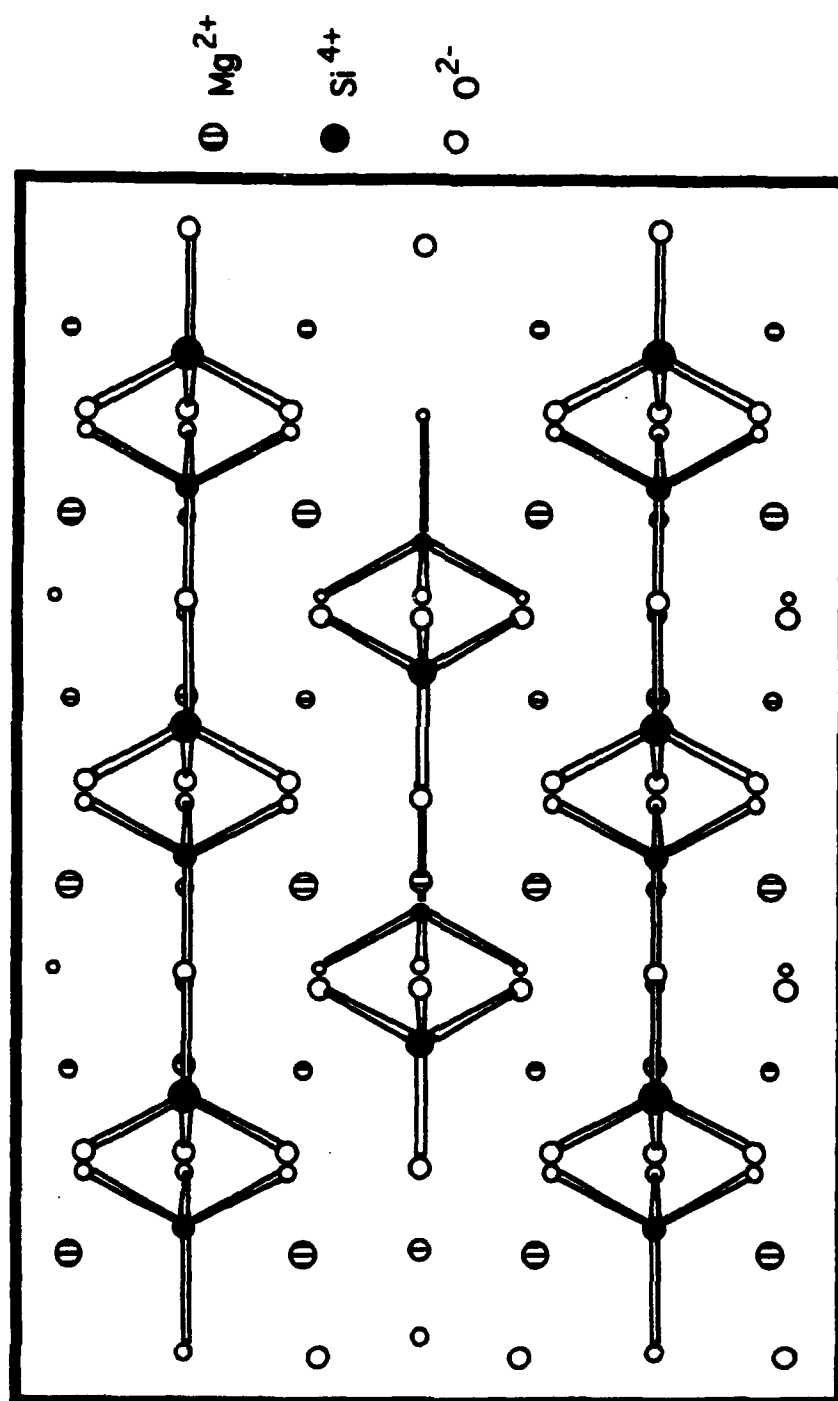
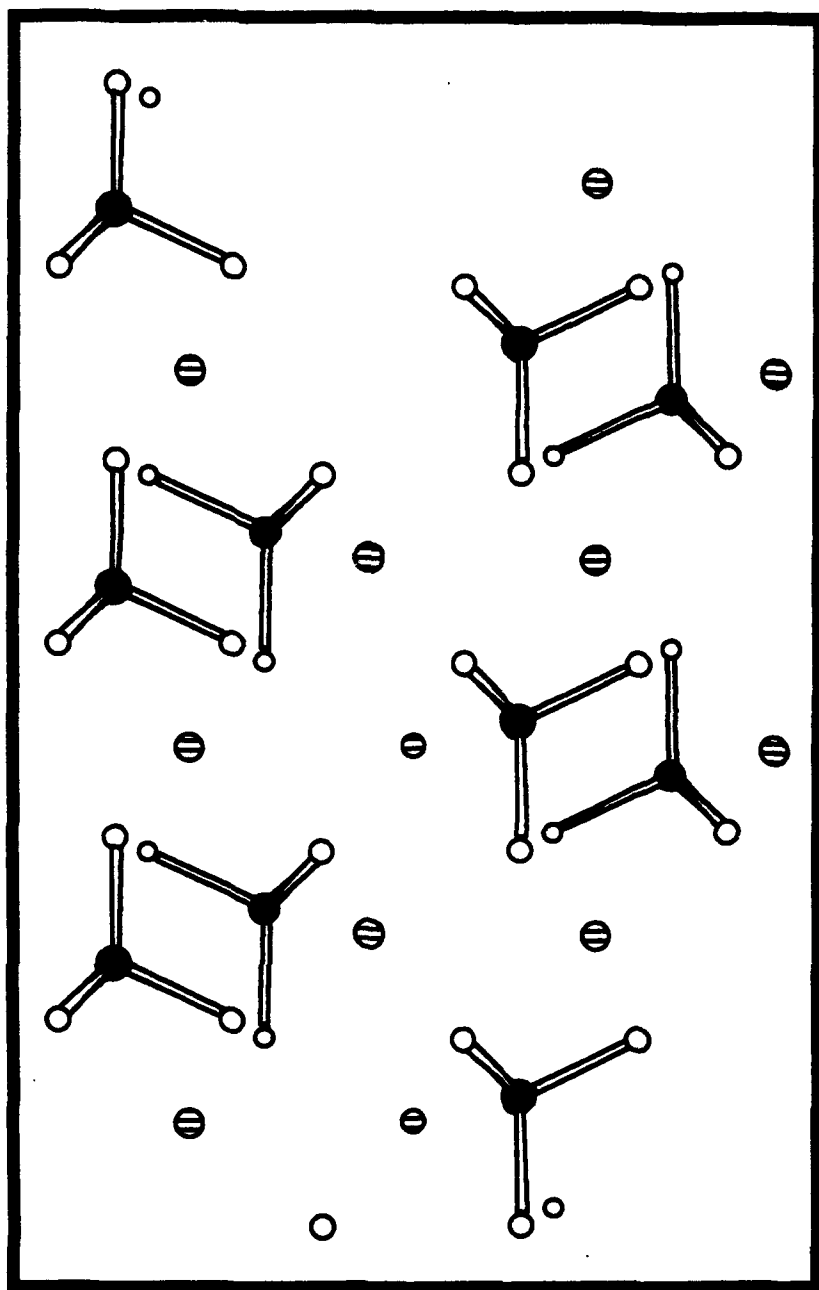




**FIG 2.4.** Forsterite crystal lattice showing silicon tetrahedra. View is parallel to the c-axis with the b-axis vertical.



planes orthogonal to the crystallographic axes, but no magnetic equivalences are required at arbitrary field orientations. These magnetic equivalences are summarized in Table 2.2.

The disparate patterns of magnetic equivalence permit ready identification of the crystallographic position of a substituted ion, as was shown, for example, by Rager in his study of  $\text{Cr}^{3+}$  in forsterite.<sup>15</sup> Unfortunately, since the 4c position in forsterite encompasses both the octahedral  $\text{Mg}^{2+}$  site and the tetrahedral  $\text{Si}^{4+}$  site, these patterns do not afford a full specification of either the substitution site of a cation or its coordination number. This ambiguity in site geometry motivates the study of  $\text{\AA}$ kermanite, which lack octahedral substitution sites altogether.

## 2. $\text{\AA}$ kermanite

The  $\text{\AA}$ kermanites CMSO ( $\text{Ca}_2\text{MgSi}_2\text{O}_7$ ) and BMaG ( $\text{Ba}_2\text{MgGe}_2\text{O}_7$ ) are composed of  $\text{Ca}^{2+}/\text{Ba}^{2+}$ , in eight fold oxygen coordination, and  $\text{Mg}^{2+}$ , in tetrahedral coordination, connecting pairwise interlinked oxygen tetrahedra (sorosilicate structure) centered on  $\text{Si}^{4+}/\text{Ge}^{4+}$ . The crystal has tetragonal symmetry with the space group  $P\bar{4}2_1m$  (see Figure 2.5) and two formula units per unit cell.<sup>19,20</sup> Crystallographic data for CMSO is given in Table 2.3 and the crystal lattice viewed along the crystallographic axes is shown in Figures 2.6, 2.7, and 2.8. As no X-ray structure is available for BMaG, data from the closely related  $\text{Ba}_2\text{ZnGe}_2\text{O}_7$  is given in Table 2.4.

The  $\text{Mg}^{2+}$  ions occur at position 2a and the  $\text{Ca}^{2+}/\text{Ba}^{2+}$  and  $\text{Si}^{4+}/\text{Ge}^{4+}$  ions at position 4e. The former have site symmetry  $S_4$  with the rotation axes parallel to the crystallographic c axis, whereas the latter lie on mirror planes perpendicular to the crystallographic  $\pm(a\pm b)$  axes<sup>21</sup> and have site symmetry  $C_s$ . The  $S_4$  symmetry of ions at the 2a position requires that they display axial symmetry in their spin coupling matrices, with unique magnetic axes lying along the crystallographic c axis (see Figure 2.5 bottom). Therefore, the two crystallographically equivalent sites must, in general, be magnetically equivalent. Ions located at the 4e position must have a magnetic principal axis normal to the mirror plane on

Position	Number of crystallographic equiv. sites	Site symmetry	Magnetic equivalence for $H_0$ in direction or plane indicated. Arbitrary labeling of crystallographically equivalent sites $\alpha, \beta, \delta, \gamma$ .							
			a	b	c	ab plane	bc plane	ac plane	a+b	a+b,c plane
4a	4	1	$\alpha=\beta=\delta=\gamma$	$\alpha=\beta=\delta=\gamma$	$\alpha=\beta=\delta=\gamma$	$\alpha=\gamma, \beta=\delta$	$\alpha=\beta, \delta=\gamma$	$\alpha=\beta, \delta=\gamma$		
4c	4	m	$\alpha=\beta=\delta=\gamma$	$\alpha=\beta=\delta=\gamma$	$\alpha=\beta=\delta=\gamma$	$\alpha=\beta, \delta=\gamma$	$\alpha=\beta=\delta=\gamma$	$\alpha=\beta=\delta=\gamma$		
2a	2	$\bar{4}$	$\alpha=\beta=\text{constant}$	$\alpha=\beta=\text{constant}$	$\alpha=\beta$	$\alpha=\beta=\text{constant}$	$\alpha=\beta$	$\alpha=\beta$	$\alpha=\beta=\text{constant}$	$\alpha=\beta$
4e	4	m	$\alpha=\beta=\delta=\gamma$	$\alpha=\beta=\delta=\gamma$	$\alpha=\beta=\delta=\gamma$	$\alpha=\gamma, \beta=\delta$	$\alpha=\beta, \delta=\gamma$	$\alpha=\beta, \delta=\gamma$	$\alpha=\gamma, \beta=\delta$	$\alpha, \gamma, \beta, \delta, \gamma$

TABLE 2.2. Magnetic equivalencies for possible cation substitution sites in forsterite and åkermanites.

Ion	Site	Sym.	Coordinates			q
			x	y	z	
Ca	4e	m	0.3355	0.5 - x	0.5073	+2
Mg	2a	$\bar{4}$	0	0	0	+2
Si	4e	m	0.1396	0.5 - x	0.9412	+4
O <sub>1</sub>	2c	mm	0.5000	0.5 - x	0.1804	-2
O <sub>2</sub>	4e	m	0.1450	0.5 - x	0.2583	-2
O <sub>3</sub>	8f	1	0.0820	0.1820	0.7909	-2

TABLE 2.3. Crystallographic data for CMSO ( $\text{Ca}_2\text{MgSi}_2\text{O}_7$ ). Tetragonal  $P\bar{4}2_1m$ .

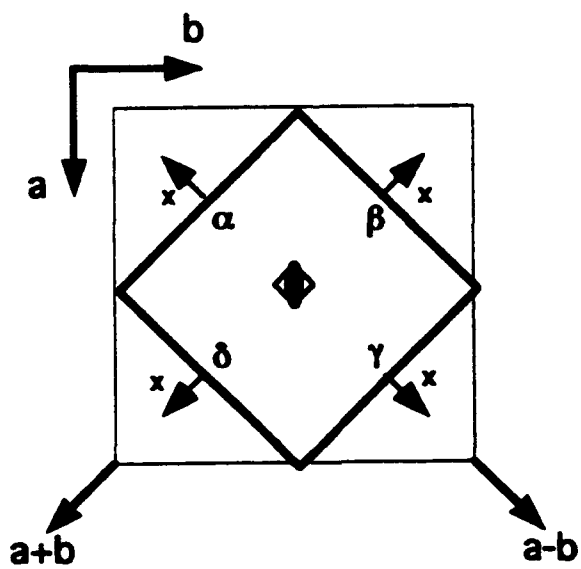
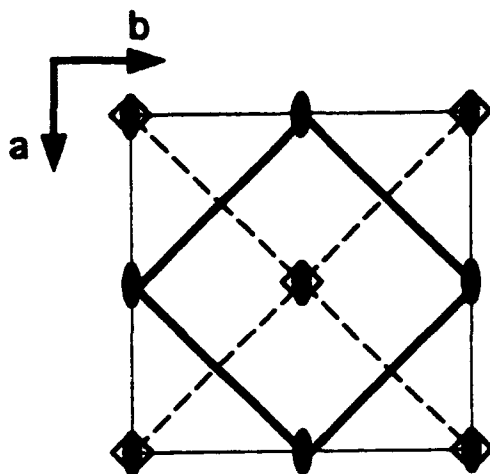
$a=b=7.789 \text{ \AA}$ ,  $c=5.018 \text{ \AA}$ .<sup>20</sup>

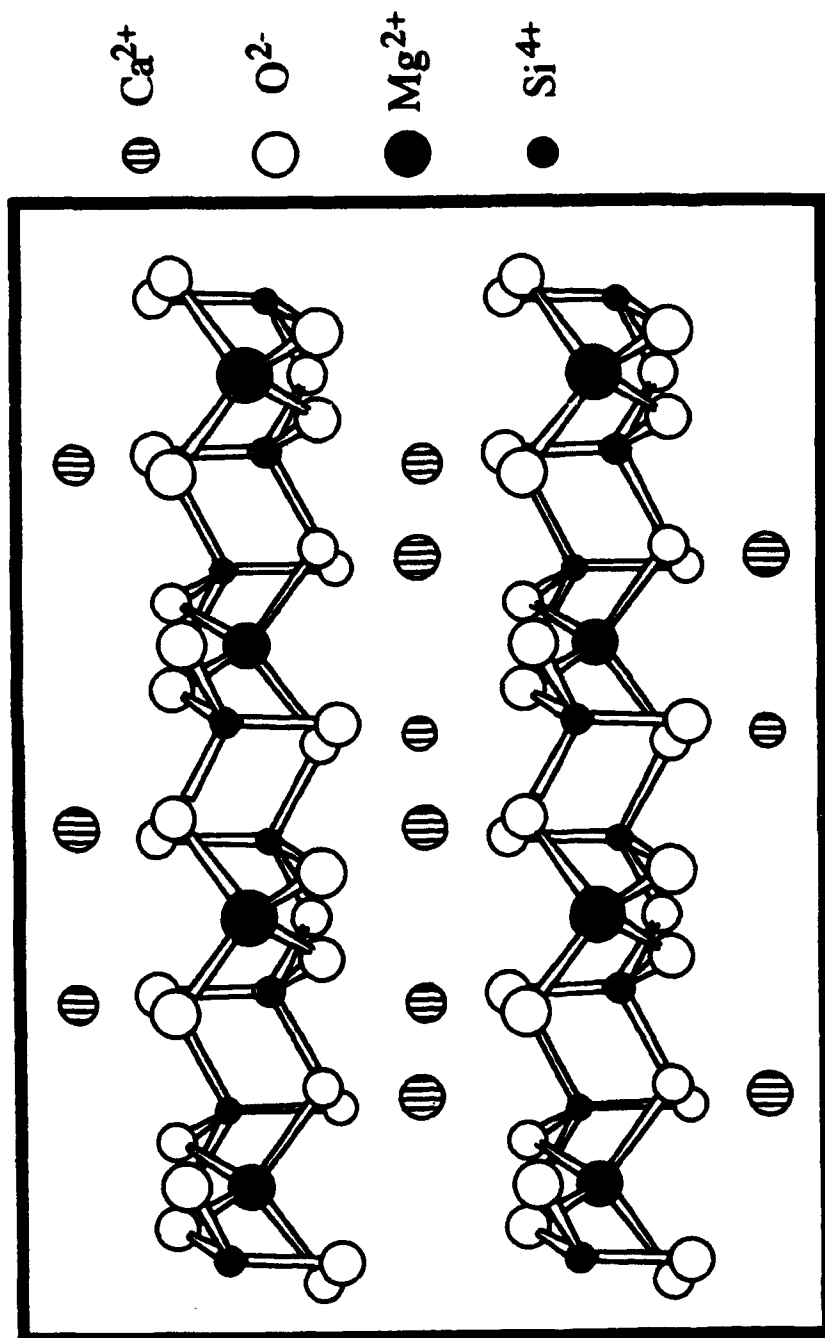
Ion	Site	Sym.	Coordinates			q
			x	y	z	
Ba	4e	m	0.1651	-0.3349	0.4927	+2
Zn	2a	$\bar{4}$	0	0	0	+2
Ge	4e	m	0.3591	-0.1409	0.0383	+4
O <sub>1</sub>	2c	mm	0.0826	0.1873	0.8105	-2
O <sub>2</sub>	4e	m	-0.1393	-0.3607	0.2717	-2
O <sub>3</sub>	8f	1	0.0000	0.5000	0.8404	-2

TABLE 2.4. Crystallographic data for BZaG ( $\text{Ba}_2\text{ZnGe}_2\text{O}_7$ ). Tetragonal

$P\bar{4}2_1m$ .  $a=b=8.347 \text{ \AA}$ ,  $c=5.554 \text{ \AA}$ .<sup>19</sup>

FIG 2.5. Diagrams of space group  $P\bar{4}2_1m$  showing orientation of crystal axis system. The heavy lines are mirror planes. The top figure shows the various space group operations with lozenges representing rotation diads, lozenge/diamonds representing inversion tetrads, and dashed lines representing glide planes. The bottom figure shows the four 4e sites (labeled with Greek letters) each with the mandatory magnetic axis, here labeled  $x$ , perpendicular to the mirror plane.<sup>49</sup>

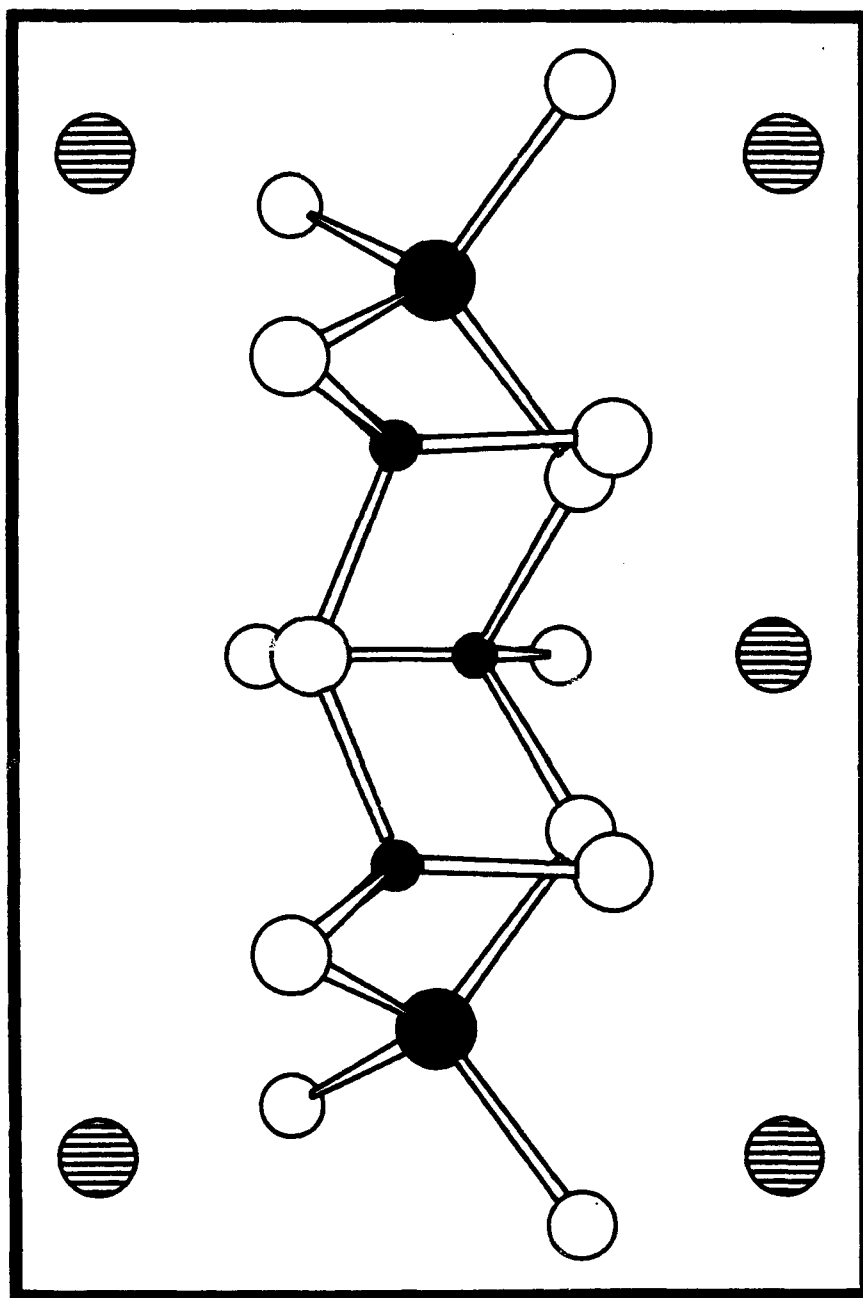




**FIG 2.6.** CMSO ( $\text{Ca}_2\text{MgSi}_2\text{O}_7$ ) crystal lattice showing silicon tetrahedra. View is parallel to the *a*-axis with the *c*-axis vertical.



**FIG 2.7.** CMSO ( $\text{Ca}_2\text{MgSi}_2\text{O}_7$ ) crystal lattice showing silicon tetrahedra. View is parallel to an  $a+b$ -axis with the  $c$ -axis vertical.



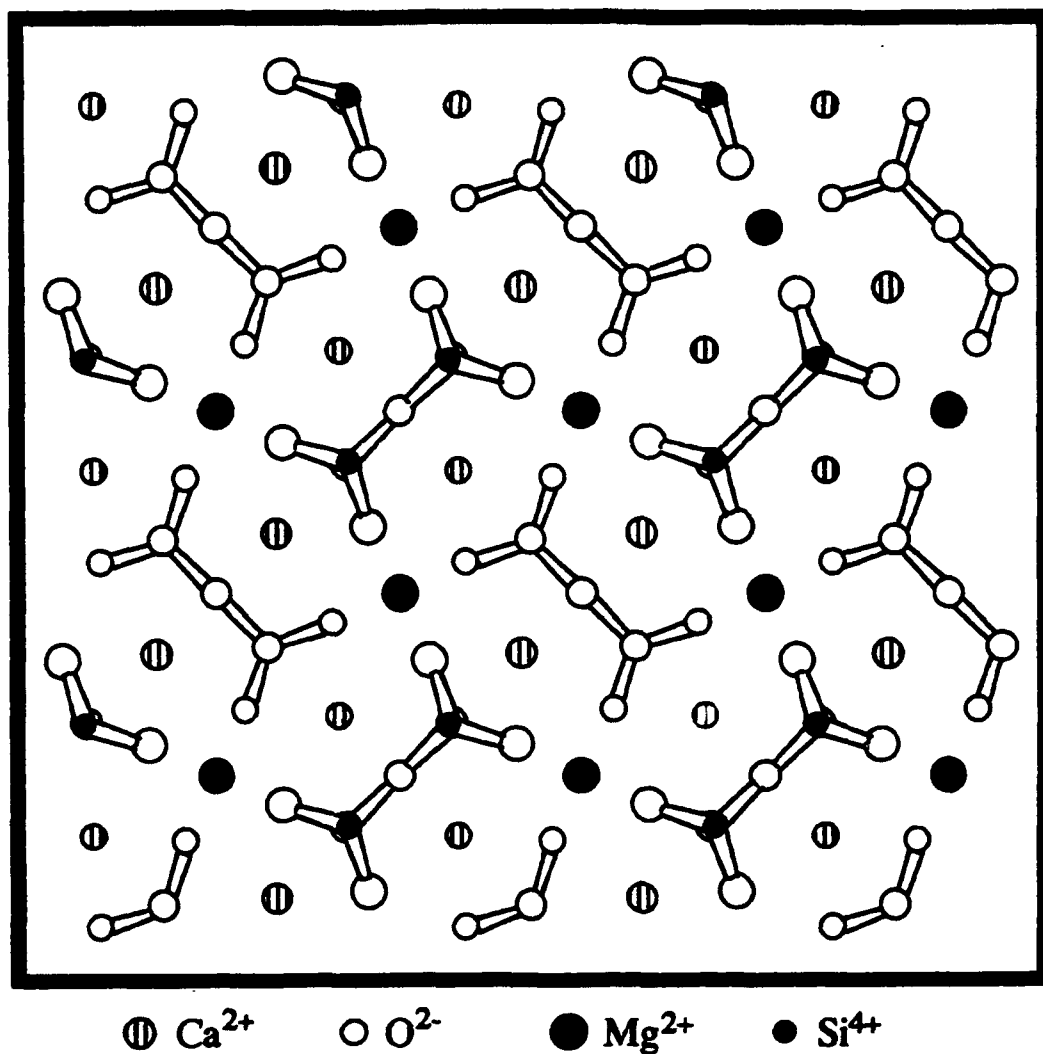


**FIG 2.8.** CMSO ( $\text{Ca}_2\text{MgSi}_2\text{O}_7$ ) crystal lattice showing silicon tetrahedra. View is parallel to the c-axis with the a-axis vertical.

which they are situated. The four crystallographically equivalent sites are thus pairwise magnetically equivalent in the three principal crystallographic planes, but need show no magnetic equivalence for an arbitrary orientation of the field within the crystal. These magnetic equivalences are summarized in Table 2.2.

Inasmuch as the patterns of magnetic equivalence for ions at the 4e and 2a positions are very different, substitution at the two tetrahedral positions is readily distinguishable. Moreover, while the 4e position embraces two substitution sites, the disparity in ionic radii of  $\text{Ca}^{2+}/\text{Ba}^{2+}$  versus  $\text{Si}^{4+}/\text{Ge}^{4+}$  suffices to remove any ambiguity in site assignment: only the latter site is fitting for  $\text{Cr}^{4+}$  substitution.

### 3. Comparison of Structures

The only common feature of the åkermanite and forsterite structures is the similarity of their  $\text{SiO}_4^{4-}$  tetrahedra. This similarity is illustrated in Figure 2.9. Most notably, åkermanite lacks the octahedral cation sites through which forsterite accommodates a host of guest ions.<sup>15-17</sup> The greater selectivity of åkermanite facilitated our initial discovery and characterization of the EPR spectrum of tetrahedral  $\text{Cr}^{4+}$  centers. The results on BMaG, in turn, facilitated the subsequent identification of the analogous center in chromium-doped forsterite.

#### B. $\text{Cr}^{4+}$

Both forsterite and BMaG crystals were doped with chromium under oxidizing conditions designed to promote inclusion as  $\text{Cr}^{4+}$ . The quadrivalent chromium ion has a ground electronic configuration of  $[\text{Ar}]\text{3d}^2$  with the lowest energy Russell-Saunders term of  $^3\text{F}$ . In a weak tetrahedral crystal field, the  $^3\text{F}$  term is split with the  $^3\text{A}_2$  state lying lowest as shown in Figure 2.10. Based on optical data of the presumed  $\text{Cr}^{4+}$  tetrahedral site,<sup>5,6,9</sup> the  $^3\text{A}_2$  state would be stabilized by  $10^4 \text{ cm}^{-1}$  relative to the next highest state,  $^3\text{T}_2$ . The isolation of the orbitally non-degenerate ground state makes the observation of the  $\text{Cr}^{4+}$  EPR

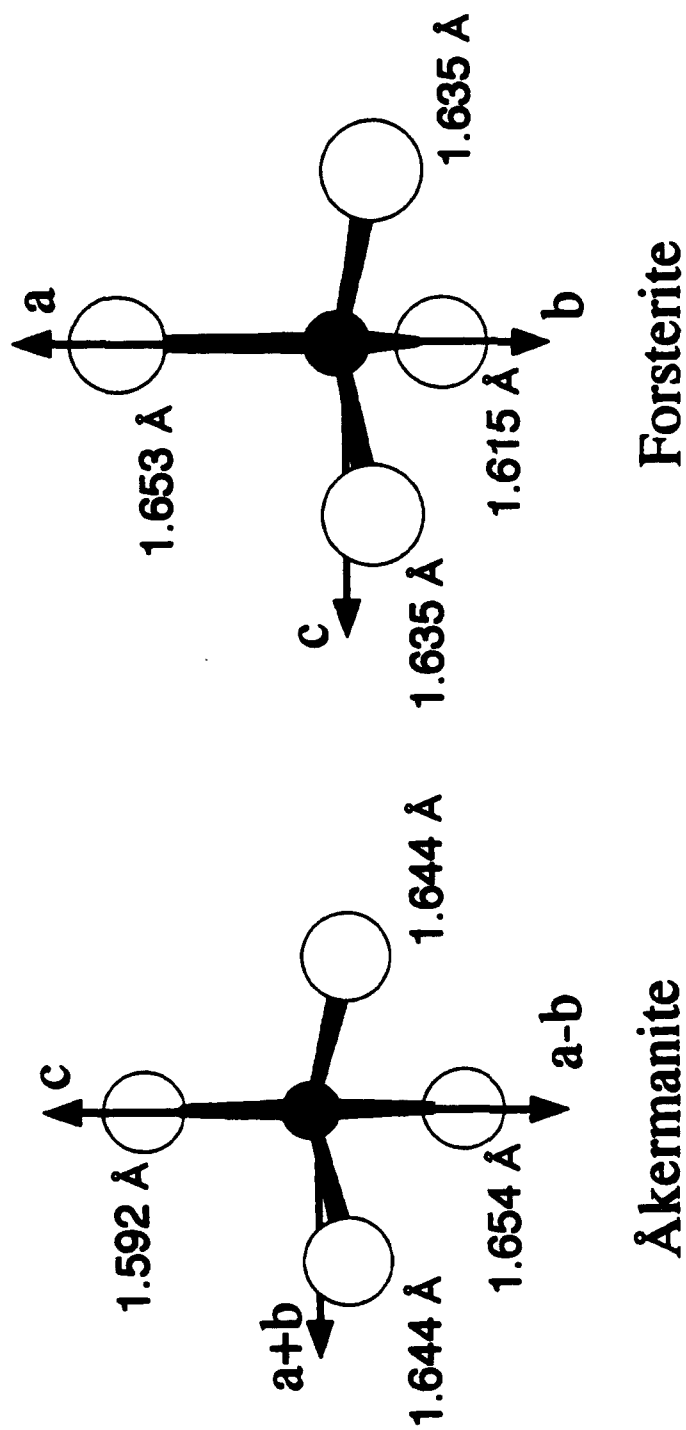


FIG 2.9. Comparison of the structure of the silicate tetrahedra in forsterite and åkermanite (CMSO). In both diagrams the view is parallel to the mirror symmetry plane on which the Si are located.

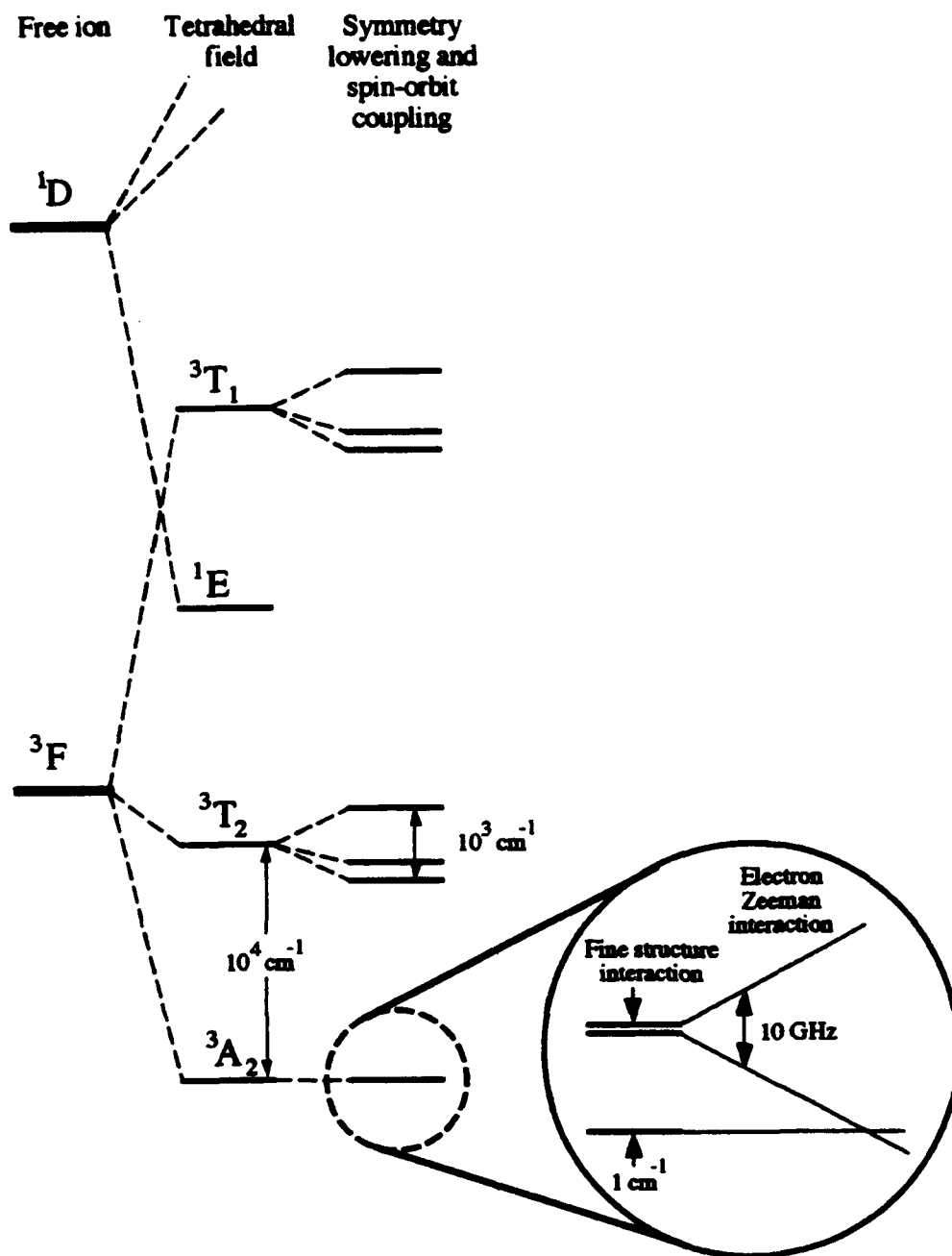


FIG 2.10. Energy level diagram for a  $d^2$  ion in a tetrahedral field.

possible at room temperature. In contrast, in octahedral fields the  $^3T_1$  state lies lowest. The orbital degeneracy of this state would be raised by the joint effects of spin-orbit coupling and symmetry-lowering in åkermanite and forsterite. Nonetheless, the resulting low-lying electronic excited states would typically lead to rapid spin-lattice relaxation and necessitate low temperatures for the observation of EPR.<sup>22</sup>

The triplet spin degeneracy of the  $^3A_2$  ground state of tetrahedral  $Cr^{4+}$  is similarly lifted by spin-orbit coupling and symmetry-lowering. We summarize the fine-structure and Zeeman interactions of the ion using the conventional spin Hamiltonian,<sup>22</sup>

$$H = -|\mu_B| B_0 \cdot g \cdot S + D (S_z^2 - S \cdot S / 3) + E (S_x^2 - S_y^2) \quad (2-1)$$

in which  $|\mu_B|$  is the magnitude of the Bohr magneton,  $B_0$  is the laboratory field,  $g$  is the Zeeman interaction matrix,  $S$  is the electron spin operator, with  $S=1$ , and  $D$  and  $E$  are the fine structure parameters;  $x$ ,  $y$ , and  $z$  comprise the principal axes of the fine structure interaction. If the  $g$ -anisotropy is very small (as we ultimately find to be the case), distinctions between  $\{x, y, z\}$  and the principal axes of  $g$  would be scarcely discernible. Accordingly, we take the two principal axis systems to be coincident.

### III. APPARATUS AND EXPERIMENTAL PROCEDURES

#### A. Crystals

Single crystals of chromium-doped forsterite were obtained from Dr. R. C. Morris of Allied-Signal Corporation, Professor D. J. Simkin of McGill University, and Dr. H. R. Verdún of Fibertek Inc. These crystals were examined optically and shown to manifest absorptions associated with the putative  $Cr^{4+}$  center.<sup>3,6,7,10</sup> The crystals obtained from Morris were doped heavily enough to show distinct coloration with trichroism visible to the naked eye. The samples from Simkin and Verdun were more lightly doped and showed only faint color. All crystals were free of visible flaws. The crystals were cut into cubes with faces

perpendicular to the a, b, and c axes. Sample volumes were approximately 0.01 to 0.02 cm<sup>3</sup>.

Single crystals of chromium-doped BMaG and CMSO were obtained from Professor H. P. Janssen of MIT. Optical spectra of these crystals displayed the same characteristic absorptions as those attributed to Cr<sup>4+</sup> in forsterite.<sup>23</sup> Two BMaG samples of differing chromium concentration (0.01 and 0.5 mole percent in the melt) were used for the experiments; both were aqua blue in color. The CMSO sample had a chromium concentration of 0.25 mole percent in the melt and was purple in color. All samples were free of visible flaws. The crystals were cut into right triangular prisms with faces perpendicular to the a, b, c and a+b axes and with volumes of approximately 0.01 to 0.02 cm<sup>3</sup>.

#### B. EPR Spectroscopy

EPR experiments were performed with a Varian E-109 X-band spectrometer using 100kHz modulation and a Varian E-231 TE<sub>102</sub> rectangular cavity. The field was varied over a range of 0.05 to 10 kG and measured with a Walker Scientific MG-3D gaussmeter that was calibrated with a Micro-Now Instruments Model 515B-1 proton gaussmeter. Observations were obtained at frequencies of 9.5, 9.2 and 9.1 GHz. Most experiments were carried out with samples at ambient temperatures, although some were performed at temperatures of approximately 100 K and 10 K. Low temperatures were achieved using either a Varian E-257 Variable Temperature Accessory or an Air Products LTD-3-110 HeliTran liquid He transfer system. Some experiments were performed at Bruker Instruments, Inc. (Billerica, MA) on a Bruker ESP 300 X-band spectrometer.

The sample crystals were mounted by use of Apiezon N grease on rexolite sample rods. The normal to the desired crystal rotation plane was aligned by eye along the rod rotation axis; the alignment error in mounting was less than 25m°. The rods were then mounted in a Varian goniometer and rotated in the cavity about an axis parallel to the microwave field, B<sub>1</sub>, and perpendicular to B<sub>0</sub>. The uncertainty in the angular orientation of the sample



due to the rotator gear was approximately  $2\text{mm}$ . Experiments performed at Bruker involved samples mounted on a double circle goniometer that allowed rotation of the crystal samples about orthogonal axes parallel to both  $B_1$  and  $B_0$ .

#### IV. EXPERIMENTS and RESULTS

##### A. Åkermanite

Measurements were made on BMaG with magnetic field rotation in the  $ab$ ,  $ac$ , and  $a+b,c$  crystallographic planes.<sup>24</sup> As indicated in Sec. II A.2, crystallographic symmetry ordains that the principal axes of the fine-structure and electron-Zeeman interaction can be found in these planes for any cation incorporated substitutionally in Åkermanite. In the 0.5 percent sample three sets of strong EPR signals were found at room temperature. Two of these sets can be identified as belonging to ions substituting at the 2a site; they are readily assigned to  $\text{Mn}^{2+}$ , with its characteristic hyperfine structure,<sup>25</sup> and  $\text{Fe}^{3+}$ , with an axial spectrum similar to  $\text{Fe}^{3+}$  in garnet.<sup>26</sup> The third set of signals displays intensities several times greater than those of the signals assigned to  $\text{Fe}^{3+}$  or  $\text{Mn}^{2+}$  (see Figure 2.11 top). In the 0.01 percent sample, however, only the  $\text{Mn}^{2+}$  and  $\text{Fe}^{3+}$  signals were detected; these signals were of approximately the same amplitude as in the more heavily doped sample. We therefore attribute the third set of signals to chromium. The observed lines are broad (approximately 80G) and have no apparent structure. Similar experiments were performed on the CMSO crystal; although  $\text{Mn}^{2+}$  signals were found, no signals analogous to those of chromium in BMaG were observed.

The fields-for-resonance of the chromium centers in BMaG were measured as a function of orientation of  $B_0$  within the  $ab$ ,  $ac$ , and  $a+b,c$  crystallographic planes. The results are shown as the plotted points in Figure 2.12. The variation in resonant field with rotation in the  $ab$  plane clearly indicates that the signals originate from the 4e sites: for an ion located at the 2a position, this resonant field should be stationary as the field is rotated in this plane. In view of the pairwise magnetic equivalence of the 4e sites in the  $ab$  and  $bc$

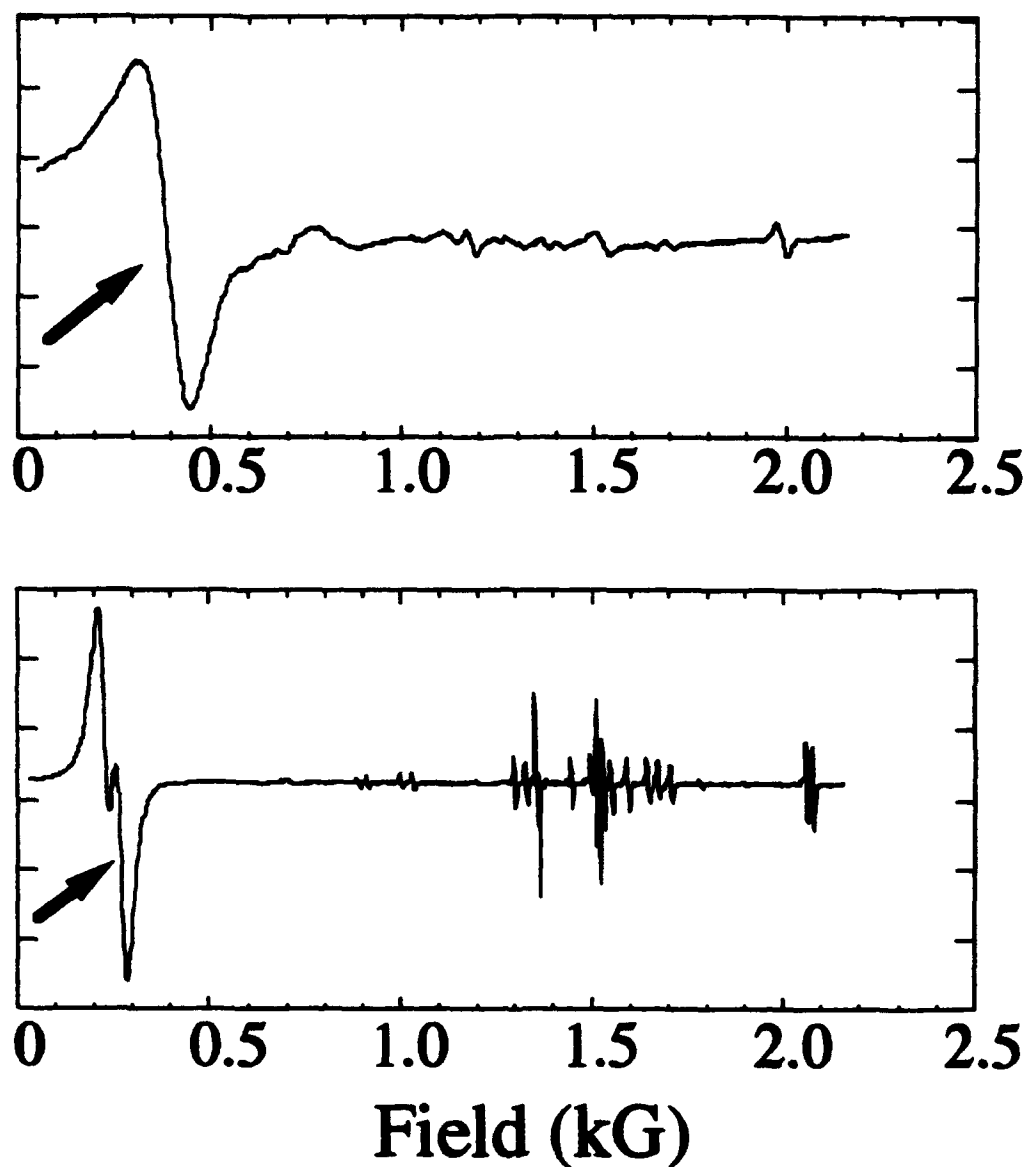


**FIG 2.11.** Exemplary EPR spectra of chromium-doped: BMaG (top) with  $B_0$  near  $a+b$  and  $B_1$  along  $a$ , and forsterite (bottom) with  $B_0$  near  $b$  and  $B_1$  along  $a$ . The arrows designate the EPR lines assigned to tetrahedral  $Cr^{4+}$ ; the sharp lines in the forsterite spectrum derive from the  $Cr^{3+}$  species analyzed by Rager and co-workers (Refs. 15,16,17). The EPR lines associated with the most prominent of these species are truncated in this display.

**FIG 2.12.** Field-for-resonance vs. orientation of  $B_0$  in the ab, bc and c,a+b crystallographic planes for  $\text{Cr}^{4+}$  in  $\text{BMsG}$ . The points are the experimental data, and the solid curves derive from the best fit spin-Hamiltonian parameters, as described in the text.



planes, the appearance of only two lines in these planes discloses that only one resonance absorption per magnetically inequivalent site is observed.

There is one anomaly in this analysis of the signals: the absence, for field rotation in the  $a+b,c$  plane, of the lines that correspond to the low field lines that are observed when the field is rotated in the  $ab$  plane. When  $B_0$  lies in the  $ab$  plane (with  $B_1$  along  $c$ ), in particular along  $a+b$ , two lines are visible, but when  $B_0$  lies in the  $a+b,c$  plane (with  $B_1$  along  $a-b$ ) only one line is found, even when  $B_0$  is again along  $a+b$ . Evidently the intensity of the low field line depends strongly on the orientation of the microwave field, vanishing when  $B_1$  is oriented along  $a-b$ .

To characterize this behavior more fully we utilized a two circle goniometer to perform experiments in which we aligned  $B_0$  along  $a+b$  then rotated the crystal about  $B_0$ , thus varying the orientation of  $B_1$  in the crystal. The series of EPR spectra obtained in this manner is shown in Figure 2.13. A progression of signal intensity from a maximum, when  $B_1$  lies along  $c$ , to a minimum, when  $B_1$  lies along  $a-b$ , is observed.

#### B. Forsterite

Measurements were made on forsterite with magnetic field rotation in the  $ab$ ,  $ac$ , and  $bc$  crystal planes. As noted in Sec. II A.1, a cation incorporated at the  $4c$  site in forsterite must have one of its magnetic axes oriented along  $c$  with the other two lying in the  $ab$  plane. Scores of EPR signals were detected in each of the laser crystals examined; many of these are shown in Figure 2.14. In the  $ac$  and  $bc$  planes a signal was detected very much like that of chromium in BMaG. This signal, observable at room temperature, is strong, broad (approximately 30G), and featureless (see Figure 2.11 bottom). Experiments were performed on several crystals; the signal intensity shows positive correlation with the coloration of the crystal and thus the chromium concentration. We therefore attribute the signal to chromium.

**FIG 2.13.** Variation of  $\text{Cr}^{4+}$  EPR intensity in BMaG with crystal rotation about  $B_0$ . In the series of spectra shown,  $B_0$  is parallel to  $a+b$  while the orientation of  $B_1$  is varied from  $c$  (signal maximum) through  $a-b$  (signal minimum). The EPR line observed corresponds to the low field line in the  $ab$  plane shown in Figure 2.12.

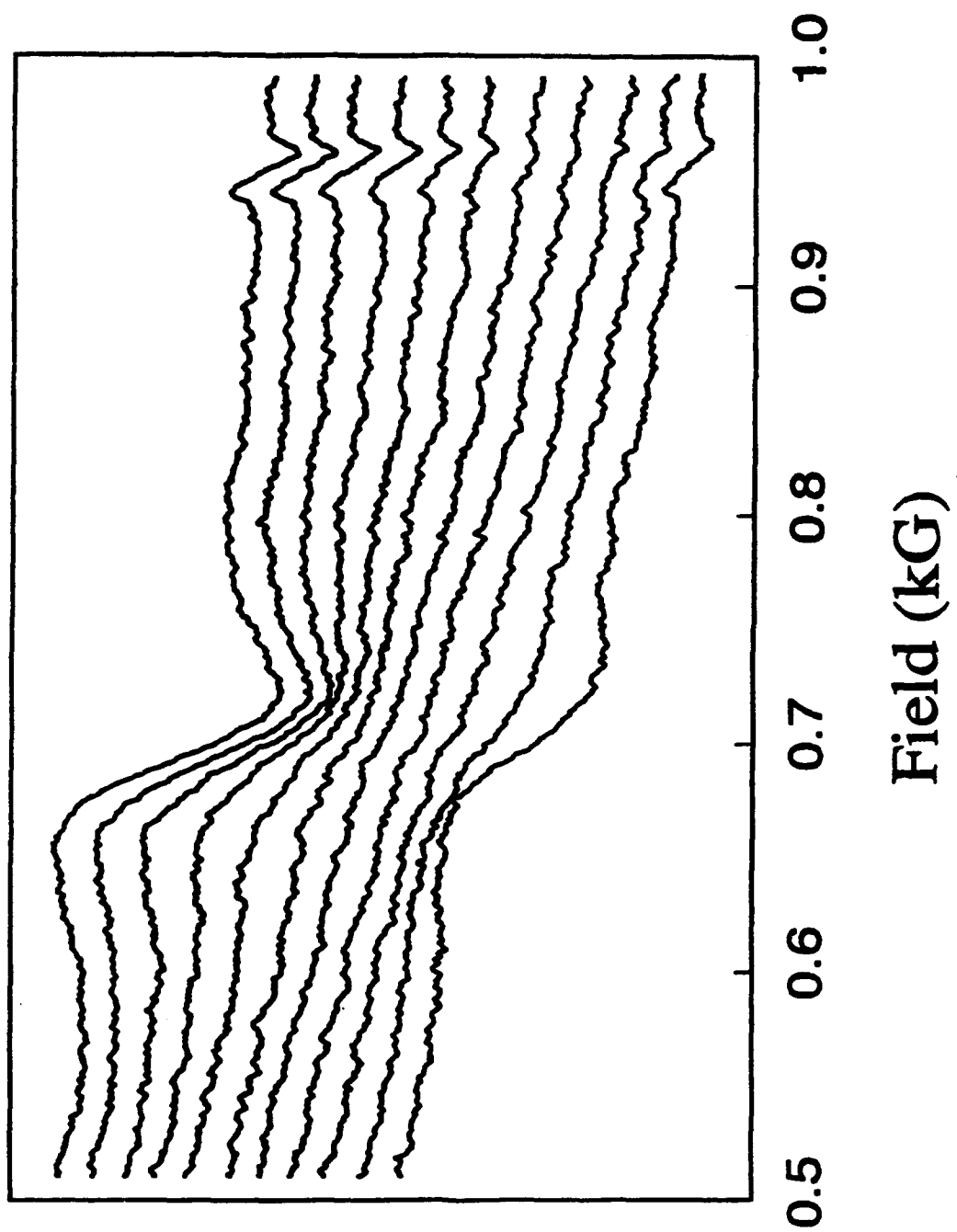
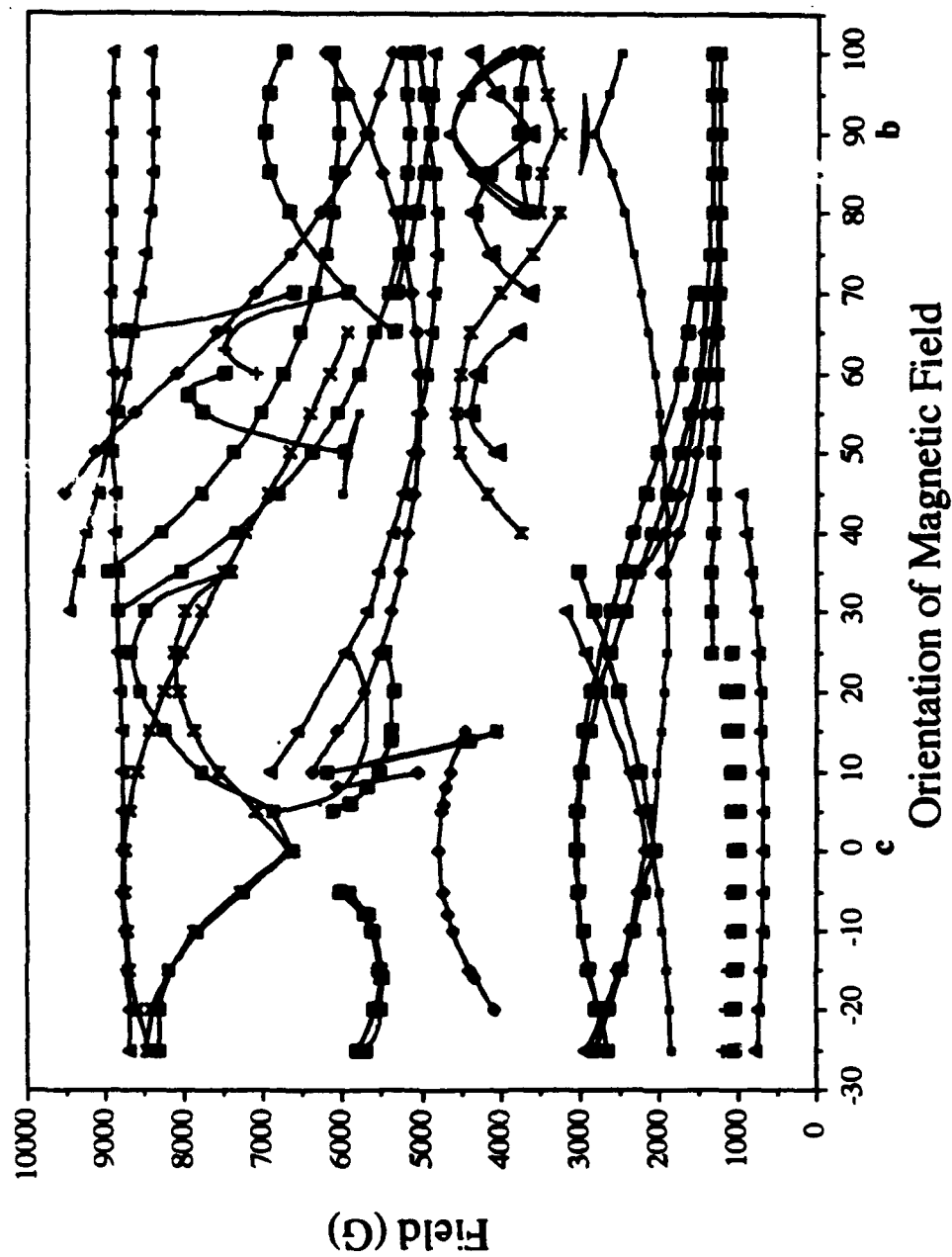


**FIG 2.14.** Field-for-resonance vs. orientation of  $B_0$  in the bc crystallographic plane for unidentified ions in forsterite.





The fields-for-resonance associated with rotation of the magnetic field in the *ac* and *bc* planes are shown as the plotted points in Figure 2.15; the gaps in the data are a consequence of spectral overlap with other strong signals. The low field extrema in these planes show a dependence on the spectrometer frequency. With  $B_0$  oriented along *a* (or *b*) these extrema are: observed at 610 G for a frequency of 9.5 GHz, observed at 160 G for a frequency of 9.2 GHz; and no longer detectable at a frequency of 9.1 GHz. Evidently, the resonant levels are split by between 9.1 GHz and 9.2 GHz in zero field, and diverge upon application of an external field oriented along *a* (or *b*).

No signal was observed for rotation with the magnetic field in the *ab* plane, notwithstanding careful inspection of the spectra obtained with  $B_0$  along either *a* or *b* — orientations at which lines were detected with field rotation in the *ac* or *bc* planes. Clearly, the signal intensity of transitions in the *ab* plane depends on the orientation of  $B_1$ . Deliberate misalignment of the rotation axis, specifically a tilt of approximately 50–150 mrad tilt about *b*, allowed two lines to be detected, albeit at much lower intensity than was seen in the *ac* and *bc* planes. These signals are shown as the plotted points in Figure 2.16.

The presence of only one signal in the planes containing *c* demonstrates that the chromium ion must occupy the 4c position rather than the 4a position from which at least two signals would derive. In the *ab* plane the 4c sites are pairwise equivalent resulting in the two signals seen in Figure 2.16. The presence of only these discrete signals discloses that, as is the case with BMaG, only one resonance absorption per magnetically inequivalent site is observed.

## V. ANALYSIS OF RESULTS

For forsterite, three key observations are sufficient for assigning the proper spin multiplicity to the chromium ion: 1) the presence of only a single resonance absorption per magnetically inequivalent site in the surveyed field range, 2) the dependence of the intensity of the signal on the microwave field orientation within the crystal, and 3) the presence

**FIG 2.15.** Field-for-resonance vs. orientation of  $B_0$  in the bc and ac crystallographic planes for  $Cr^{4+}$  in forsterite. The points are the experimental data, and the solid curves derive from the best fit spin-Hamiltonian parameters, as described in the text.

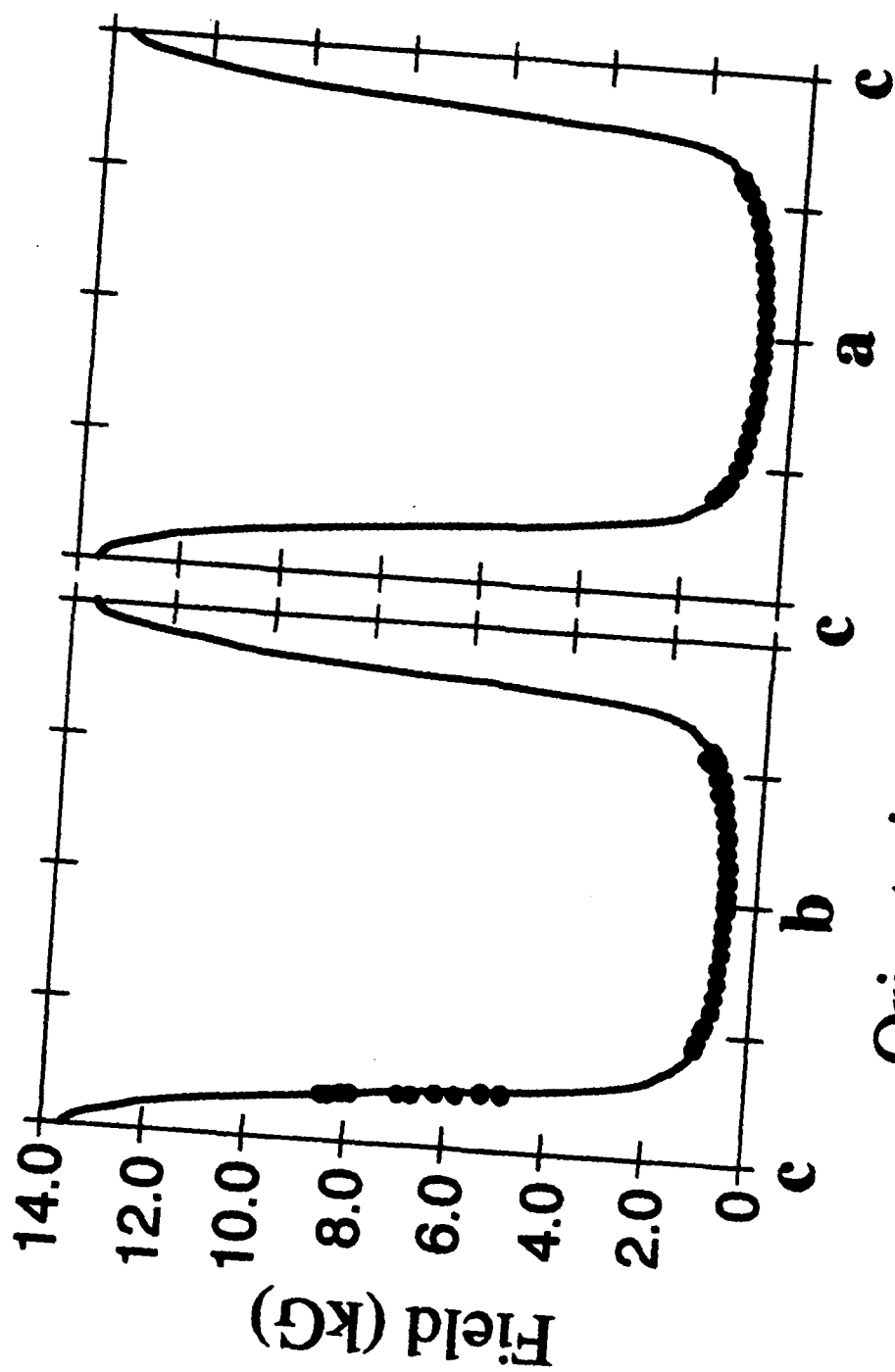
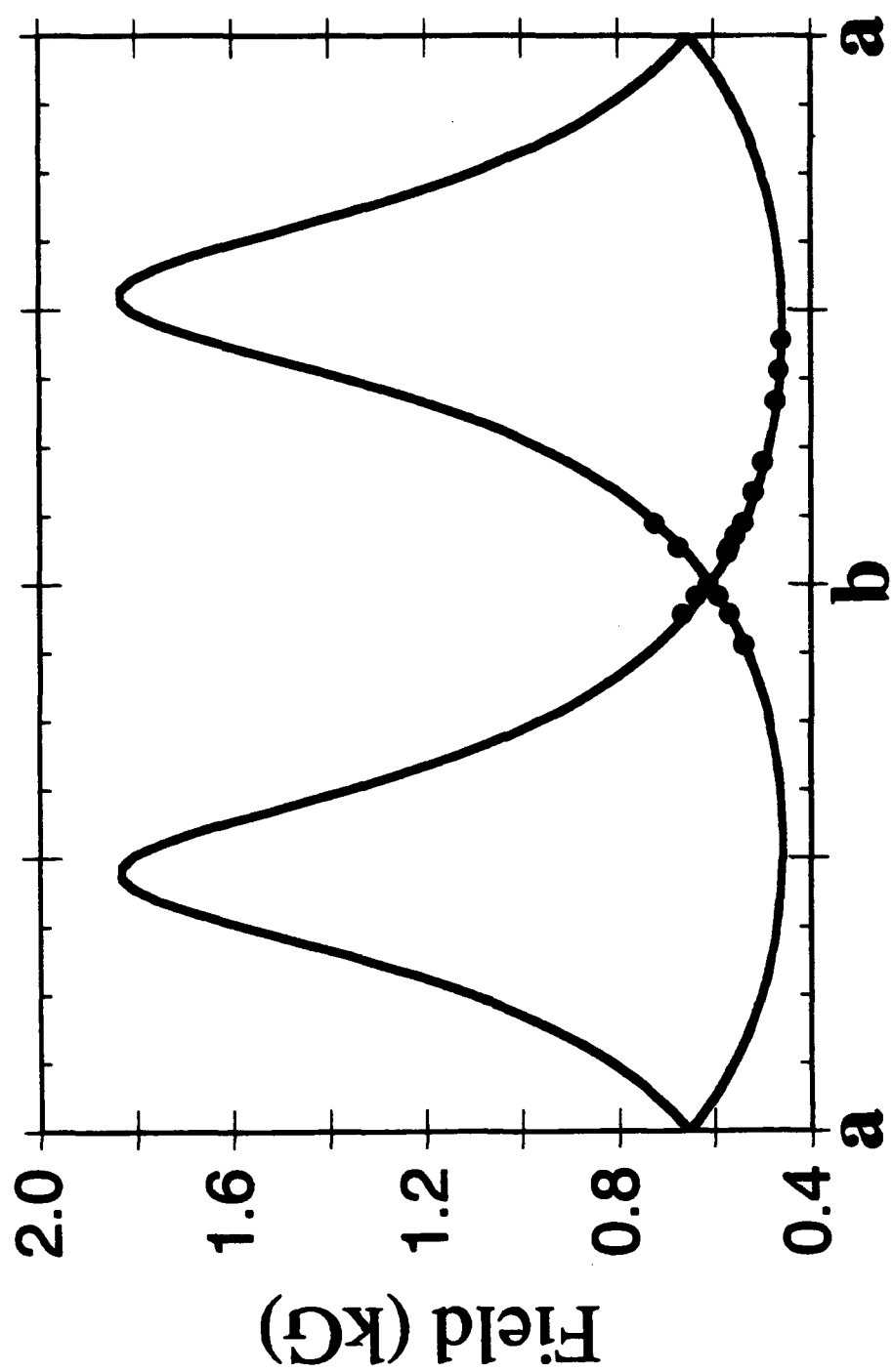


**FIG 2.16.** Field-for-resonance vs. orientation of  $B_0$  near the  $ab$  crystallographic plane for  $Cr^{4+}$  in forsterite. The points are experimental data, and the solid curves derive from the best fit spin-Hamiltonian parameters, as described in the text. In order to obtain this data, the crystal rotation axis was tilted about  $b$  to make an angle of  $\sim 0.1\pi$  with  $c$ .



Orientation of Magnetic Field

of a zero field splitting of resonant levels nearly equal to the microwave quantum,  $h\nu_\mu$  (where  $\nu_\mu$  is the microwave frequency and  $h$  is Planck's constant).

The latter observation obviously rules out a  $S=1/2$  system, which can have no zero field splitting. The assignment of the observed resonance lines to an  $S=1$  system, on the other hand, is completely consistent with the experimental observations. In typical experimental situations, if  $D \gg h\nu_\mu$  then only transitions between the levels split in zero field by  $2E$  are observed as illustrated in Figure 2.17. If the  $2E$  splitting is then assumed to be somewhat less than the microwave quantum, this solitary transition should be observable for any orientation of  $B_0$ . If, however,  $2E > h\nu_\mu$ , the separation of resonant energy levels is necessarily greater than  $h\nu_\mu$  and resonance is not attainable for any magnetic field orientations except those close to the median magnetic principal axis (conventionally labeled  $y$ ).

In order to account for the disappearance of the low field extrema in the  $ac$  and  $bc$  planes of forsterite,  $2E$  must lie between 9.1 and 9.2 GHz. In addition,  $y$  cannot coincide with  $a$  (or  $b$ ). Moreover, cursory comparison of  $|B_0|$  at the resonant field stationary points (which, by symmetry, occur when  $B_0$  is along  $c$  or in the  $ab$  plane) with the hierarchy of resonant field values for  $B_0 \parallel x$ ,  $y$ , and  $z$  (illustrated in Figure 2.17) reveals that  $y \parallel c$ , and that the  $x$  and  $z$  axes of the two magnetically inequivalent  $4c$  ions essentially bisect  $a$  and  $b$ . The relationship between  $\{x, y, z\}$  and the crystallographic frame is shown for one of these two ions in Figure 2.18.

The dependence of EPR signal intensities in the  $ab$  plane of forsterite on the orientation of  $B_1$  within the crystal is also consistent with the assignment of  $S=1$ . Inasmuch as the splitting between resonance levels is only slightly smaller than the microwave quantum, the EPR transitions occur at nearly zero field for all magnetic field orientations except those close to  $y$ . To the extent that the mixing of the zero field eigenstates,  $\{|T_x\rangle, |T_y\rangle, |T_z\rangle\}$ , by the small Zeeman interaction is negligible, these EPR transitions are subject to well-known selection rules involving the microwave field orientation.<sup>27</sup>

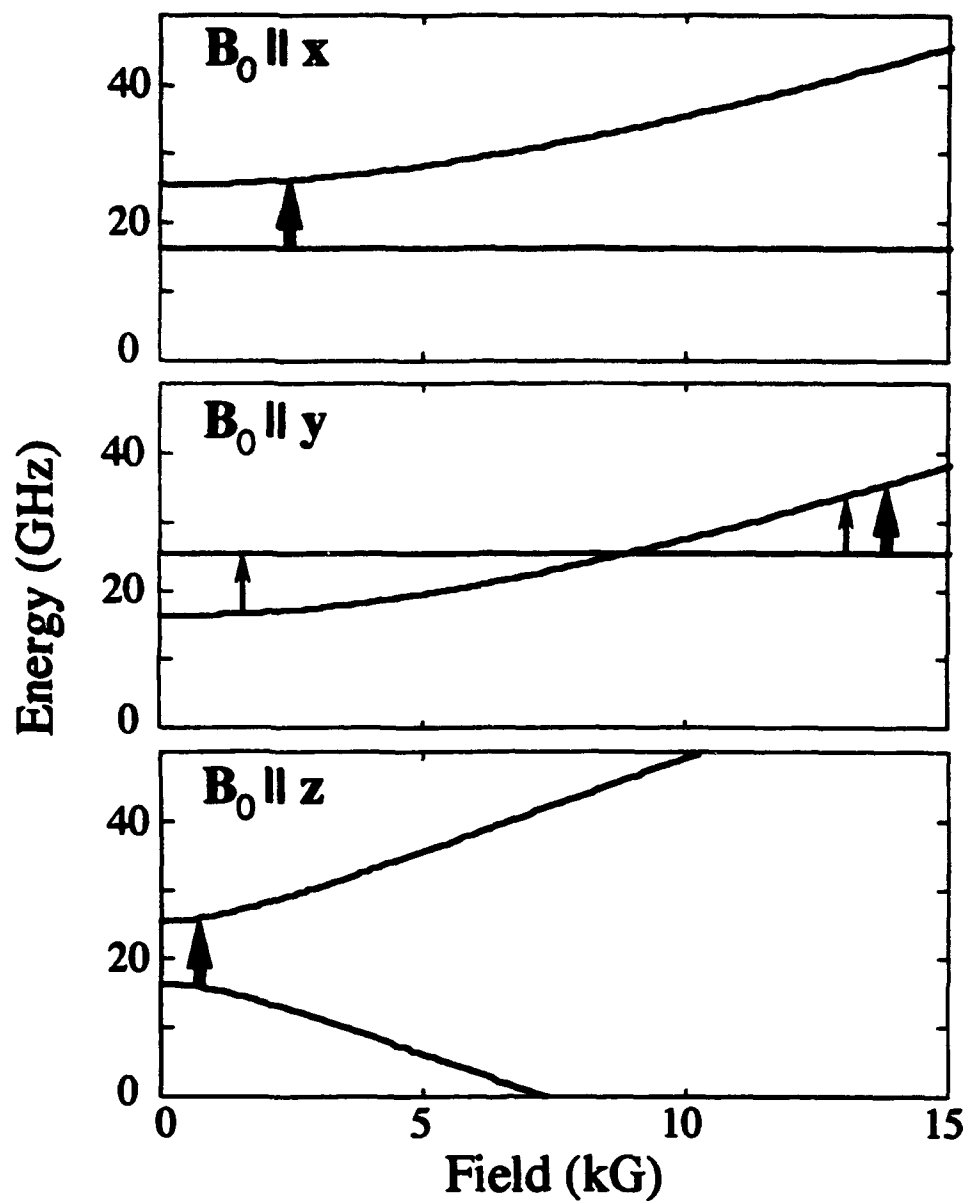
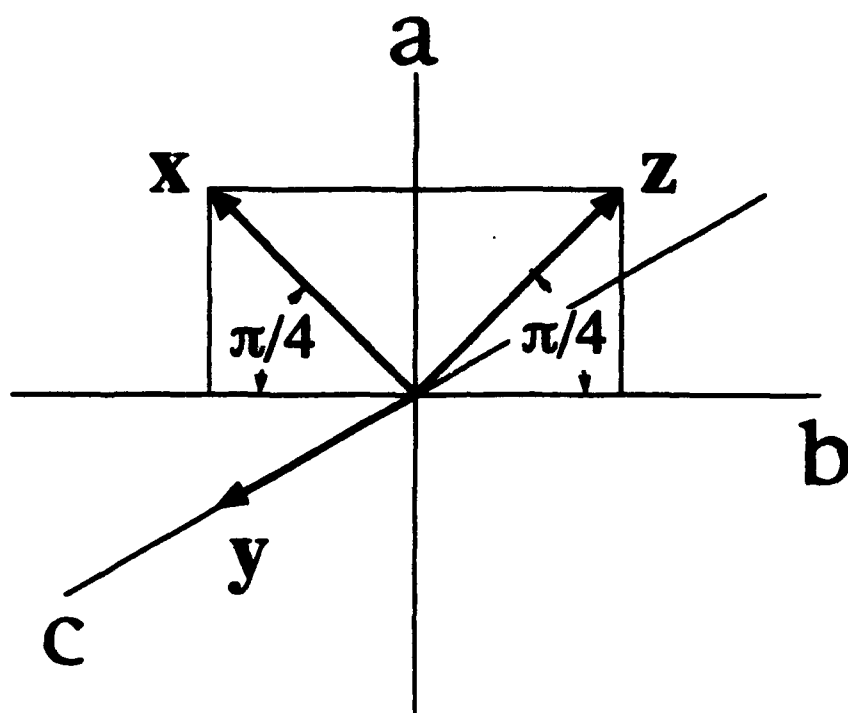


FIG 2.17. Upper two energy levels of the  $\text{Cr}^{4+}$  ground state spin triplet ( $D \gg h\nu_{\mu}$ ) with the magnetic field oriented along the three magnetic principal axes. The zero field splitting of these levels,  $2E$ , is 9.2 GHz. The thick arrows show the transitions possible at 9.5 GHz, while the thin arrows show the transitions possible at 9.1 GHz.





**FIG 2.18.** Orientation of the magnetic principal axes of one of the crystallographically equivalent  $\text{Cr}^{4+}$  ions in forsterite, relative to the crystallographic axes.

Examination of the axis system depicted in Figure 2.18, reveals that rotation of  $B_0$  in the  $ab$  crystallographic plane with  $B_1 \parallel c$  corresponds to an  $xz$  plane rotation with  $B_1 \parallel y$  in the internal axis systems of ions in the 4c sites of forsterite. Since the observed EPR transition occurs at nearly zero field, between states essentially equivalent to  $|T_x\rangle$  and  $|T_y\rangle$ , no EPR signal is observed. On the other hand, if the crystal is tilted such that  $B_1$  incorporates a non-zero  $z$ -component, the EPR transition is no longer forbidden.

For chromium-doped BMaG, similar arguments to those presented for forsterite demonstrate that the chromium EPR spectra can also be best explained assuming an  $S=1$  ion. A final demonstration of the soundness of this identification is the suitability of Eq. (2-1) for summarizing the EPR spectral results.

We employed Eq. (2-1) in evaluating the spin Hamiltonian parameters by least-squares fitting the observed fields-for-resonance. In this calculation we employed a Levenberg-Marquardt<sup>28</sup> non-linear fitting routine, together with an eigenfield algorithm based on the method described by Belford *et al.*<sup>29</sup> For both crystal systems, best values were calculated for  $D$ ,  $E$ , and the principal values of  $g$ , namely  $g_x$ ,  $g_y$ ,  $g_z$ , with the principal axes of  $g$  constrained to be coincident with the fine structure axes  $\{x,y,z\}$ .

In the case of forsterite, the fitted data was limited to fields-for-resonance observed with  $B_0$  in the  $ac$  and  $bc$  planes, where all ions are magnetically equivalent. The orientations of  $\{x,y,z\}$  were not fitted but set to values determined by symmetry and by inspection of the data in Figures 2.15 and 2.16. The direction cosines of the magnetic axes are shown in Table 2.6: the  $y$  axis is constrained to  $c$  and  $z$  is constrained to precisely bisect the  $a$  and  $b$ , as illustrated in Figure 2.18. This latter constraint is justified by the equivalence of resonant field data obtained with  $B_0$  in the  $ac$  and  $bc$  planes and by the location of the extrema in Figure 2.16. Best fit spin Hamiltonian parameter values are shown in Table 2.5 together with  $\delta_{rms}$ , the root mean squared deviation between the observed and calculated resonant field values. These best fit parameter values were used to generate the solid curves in

Parameter	Ba <sub>2</sub> MgGe <sub>2</sub> O <sub>7</sub>	Mg <sub>2</sub> SiO <sub>4</sub>
$\delta_{rms}$ (G)	8	3
D (GHz)	114.2 (0.4)	63. (1.)
E (GHz)	4.465 (0.001)	4.5885 (0.0003)
$g_x$	1.99 (0.01)	1.99 (0.02)
$g_y$	1.89 (0.04)	2.00 (0.01)
$g_z$	2.003 (0.003)	2.003 (0.001)

TABLE 2.5. Least-squares best fit values (standard deviations in parentheses) of the spin Hamiltonian parameters for Cr<sup>4+</sup> in BMaG and forsterite single crystals.

Crystal	Magnetic axis	Crystallographic axis		
		a	b	c
Ba <sub>2</sub> MgGe <sub>2</sub> O <sub>7</sub>	x	(+--+ )0.707	(+--+ )0.707	0.000
	y	(-++- )0.348	(+--+ )0.348	(+--+ )0.870
	z	(+--+ )0.615	(-++- )0.615	(+--+ )0.492
Mg <sub>2</sub> SiO <sub>4</sub>	x	±0.707	+0.707	0.000
	y	0.000	0.000	±1.000
	z	±0.707	+0.707	0.000

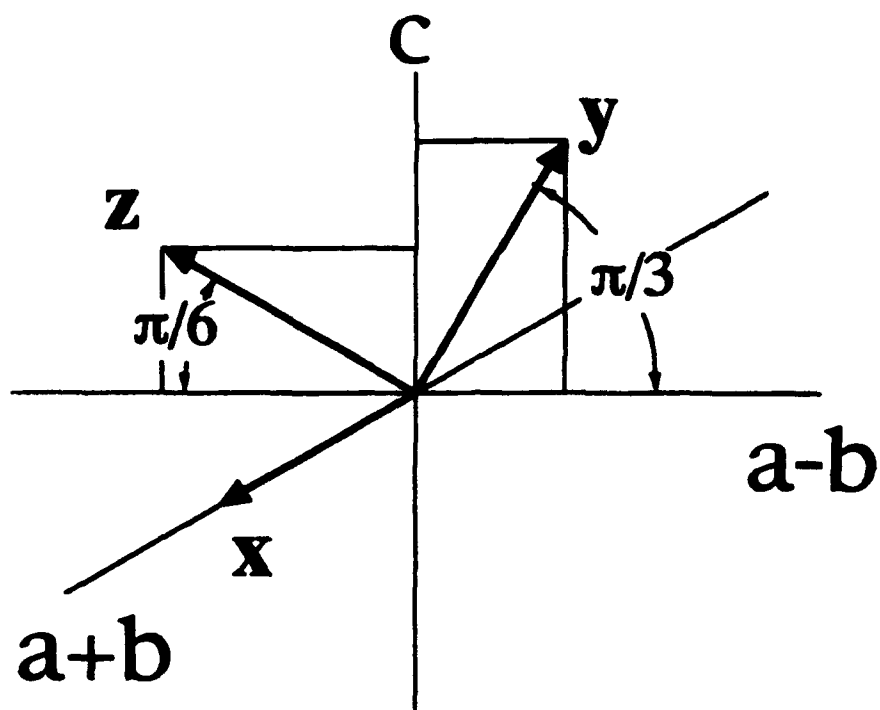
TABLE 2.6. Direction cosines of the coincident principal axes of the electron-Zeeman and fine-structure interactions in the crystal axis systems of BMaG and forsterite. The multiplicity of signs reflects the presence of four crystallographically equivalent sites in BMaG and two pairs of inversion related sites in forsterite

Figure 2.15. In addition, these parameter values were used to fit the data of Figure 2.16, obtained with  $B_0$  near the  $ab$  plane, by parametric variation of the tilt angle described above. The best fit, shown as the solid curve in Figure 2.16, corresponds to a tilt angle  $0.1\pi$ , a value that stands in good agreement with our *a priori* estimate.

For BMaG, we opted to fit the resonant field data that belongs to a selected one of the  $4e$  sites. Data observed with  $B_0$  rotation in the  $ab$ ,  $ac$ , and  $a+b,c$  planes was fit. In the latter plane, in which the EPR lines show a partially resolved splitting due to a slight misalignment of the crystal rotation axis, the average of the observed pair of resonant field values was used in the fit. Like the  $y$  axis in forsterite, the  $x$  axis in BMaG is assignable as the normal to the mirror symmetry plane. The orientation of the in-plane axes,  $y$  and  $z$ , was established by least-squares adjustment. Best-fit spin Hamiltonian parameter values are shown in Table 2.5; direction cosines of  $\{x,y,z\}$  in the crystallographic axis system are shown in Table 2.6. The solid lines in Figure 2.12 were calculated from the tabulated parameter values. The relation between the crystallographic and the magnetic axes of one of the crystallographically equivalent  $Cr^{4+}$  ions in BMaG is illustrated in Figure 2.19; all four sites are shown in Figure 2.20.

Transition intensities were calculated for both BMaG and forsterite based on the best fit spin Hamiltonian parameter values and were found to be consistent with the experimental observations. In particular, calculations for forsterite with  $B_1$  along  $c$  predict an EPR signal intensity that varies with the orientation of  $B_0$  in the  $ab$  plane from  $10^{-3}$  to  $10^{-5}$  times the average (and essentially constant) value found for  $B_1$  along either  $a$  or  $b$  as shown in Figure 2.21. A marked increase in intensity is also found if  $B_1$  is tilted away from  $c$ , consistent with our ability to obtain data near, but not in, the  $ab$  plane.

All arguments made for a chromium ion of triplet spin multiplicity should hold as well for transitions between the analogous levels of a  $S=2$   $Cr^{2+}$  ion, making a distinction based on the limited data obtainable somewhat difficult. Nevertheless, we reject the



**FIG 2.19.** Orientation of the magnetic principal axes of one of the crystallographically equivalent  $\text{Cr}^{4+}$  ions in BMaG, relative to the crystallographic axes.

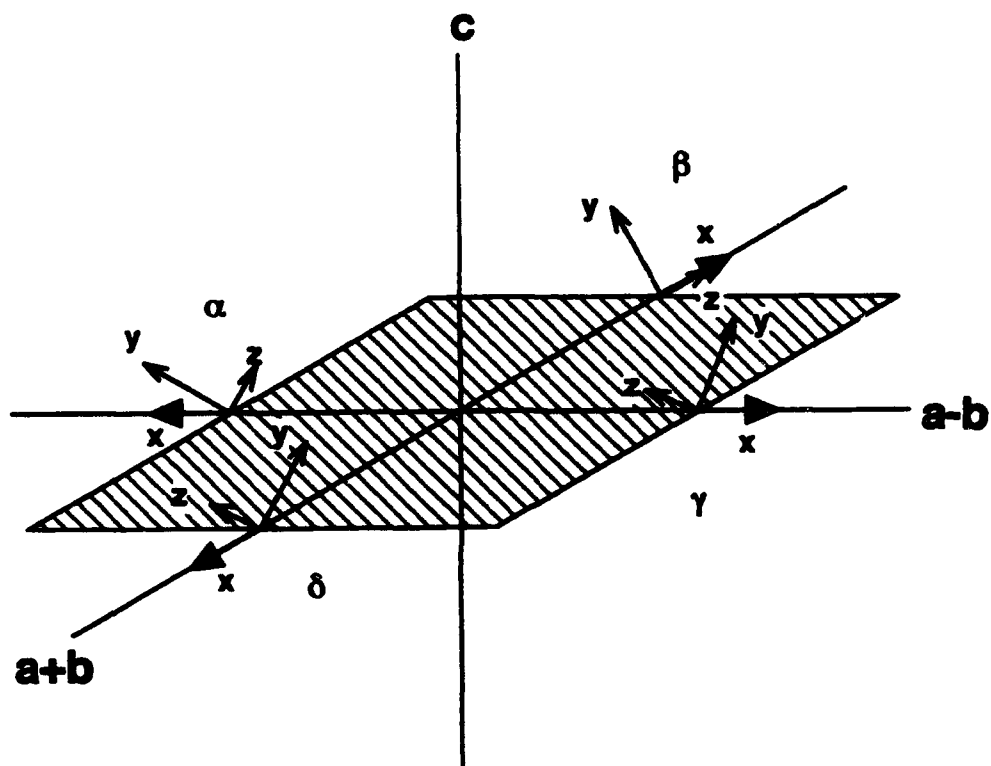


**FIG 2.20.** Orientation of the magnetic principal axes of the crystallographically equivalent  $\text{Cr}^{4+}$  ions in  $\text{BMaG}$ , relative to the crystallographic axes.

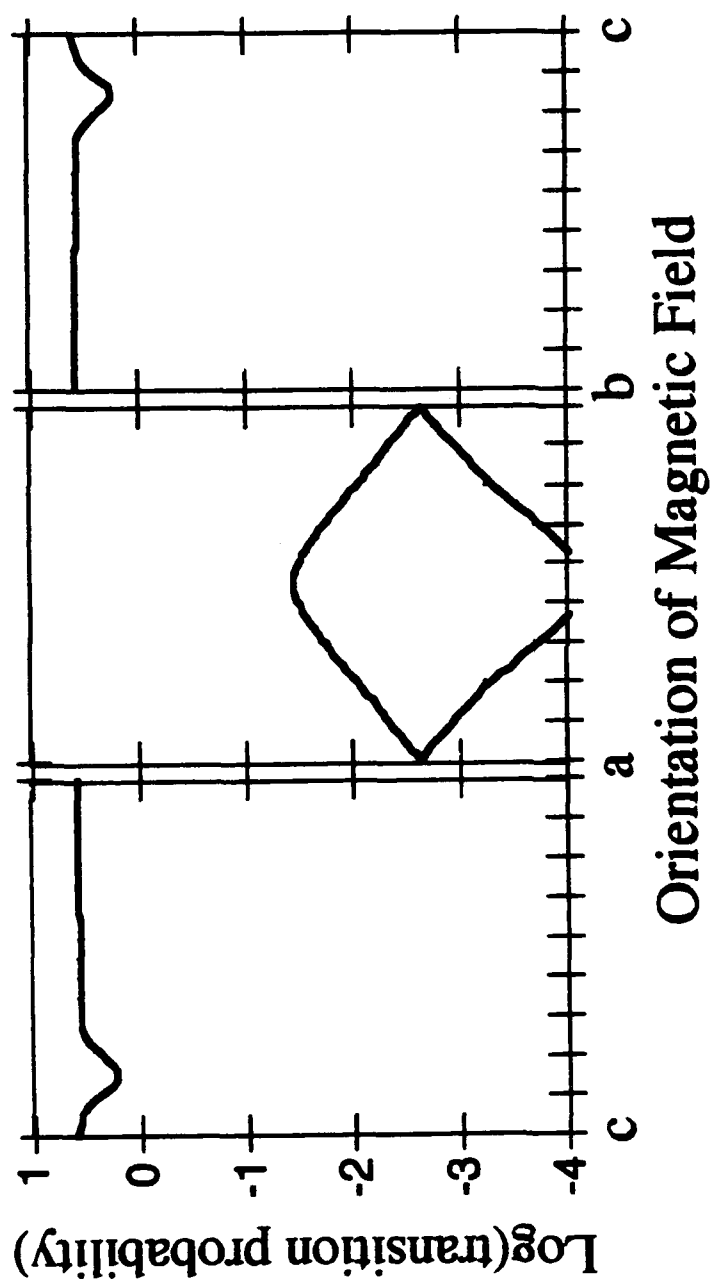


**FIG 2.21.** Log of transition probability vs. orientation of  $B_0$  in the *ac*, *ab* and *bc* crystallographic planes in forsterite.

possibility of  $S=2$  for two reasons. First, the materials studied here were prepared under conditions designed to favor incorporation of high oxidation states of chromium. Second paramagnetic  $d^4$  ions possess orbitally degenerate ground states in both octahedral and tetrahedral fields — making it unlikely that signals would be observable at room temperature.

## VI. DISCUSSION

The EPR spectra of chromium-doped BMaG and forsterite single crystals demonstrate the inclusion of chromium ions at the 4e sites of BMaG and the 4c sites of forsterite. The orientation dependence of the EPR resonant fields and signal intensities reveals the triplet spin multiplicity of the chromium center consistent with its identification as  $Cr^{4+}$ . This assignment is supported by our ability to observe the spectra at room temperature.

The 4e position in BMaG encompasses both  $Ba^{2+}$  and  $Ge^{4+}$  sites. Nevertheless, it is certain that the  $Cr^{4+}$  ion, with an ionic radius of 0.56 Å, would be incorporated substitutionally for the more nearly equivalent tetrahedral  $Ge^{4+}$  ion (0.53 Å), rather than the much larger  $Ba^{2+}$  ion (1.56 Å).<sup>30</sup> The similarity, detailed below, between the  $Cr^{4+}$  EPR spectra in BMaG and those in forsterite suggests a corresponding similarity in substitution sites in the crystals. We therefore conclude that the  $Cr^{4+}$  ion substitutes at the tetrahedral  $Si^{4+}$  site rather than the octahedral  $Mg^{2+}$  site in forsterite.

Comparison of the Hamiltonian parameters found for the  $Cr^{4+}$  ion in BMaG and in forsterite reveals a number of similarities. In both systems the value of  $D$  is rather large (*vide infra*), on the order of  $1\text{ cm}^{-1}$ . Moreover, the value of  $E/D$ , which gauges the departure of fine structure interaction from axial symmetry, is very small in both systems: 0.04 in BMaG and 0.07 in forsterite. The principal values of  $g$  are all very close to the free electron  $g$ -value. In particular, the  $g_z$  values, which are most precisely determined, are essentially the equal in both systems to the free electron value.



As a final point of comparison, it is interesting to consider the orientation of the major axis of the fine structure interaction,  $z$ , within the  $\text{SiO}_4^{4-}/\text{GeO}_4^{4-}$  tetrahedra. In BMaG and in forsterite the axis that is constrained by symmetry to lie normal to the mirror plane is one of the minor axes; the major axis must therefore lie in the mirror plane. Because of crystallographic equivalences, a dilemma exists regarding the orientation of  $z$  within the  $\text{GeO}_4^{4-}$  tetrahedra of BMaG and the  $\text{SiO}_4^{4-}$  tetrahedra of forsterite. For one assignment of  $z$  orientations, however, we are able to find a common motif: approximate alignment of  $z$  along the bisector of the two equivalent (mirror-symmetry related) Si/Ge-O bonds. It is interesting to note, that a distorted tetrahedron of  $C_{2v}$  symmetry is required by symmetry to possess the configuration of magnetic axes implied by this assignment. On the other hand, the presence of a significantly shortened bond within the tetrahedra (see Figure 2.9) raises the possibility that  $\text{Cr}^{4+}$  ions centered in them might more closely reflect an approximate  $C_{3v}$  symmetry in their properties. From this perspective, the major axis in forsterite would be constrained to lie close to  $a$ , and in BMaG, close to  $c$ . Neither of these anticipated alignments is borne out experimentally. The location of the fine-structure major axis in these crystals thus gives insight into the dominant components of the crystal-field at the  $\text{Cr}^{4+}$  occupied tetrahedral sites.

In view of the close similarity between BMaG and CMSO, the lack of detectable  $\text{Cr}^{4+}$  EPR signals in the latter is puzzling. We believe that our inability to detect chromium EPR absorptions in CMSO is precipitated by the presence of a 2E splitting that is slightly larger than any microwave frequency utilized in our study. The large splitting would make signal detection impossible in all but a potentially very narrow range of  $B_0$  orientations. Studies of this system are continuing.

EPR spectroscopy of tetrahedral  $\text{Cr}^{4+}$  in organometallic compounds has been reported previously.<sup>31,32,33</sup> The fine structure interactions found in these systems are much smaller than in BMaG and forsterite, with D values of  $\sim 1$  GHz. Similar results have also been found for other  $3d^2$  ions, including as  $\text{Ti}^{2+}$ ,<sup>34-37</sup>  $\text{V}^{3+}$ ,<sup>38-42</sup>  $\text{Fe}^{4+}$ ,<sup>43,44</sup> and

Mn<sup>5+</sup>,<sup>43,45,46</sup> in tetrahedral sites within a number of single crystal hosts. This disparity in D-values is presumably related to the relatively large distortions of the CrO<sub>4</sub><sup>4-</sup> tetrahedra in BMaG and forsterite. Yen and co-workers<sup>9</sup> employed their analysis of the optical spectrum of Cr<sup>4+</sup> in forsterite to estimate D and E values of approximately 23 and 4 GHz respectively. This estimate of D, although several times smaller than the value observed experimentally, is of an agreeable order of magnitude, and is decidedly larger than observed in previously studied 3d<sup>2</sup> systems. The estimated E value corresponds extremely well with the experimental result.

A preliminary version of the results given here was presented in at the 1991 OSA conference on solid state lasers.<sup>23</sup> At that time, Baryshevski *et al.*<sup>11</sup> reported D and E values, together with an isotropic g-value, for a Cr<sup>4+</sup> center in forsterite. These values were in good agreement with those reported by us. Concurrently, Yen and co-workers<sup>47</sup> presented EPR data from a number of different centers in forsterite and suggested assignments involving Cr<sup>4+</sup> in the M1 and M2 octahedral sites or Cr<sup>2+</sup> in either the octahedral or tetrahedral sites. They concluded that none of the signals that they characterized could be assigned as the NIR laser active site.<sup>47</sup> More recently, the Yen group<sup>12</sup> has also reported the observation of spectra identical to those obtained by both Baryshevski *et al.*<sup>11</sup> and us. A broad consensus for the presence of tetrahedrally coordinate, S=1, Cr<sup>4+</sup> ions in forsterite has thus emerged. The results and analysis presented here represent the first detailed account of the observations and the reasoning upon which this consensus is founded.<sup>48</sup>

Although EPR results alone cannot establish the connection between the presence of Cr<sup>4+</sup> ions and the NIR laser center in chromium-doped forsterite, several studies have been conducted that make this connection clear. Baryshevski *et al.* demonstrated that transient changes in the intensity of the Cr<sup>4+</sup> EPR signal could be induced by optical excitation at spectral regions corresponding to absorption bands of the lasing center.<sup>11</sup> Concurrently, Yen and co-workers<sup>13</sup> used FLN (fluorescence line narrowing) techniques to resolve a 60 GHz zero field splitting within the electronic ground state. An elaboration of these experi-

ments later provided compelling evidence for the equivalence of the  $\text{Cr}^{4+}$  EPR center and the NIR laser center. In FLN-assisted optical Zeeman experiments, Rose *et al.*<sup>14</sup> found a striking correspondence between  $B_0$ -dependence of the ground state splittings observed experimentally and those predicted based on the EPR parameters reported here.<sup>14</sup> These experiments also show that D is positive.<sup>14</sup> Complementary studies, yielding similar results have also been reported by Yen *et al.*<sup>12</sup>

#### ACKNOWLEDGEMENTS

Support of this work by the Army Research Office (DAAL03-90-0113) and the Rowland Fund (to AS) is gratefully acknowledged. We also wish to thank for Dr. R. C. Morris of Allied-Signal Corporation, Professor D. J. Simkin of McGill University, Dr. H. R. Verdún of Fibertek, and Professor H. P. Jenssen of MIT for supplying crystals used in this work. We gratefully acknowledge the generous assistance of Dr. Ralph T. Weber of Bruker Instruments in making certain experiments possible. Finally we wish to thank Dr. Renny A. Fields of the Aerospace Corporation and Dr. A. Pinto of the Army Night Vision Laboratory who introduced us to this problem and provided valuable advice and suggestions that helped us to solve it.

## REFERENCES

- [1] Petricevic, V., Gayen, S. K., Alfano, R. R., Yamagishi, K., Anzai, H., and Yamaguchi, Y., *Appl. Phys. Lett.* **52**, 1040 (1988).
- [2] Petricevic, V., Gayen, S. K., and Alfano, R. R., *Appl. Phys. Lett.* **53**, 2590 (1988).
- [3] Verdún, H. R., Thomas, L. M., Andrauskas, D. M., McCollum, T., and Pinto, A., *Appl. Phys. Lett.* **53**, 2593 (1988).
- [4] Stokowski, S. E., Randles, M. H., and Morris, R. C., *J. Quant. Elect.* **24**, 934 (1988).
- [5] Petricevic, V., Gayen, S. K., and Alfano, R. R., in *OSA Proceedings on Tunable Solid State Lasers*, edited by Shand, M. L. and Jensen, H. P. (Optical Society of America, Washington, DC, 1989), Vol. 5, p. 77.
- [6] Verdún, H. R., Thomas, L. M., Andrauskas, D. M., and Pinto, A., in *OSA Proceedings on Tunable Solid State Lasers*, edited by Shand, M. L. and Jensen, H. P. (Optical Society of America, Washington, DC, 1989), Vol. 5, p. 85.
- [7] Moncorgé, R., Simkin, D. J., Cormier, G., and Capobianco, J. A., in *OSA Proceedings on Tunable Solid State Lasers*, edited by Shand, M. L. and Jensen, H. P. (Optical Society of America, Washington, DC, 1989), Vol. 5, p. 93.
- [8] Jia, W., Lu, L., Tissue, B. M., and Yen, W. M., *J. Cryst. Growth* **109**, 329 (1991).
- [9] Jia, W., Liu, H., Jaffe, S., Yen, W. M., and Denker, B., *Phys. Rev. B* **43**, 5234 (1991).
- [10] Moncorgé, R., Cormier, G., Simkin, D. J., and Capobianco, J. A., *IEEE J. Quantum Electron.* **27**, 114 (1991).
- [11] Baryshevski, V. G., Korzhik, M. V., Livshitz, M. G., Tarasov, A. A., Kimaev, A. E., Mishel, I. I., Meilman, M. L., Minkov, B. J., and Shkandarevich, A. P., in *OSA Proceedings on Tunable Solid State Lasers*, (Optical Society of America, 1991), .
- [12] Hoffman, K. R., Casas-Gonzalez, J., Jacobsen, S. M., and Yen, W. M., *Phys. Rev. B* **44**, 12589 (1991).
- [13] Hoffman, K. R., Jacobsen, S. M., Casas-Gonzalez, J., and Yen, W. M., in *OSA Proceedings on Advanced Solid State Lasers*, edited by Dubé, G. and Chase, L. (Optical Society of America, Washington, DC, 1991), Vol. 10, p. 44.
- [14] Rose, T. S., Fields, R. A., Whitmore, M. H., and Singel, D. J., in *OSA Proceedings on Advanced Solid-State Lasers*, edited by Chase, L. L. and Pinto, A. A. (Optical Society of America, Washington, DC, 1992), Vol. 13, p. 17. Rose, T. S., Whitmore, M. H., Fields, R. A., and Singel, D. J., *J. Opt. Soc. Amer.: B*, submitted for publication.
- [15] Rager, H., *Phys. Chem. Minerals* **1**, 371 (1977).
- [16] Bershov, L. V., Gaite, J. M., Hafner, S. S., and Rager, H., *Phys. Chem. Minerals* **9**, 95 (1983).
- [17] Nagel, S. and Rager, H., *Phys. Chem. Minerals* **12**, 291 (1985).
- [18] Smyth, J. R. and Hazen, R. M., *Am. Mineral.* **58**, 588 (1973).

- [19] Allik, T. H., Ferry, M. J., Reeves, R. J., Powell, R. C., Hovis, W. W., Caffey, D. P., Utano, R. A., Merkle, L., and Campana, C. F., *J. Opt. Soc. Am. B* **7**, 1190 (1990).
- [20] Smith, J. V., *Amer. Min.* **38**, 643 (1953).
- [21] In åkermanite the crystallographic axes that we refer to as a and b are equivalent and are both properly labeled as a; in the interest of clarity, however, we prefer the distinct, though arbitrary, designations.
- [22] Abragam, A. and Bleaney, B., *Electron Paramagnetic Resonance of Transition Ions* (Dover Publications, Inc., New York, NY, 1970).
- [23] Garret, M. H., Chan, V. H., Jensen, H. P., Whitmore, M. H., Sacra, A., Singel, D. J., and Simkin, D. J., in *OSA Proceedings on Advanced Solid-State Lasers*, edited by Dubé, G. and Chase, L. (Optical Society of America, Washington, DC, 1991), Vol. 10, p. 76.
- [24] Using Miller indices these planes are the (001), (010), and (1-10) respectively.
- [25] Wertz, J. E. and Bolton, J. R., *Electron Spin Resonance* (Chapman and Hall, New York, NY, 1986).
- [26] Geschwind, S., *Phys. Rev.* **121**, 363 (1961).
- [27] The eigenstates,  $|T_u\rangle$ , of the zero field spin Hamiltonian,  

$$H = D(S_z^2 - S^2/3) + E(S_x^2 - S_y^2),$$
 have the property  $S_u|T_u\rangle = 0$ , where  $u = x, y, z$ , the principal axis of the fine structure matrix  $D$ . The transition probability between the states  $|T_x\rangle$  and  $|T_y\rangle$ , which are separated by  $2E$ , is therefore zero if  $B_1$  has no component along  $z$ .
- [28] Press, W. H., Flannery, B. P., Teukolsky, S. A., and Vetterling, W. T., *Numerical Recipes* (Cambridge University Press, , 1986).
- [29] Belford, G. G., Belford, R. L., and Burkhalter, J. F., *J. Mag. Res.* **11**, 251 (1973).
- [30] Huheey, J. E., *Inorganic Chemistry* (Harper and Row, New York, NY, 1983).
- [31] Mowat, W., Shortland, A., Yagupsky, G., Hill, N. J., Yagupsky, M., and Wilkinson, G., *J. C. S. Dalton* (7), 533 (1972).
- [32] Mowat, W., Shortland, A. J., Hill, N. J., and Wilkinson, G., *J. C. S. Dalton* (4), 770 (1973).
- [33] Alyea, E. C., Basi, J. S., Bradley, D. C., and Chisholm, M. H., *J. Chem. Soc. A* **5**, 772 (1971).
- [34] Schneider, J. and Räuber, A., *Phys. Lett.* **21**, 380 (1966).
- [35] Dziesiaty, J. and Böttcher, R., *Phys. Stat. Sol.* **26**, K21 (1968).
- [36] Zaripov, M. M., Kropotov, V. S., and Livanova, L. D., *Fiz. Tverd. Tela* **9**, 1265 (1967).

- [37] Zaripov, M. M., Kropotov, V. S., Livanova, L. D., and Stepanov, V. G., *Fiz. Tverd. Tela* **9**, 2985 (1967).
- [38] Holton, W. C., Schneider, J., and Estle, T. L., *Phys. Rev.* **133**, A1638 (1964).
- [39] Woodbury, H. H. and Ludwig, G. W., *Bull. Am. Phys. Soc.* **6**, 118 (1961).
- [40] Zaripov, M. M., Kropotov, V. S., Livanova, L. D., and Stepanov, V. G., *Fiz. Tverd. Tela* **9**, 209 (1967).
- [41] Zaripov, M. M., Kropotov, V. S., Livanova, L. D., and Stepanov, V. G., *Doklady AN SSSR* **173**, 1043 (1967).
- [42] Zaripov, M. M., Kropotov, V. S., Livanova, L. D., and Stepanov, V. G., *Fiz. Tverd. Tela* **10**, 325 (1968).
- [43] Carrington, A., Ingram, D. J. E., Lott, K. A. K., Schonland, D. S., and Symons, M. C. R., *Proc. R. Soc.* **A254**, 101 (1960).
- [44] Debuyst, R., Dejehet, F., and Apers, D., *J. Inorg. Nucl. Chem.* **37**, 338 (1975).
- [45] Lachwa, H. and Reinen, D., *Inorg. Chem.* **28**, 1044 (1989).
- [46] Scharmann, A., Vitt, B., Hoppe, R., and Meyer, G., *Phys. Stat. Sol.* **72**, 197 (1975).
- [47] Casas-Gonzalez, J., Jacobsen, S. M., Hoffman, K. R., and Yen, W. M., in *OSA Proceedings on Advanced Solid-State Lasers*, edited by Dubé, G. and Chase, L. (Optical Society of America, Washington, DC, 1991), Vol. 10, p. 64.
- [48] In examining the Hamiltonian parameter values determined by various research groups, the temperatures at which the experiments were carried out should be noted. We have observed a significant temperature dependence of the fine structure parameters, specifically an increase  $E$  as the temperature is reduced.
- [49] F. M. Henry and K. Lonsdale eds., *International Tables for X-Ray Crystallography* (Kynock Press, 1965).

## **Chapter 3**

### **Unequivocal Identification of the Cr<sup>4+</sup> Lasing Center in Cr:Forsterite.**

# Unequivocal Identification of the $\text{Cr}^{4+}$ Lasing Center in Cr:Forsterite

T. S. Roae<sup>†</sup> and R. A. Fields<sup>†</sup>

*Electronics Technology Center, The Aerospace Corporation, M2/246, PO Box 92957,  
Los Angeles, California 90009*

M. H. Whinnere<sup>‡</sup> and D. J. Singel<sup>‡</sup>

*Department of Chemistry, Harvard University, 12 Oxford Street, Cambridge, Massachusetts 02138*

## Abstract

Optical Zeeman experiments were performed on Cr:forsterite with the magnetic field applied along the crystallographic *a* and *c* axes. The strong agreement between these optical results and previous EPR studies for both alignments establishes the identity of the near infrared emission center as tetrahedral  $\text{Cr}^{4+}$ .

## Introduction

Since the first report [1] of the NIR (near infrared) laser action in Cr-doped forsterite ( $\text{Mg}_2\text{SiO}_4$ ), considerable effort has been made toward the determination of the nature of the lasing center. Initially it was suggested that the active center is  $\text{Cr}^{3+}$ , substituting for  $\text{Mg}^{2+}$ , at the octahedral lattice sites [1]. Subsequent to the realization that the NIR emission could be stimulated via excitation at 1064 nm [2,3] an alternative assignment was proposed: by analogy to the tetra-oxo  $\text{Cr}^{4+}$  center responsible for parasitic absorption in Cr activated Nd:YAG [4], the lasing center in forsterite was assigned to  $\text{Cr}^{4+}$  located at the tetrahedral silicate sites [2,3].

The presence of a tetrahedral  $\text{Cr}^{4+}$  center in Cr:forsterite was confirmed by EPR (electron paramagnetic resonance) spectroscopy [5,6]. Specifically, Singel and co-workers identified the spectrum of a ground state triplet spin species accommodated at the crystallographic 4c site which exhibited an intensity that varied directly with the Cr content of the crystal [5]. While both the octahedral  $\text{Mg}^{2+}$  and tetrahedral  $\text{Si}^{4+}$  centers lie at 4c sites in forsterite, the similarity of the forsterite spectra to those of Cr-doped BMAG ( $\text{Ba}_2\text{MgGe}_2\text{O}_7$ ), which unambiguously derive from

substitutional incorporation of  $\text{Cr}^{4+}$  at the tetrahedral Ge sites [5], argues that the relevant forsterite center is tetrahedral. Analysis of the forsterite spectrum in terms of the conventional triplet spin Hamiltonian yielded parameter values of  $D = 63. \pm 1$  GHz,  $E = 4.5885 \pm 0.0003$  GHz,  $g_x = 1.99 \pm 0.02$ ,  $g_y = 2.00 \pm 0.01$ , and  $g_z = 2.003 \pm 0.002$ , with the *x*, *y* and *z* principal axes respectively oriented along the  $a \pm b$ , *c*, and  $\pm a-b$  axes for the two sets of magnetically non-equivalent centers [7]. A concurrent EPR study by Baryshevski et al. [6], yielded very similar parameter values.

While EPR studies have confirmed the presence of tetrahedral  $\text{Cr}^{4+}$  in forsterite, the connection between this paramagnetic center and the NIR laser center remains to be firmly established. Two initial steps have been made toward reaching this goal. First, Baryshevski et al. [6], showed that optical excitation at wavelengths corresponding to the absorption maxima of the lasing center in forsterite causes a transient perturbation of the intensity of the  $\text{Cr}^{4+}$  EPR signal. Second, Yen and co-workers [8] employed FLN (fluorescence line narrowing) methods to resolve a  $2 \text{ cm}^{-1}$  splitting in the NIR emission of Cr:forsterite. This splitting accurately reflects the resolvable ground state sublevel structure expected in zero external magnetic field for the triplet species characterized by EPR (with  $D \pm E \approx 2 \text{ cm}^{-1}$ ). The zero-field FLN spectra are of limited value, however, for correlating the EPR and optical centers: the ground state sublevel structure is only partially characterized, and the orientation of the fine-structure axes is utterly undetermined by these experiments.

We have therefore extended the FLN measurements by examining the dependence of the ground



state sublevel splittings on both the magnitude and direction of an applied magnetic field. These Zeeman experiments demonstrate that the ground state of the optical center shares all of the defining properties—the fine-structure tensor principal values and principal axis orientations—of the center characterized by EPR, and thus provide compelling evidence for the common identity of the two centers. During the course of our measurements we became aware of similar Zeeman studies being conducted by others, in which the external field was aligned along the *b* crystallographic axis [9,10]. We report results obtained with the field along the *a* and *c* axes.

### Experimental

The Cr:forsterite crystal, obtained from Allied-Signal Corp., was placed inside a liquid helium cryostat fitted with a superconducting 6 Tesla high homogeneity magnet and maintained at a temperature of  $-2$  K for the experiments. As displayed in Fig. 1, the crystal was oriented such that the optical excitation was polarized vertically along the crystal *b* axis (Pbm crystal system [11]). The fluorescence was detected normal to the pump direction and parallel to the magnetic field. Rotation of the crystal about the *b* axis allowed the magnetic field to be oriented along the crystal *c* axis (i.e., the *y* principal axis of the zero-field splitting tensor [5]) or along the crystal *a* axis. In both settings, all centers at the 4*c* sites are magnetically equivalent.

Optical excitation of the forsterite crystal was achieved with an argon-ion pumped Ti:sapphire laser (50–100 mW, .01–.02  $\text{cm}^{-1}$  bandwidth) tuned into the three distinct energy sublevels of the lowest lying ex-

cited triplet spin state,  $^3A$ . The excitation wavelengths, 10891 Å, 10913 Å and 10927.5 Å, yielded the maximum zero-field fluorescence at 10930 Å, which corresponds to the energy gap between the lowest sublevel of the excited  $^3A^*$  [12] and the nearly degenerate upper two sublevels of the  $^3A^*$  ground state manifold [13]. The fluorescence was focussed into a 3/4 meter monochromator and detected with a photomultiplier tube and photon counting system. In order to suppress the laser scatter when pumping into the lowest lying excited state 10927.5 Å, the laser beam was deflected by an AO modulator which provided 10  $\mu\text{sec}$  pulses. Fluorescence was then detected after a 1  $\mu\text{sec}$  delay. Spectra were recorded for magnetic field strengths ranging from 0 to 5 Tesla.

### Results and Discussion

Exemplary FLN spectra, obtained following excitation into the upper sublevel of the lowest excited spin triplet, with the field aligned along the crystallographic *c*, axis are displayed in Fig 2. In the presence of inhomogeneous broadening, the narrow band laser excites  $\text{Cr}^{4+}$  ions from each of the thermally populated ground state sublevels to a selected one of the well separated sublevels of the excited state, as illustrated in Fig. 3. Inasmuch as the resonant excitation selects distinct  $\text{Cr}^{4+}$  sites, three excited state populations are generated. These excited state populations undergo rapid internal conversion to the lowest sublevel of the excited state and then emit to the three ground state sublevels. In principal, nine distinct FLN lines could be detected. However, we typically observe only two to five lines, since 1) the sublevels splittings are not resolvable at certain field values, 2) certain lines are expected to be of negligible intensity and 3) three of the lines, those that involve excitation from and emission to the same ground state sublevel are necessarily coincident at all field values. This latter set of lines is easily identified in the FLN spectra because it maintains a constant offset from the laser wavelength, independent of the magnetic field strength; this spectral feature is highlighted by the dotted line in Fig 2. The identification of this feature greatly facilitates the assignment of the other lines appearing in the FLN spectra. From the observed separation of the lines in the spectra, one can obtain the energy differences between the ground state sublevels and calculate their energies relative to a constant center-of-gravity at zero energy. In Fig. 4, these experimental energy values derived from the FLN data are plotted as a function of the external magnetic field (applied along the *a*

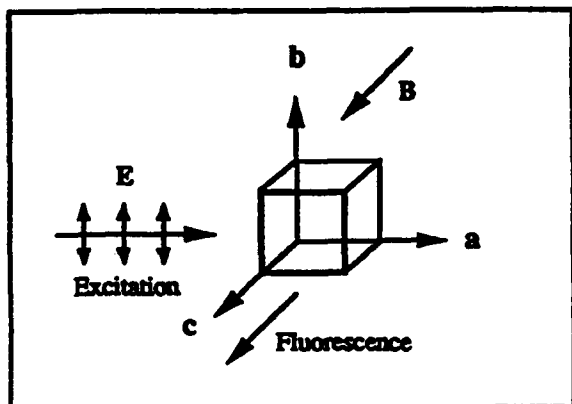


Figure 1. Orientation of the Cr:forsterite crystal and the optical and magnetic fields for the Zeeman experiments. *B* || *c* is illustrated.

and c axes) and compared to the theoretical behavior predicted from the spin Hamiltonian parameters, tabulated above, for the center characterized by EPR. Note that while a clear distinction in behavior exists for the magnetic field oriented along a or c, the agree-

ment between the FLN and EPR data is excellent for both orientations. These results provide compelling evidence that the EPR and optical center have the same identity, thereby identifying tetrahedral  $\text{Cr}^{4+}$  as the source of the NIR emission in Cr:forsterite.

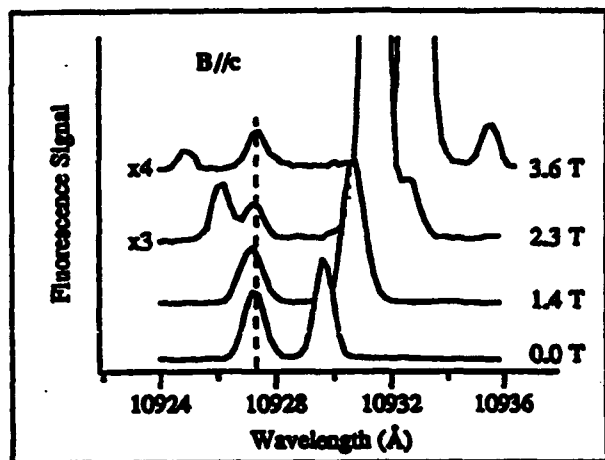


Figure 2. FLN spectra recorded at the indicated magnetic field strengths (in Tesla) applied along the crystallographic c axis. The laser wavelength was 10891 Å.

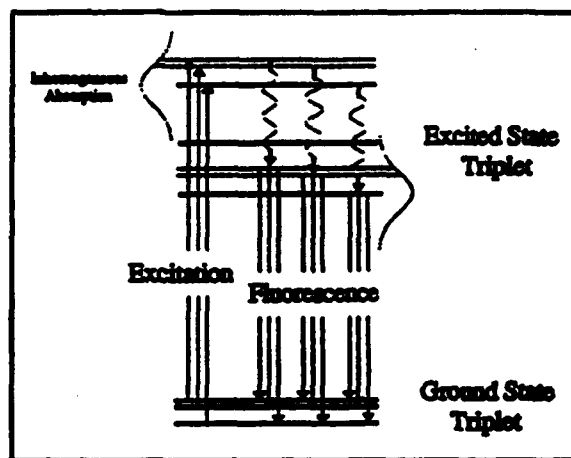


Figure 3. Illustration of nine possible fluorescence transitions in an inhomogeneously broadened  $\text{Cr}^{4+}$  system.

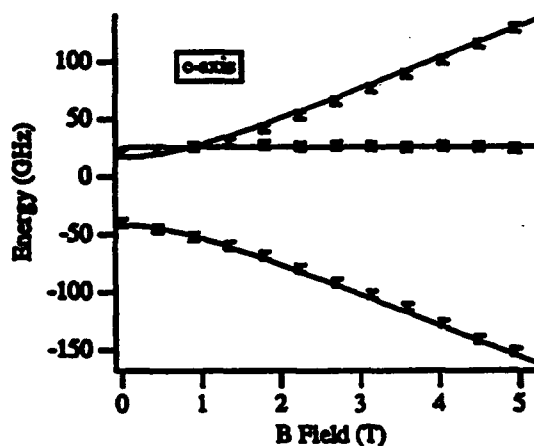
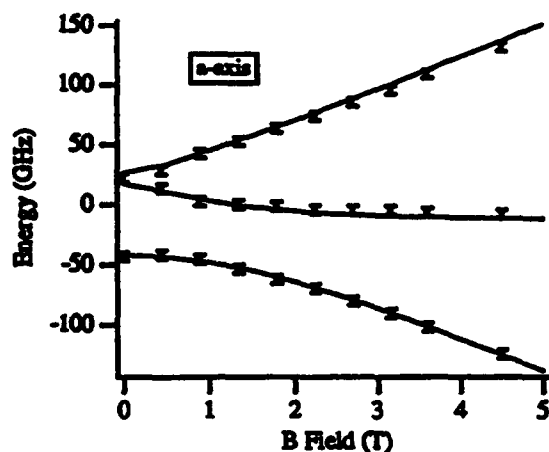


Figure 4. Comparison of energies derived from FLN spectra (points with error bars) to those predicted by EPR (solid curves). At field intensities where the energy levels were unresolved, a single point is drawn.

### Acknowledgments

<sup>†</sup>We thank M. S. Hopkins and C. L. Fincher for experimental assistance. Work supported by Aerospace Sponsored Research grant.

<sup>‡</sup>We gratefully acknowledge financial support from the ARO (DAAL-03-90-0113) and helpful discussions with H. P. Jenssen, D. J. Simkin, and A. Pinto.

We thank R. C. Morris for the forsterite sample.

### References

1. V. Petricevic, S. K. Gayen, R. R. Alfano, K. Yamagishi, H. Anzai, and Y. Yamaguchi, *Appl. Phys. Lett.* **52**, 1040 (1988).
2. V. Petricevic, S. K. Gayen, and R. R. Alfano, *Appl. Phys. Lett.* **53**, 2590 (1988).
3. H. R. Verdun, L. M. Thomas, D. M. Andrauskas, T. McCollum, and A. Pinto, *Appl. Phys. Lett.* **53**, 2593 (1988).
4. S. E. Stokowski, M. H. Randles, and R. C. Morris, *J. Quant. Elect.* **24**, 934 (1988).
5. M. H. Garrett, V. H. Chan, H. P. Jenssen, M. Whitmore, A. Sacra, and D. J. Singel, *OSA Proceedings on Advanced Solid-State Lasers 1991*, **10**, Hilton Head, NC, p. 76.
6. V. G. Baryshevski, M. V. Korzhik, M. G. Livshitz, A. A. Tarasov, A. E. Kimaev, I. I. Miskel, M. L. Meilman, B. J. Minkov, and A. P. Shkadarevich, (ref. 5), p. 26.
7. M. H. Whitmore and D. J. Singel (in preparation).
8. K. R. Hoffman, S. M. Jacobsen, J. Casas-Gonzalez, and W. M. Yen, (ref. 5), p. 44.
9. J. Casas-Gonzalez, K. R. Hoffman, S. M. Jacobsen, and W. M. Yen, *Extended Abstracts, The Electrochemical Society, Phoenix, AZ, 1991*, p. 954.
10. K. R. Hoffman, J. Casas-Gonzalez, S. M. Jacobsen, and W. M. Yen, *Phys. Rev. B* **44** (22), 12589 (1991).
11. H. Rager, *Phys. Chem. Min.* **1**, 371 (1977).
12. H. R. Verdun, L. M. Thomas, D. M. Andrauskas, and A. Pinto, *OSA Proceedings on Tunable Solid-State Lasers 1989*, **5**, Cape Cod, MA, p. 85.
13. These wavelengths were similar to those reported in ref. 8.

## **Chapter 4**

### **Optical Zeeman Spectroscopy of the Near IR Lasing Center in Chromium:Forsterite**

**Optical Zeeman Spectroscopy of the Near IR Lasing Center in  
Chromium:Forsterite**

T. S. Rose<sup>†\*</sup>, M. H. Whitmore<sup>‡</sup>, R. A. Fields<sup>†</sup>, and D. J. Singel<sup>‡</sup>

<sup>†</sup>*Electronics Technology Center, The Aerospace Corporation, M2/246,  
PO Box 92957, Los Angeles, CA 90009*

<sup>‡</sup>*Department of Chemistry, Harvard University,  
12 Oxford Street, Cambridge, MA 02138*

**Abstract**

Optical Zeeman spectra of the near IR luminescent center in Cr:forsterite were obtained with an external magnetic field applied along the crystallographic a and c axes. The field-dependent sublevel splittings of the triplet spin ground state were resolved via FLN (fluorescence line narrowing) techniques. The excellent correspondence between the observed splittings and those calculated for the tetrahedral Cr<sup>4+</sup> center, previously identified and characterized in forsterite by EPR (electron paramagnetic resonance), firmly establishes the identity of the near IR center as tetrahedral Cr<sup>4+</sup>. A simple model for the FLN excitation/emission cycle, including the influence of the external field on the optical line positions and intensities, is described.

## Introduction

Over the past decade, considerable effort has been devoted to the characterization of materials potentially useful as active media in broadly tunable solid-state lasers. In particular, the recent discovery of near IR (infrared) laser action, spanning the 1.17 – 1.37  $\mu\text{m}$  range, in Cr-doped forsterite<sup>1-3</sup> prompted a series of investigations aimed at elucidating the exact nature of the lasing center. Originally the active center was suggested to be  $\text{Cr}^{3+}$  substituting for  $\text{Mg}^{2+}$  at octahedral lattice sites<sup>1</sup>. Following the discovery that the near IR emission could be stimulated by excitation at 1.064  $\mu\text{m}$ ,<sup>2,3</sup> an alternative assignment was proposed: by analogy to the tetra-oxo  $\text{Cr}^{4+}$  center responsible for parasitic absorption in chromium activated Nd:YAG,<sup>4</sup> the lasing center in forsterite was assigned to  $\text{Cr}^{4+}$  lodged at tetrahedral silicate sites.<sup>2,3</sup> Polarized optical absorption spectra of Cr-doped forsterite were subsequently rationalized in terms of the energy level diagram for tetrahedral  $\text{Cr}^{4+}$  shown in Fig. 4.1.<sup>5,6</sup>

Conclusive evidence for the presence of tetrahedral  $\text{Cr}^{4+}$  centers in Cr-doped forsterite was obtained by EPR (electron paramagnetic resonance) spectroscopy.<sup>7-10</sup> The room temperature  $\text{Cr}^{4+}$ :forsterite EPR spectrum is amenable to analysis in terms of the conventional triplet spin Hamiltonian with parameter values of  $D = 63$ . GHz,  $E = 4.5885$  GHz,  $g_x = 1.99$ ,  $g_y = 2.00$ , and  $g_z = 2.003$ , and with the  $x$ ,  $y$ , and  $z$  principal axes oriented respectively along the  $a \pm b$ ,  $c$ , and  $\pm a - b$  crystallographic axes for the two sets of magnetically inequivalent centers.<sup>8</sup>

Although critical for the identification and characterization of the tetrahedral  $\text{Cr}^{4+}$  centers in forsterite, the EPR studies do not establish any correlation between the tetrahedral  $\text{Cr}^{4+}$  ion and the near IR lasing center. A primary method for establishing this correlation is provided by optical-Zeeman spectroscopy, in which the energy separation between the sub-levels of the  $^3A_2$  ground state of the  $\text{Cr}^{4+}$  centers, illustrated in Fig. 4.2, are measured via fluorescence emission. The behavior of the optically measured Zeeman splittings, with respect to the field strength and direction, can be directly compared with calculations based on the

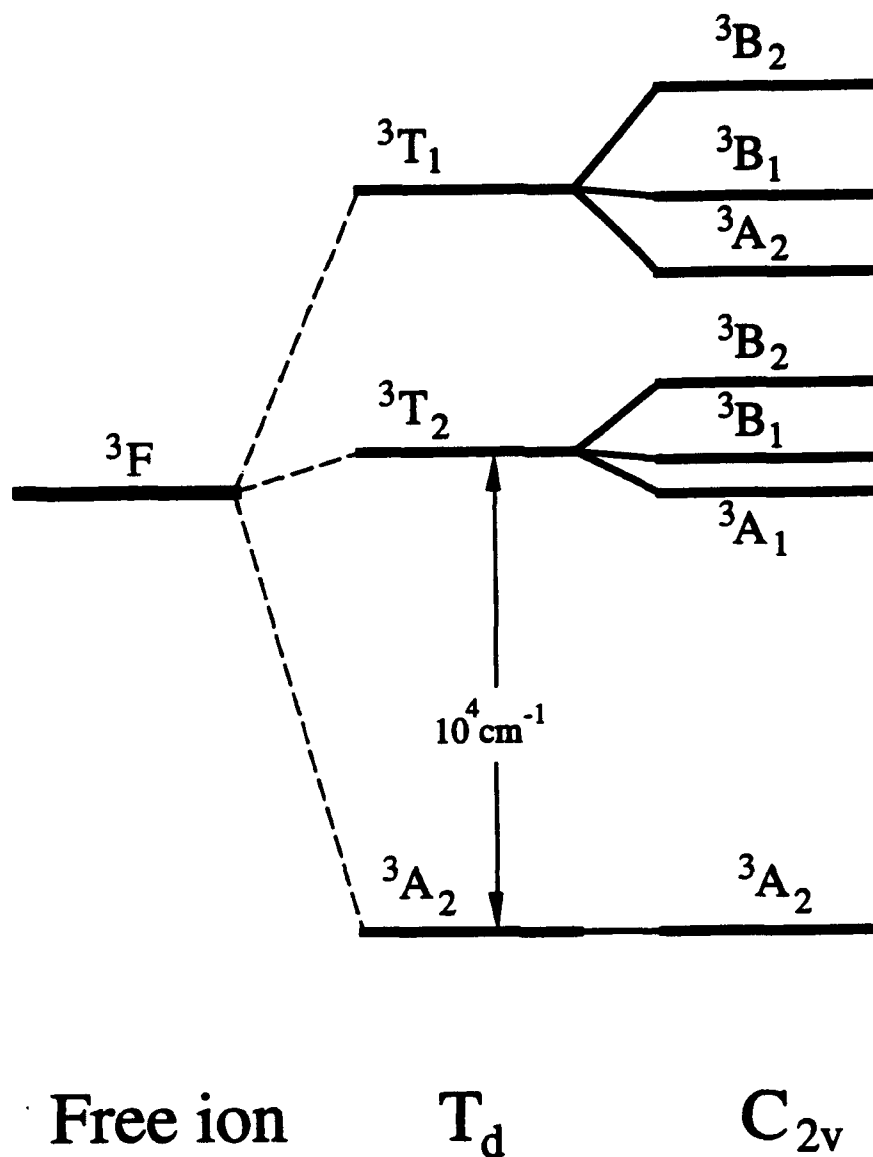
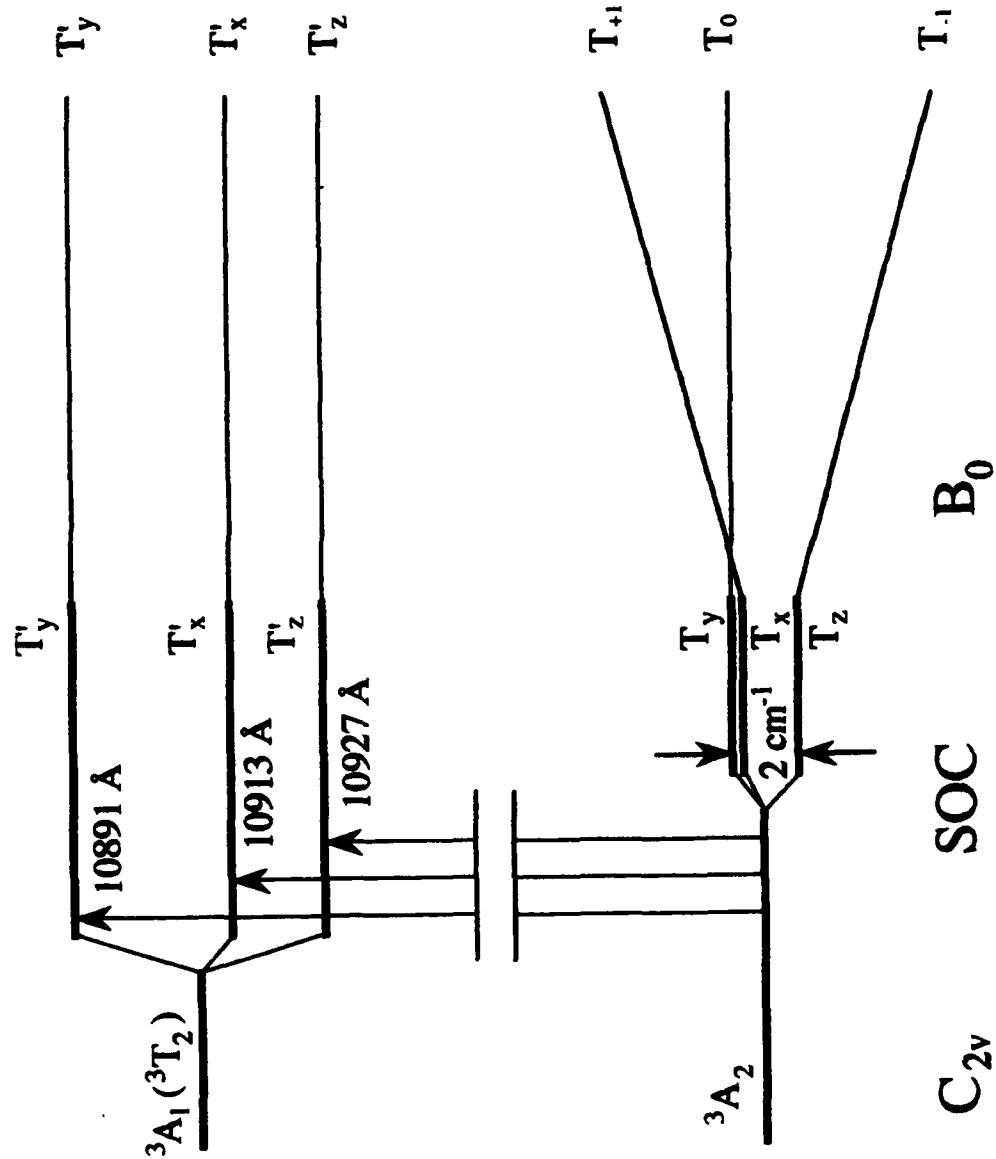


**Figure 4.1.** Typical energy level scheme of a  $d^2$  ion in a tetrahedral ligand field. Distortion of the coordinate sphere results in a reduction of symmetry from  $T_d$  to  $C_{2v}$ .

**Figure 4.2.** Detailed energy level diagram of the ground and first excited states for a  $d^2$  ion in a distorted tetrahedral ligand field, as illustrated in Fig. 4.1. The initially degenerate spin sublevels of  $^3A_2$  and  $^3A_1[{}^3T_2]$  are split by spin orbit coupling (SOC). Also depicted is the typical behavior for the spin sublevels in the presence of an external magnetic field applied along the y principal axis of the fine-structure tensor.





spin Hamiltonian parameters determined by EPR. In order to resolve the Zeeman splittings in the optical spectra, it is necessary to employ a narrow band excitation source to induce FLN (fluorescence line narrowing) of the emission lines.

Yen and coworkers first demonstrated the possibility of FLN in the forsterite system;<sup>11</sup> they resolved a  $2\text{ cm}^{-1}$  splitting in the near IR emission of Cr:forsterite in zero magnetic field. The Yen group later reported FLN assisted optical-Zeeman spectra obtained with the magnetic field aligned along one selected orientation (the b crystallographic axis).<sup>10,12</sup> Concurrently, we reported a preliminary account of a Zeeman-FLN spectroscopic investigation in which the field was aligned along the a and c crystallographic axes revealing the anisotropic behavior of the system and unequivocally proving  $\text{Cr}^{4+}$  to be the lasing center.<sup>13</sup> Here, we elaborate further on those results and discuss both the excitation/emission cycle involved in the observed Zeeman-FLN spectra and the factors influencing the line intensities.

## II. Experimental

The Cr:forsterite crystal, obtained from Allied-Signal Corp., was placed inside a liquid helium cryostat fitted with a super conducting 6 Tesla high homogeneity magnet and maintained at a temperature of  $\sim 2\text{ K}$  for the experiments. As displayed in Fig. 4.3, the crystal was oriented such that the optical excitation was polarized vertically along the crystal b axis (Pbnm crystal system<sup>14</sup>). The fluorescence was detected normal to the pump direction and parallel to the magnetic field. Rotation of the crystal about the b axis allowed for orientation of the magnetic field B along either the crystal c axis (i.e., the y principal axis of the zero-field splitting tensor<sup>7</sup>) or the crystal a axis. At both settings, all centers at the 4c sites are magnetically equivalent.

In order to obtain fluorescence line-narrowed spectra, optical excitation of the forsterite crystal was achieved with an argon-ion pumped Ti:sapphire laser (50–100 mW,  $0.01\text{--}0.02\text{ cm}^{-1}$  bandwidth) tuned into the three distinct spin sublevels ( $T_x$ ,  $T_y$ ,  $T_z$ ) of the lowest electronic excited state,  $^3A_1[^3T_2]$ .<sup>15</sup> Excitation at wavelengths 10891 Å, 10913 Å and

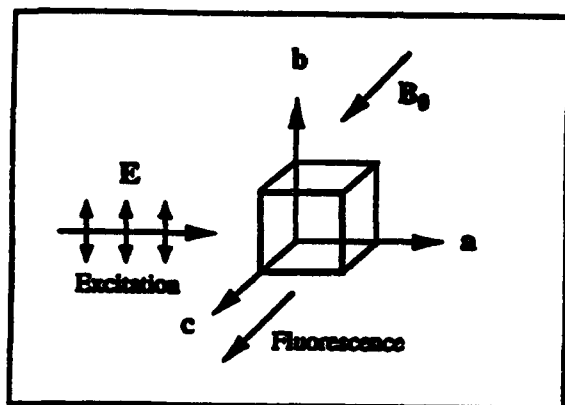


**Figure 4.3.** Orientation of the Cr:forsterite crystal and the optical and magnetic fields for the Zeeman experiments.

10927.5 Å, were noted to maximize the zero-field fluorescence at 10930 Å, the wavelength corresponding to the energy gap between the lowest sublevel,  $T_z'$ , of the excited  ${}^3A_1[{}^3T_2]$  and the nearly degenerate upper two sublevels,  $T_x$  and  $T_y$ , of the  ${}^3A_2$  ground state.<sup>6</sup> Broad band spectra were obtained via excitation with 5145 Å argon-ion light and with 7422 Å light derived from the Ti:sapphire laser. The fluorescence was focused into a 3/4 meter monochromator and detected with a photomultiplier tube and photon counting system. Suppression of scattered laser light detection was accomplished by generating 10 μsec pulses from the cw excitation beam with an AO modulator and measuring the fluorescence signal after a 1 μsec delay following each pulse. Spectra were recorded for magnetic field strengths ranging from 0 to 5 T.

### III. Results and Discussion

#### Line Narrowing Effects In the $Cr^{4+}$ Fluorescence

A comparison of the fluorescence spectra obtained in zero external magnetic field with excitation at 5145, 7422, and 10891 Å is shown in Fig. 4.4. Excitation at 5145 Å (Fig. 4.4, upper panel) results primarily in a broad emission spectrum peaked at ~8700 Å, characteristic of  $Cr^{3+}$  in octahedral coordination.<sup>5,17</sup> The origin of the near IR emission, attributed to  $Cr^{4+}$ , appears faintly at 10930 Å. This latter feature, with its accompanying phonon sideband, becomes much stronger relative to the  $Cr^{3+}$  emission when the excitation is tuned to 7422 Å (Fig. 4.4, middle panel), corresponding to absorption from the ground electronic state,  ${}^3A_2$ , to a state derived from the  ${}^3T_1$  multiplet of the tetrahedral  $Cr^{4+}$  chromophore.<sup>5,6</sup> No evidence of FLN is observed upon narrow band excitation at either 5145 or 7422 Å; the fluorescence linewidth at 10930 Å, ~10 Å, is very similar to that observed in the low temperature absorption spectra,<sup>11</sup> which exhibit three distinct lines at 10891, 10913 and 10927 Å assigned to transitions between the  ${}^3A_2$  ground state and the resolvable spin-triplet sublevels of the lowest electronic state  ${}^3A_1[{}^3T_2]$ . The absence of three corresponding lines in the fluorescence spectra, that is, the presence of emission only at 10930 Å, suggests that the luminescence occurs predominantly from a single  ${}^3A_1[{}^3T_2]$  spin sublevel.

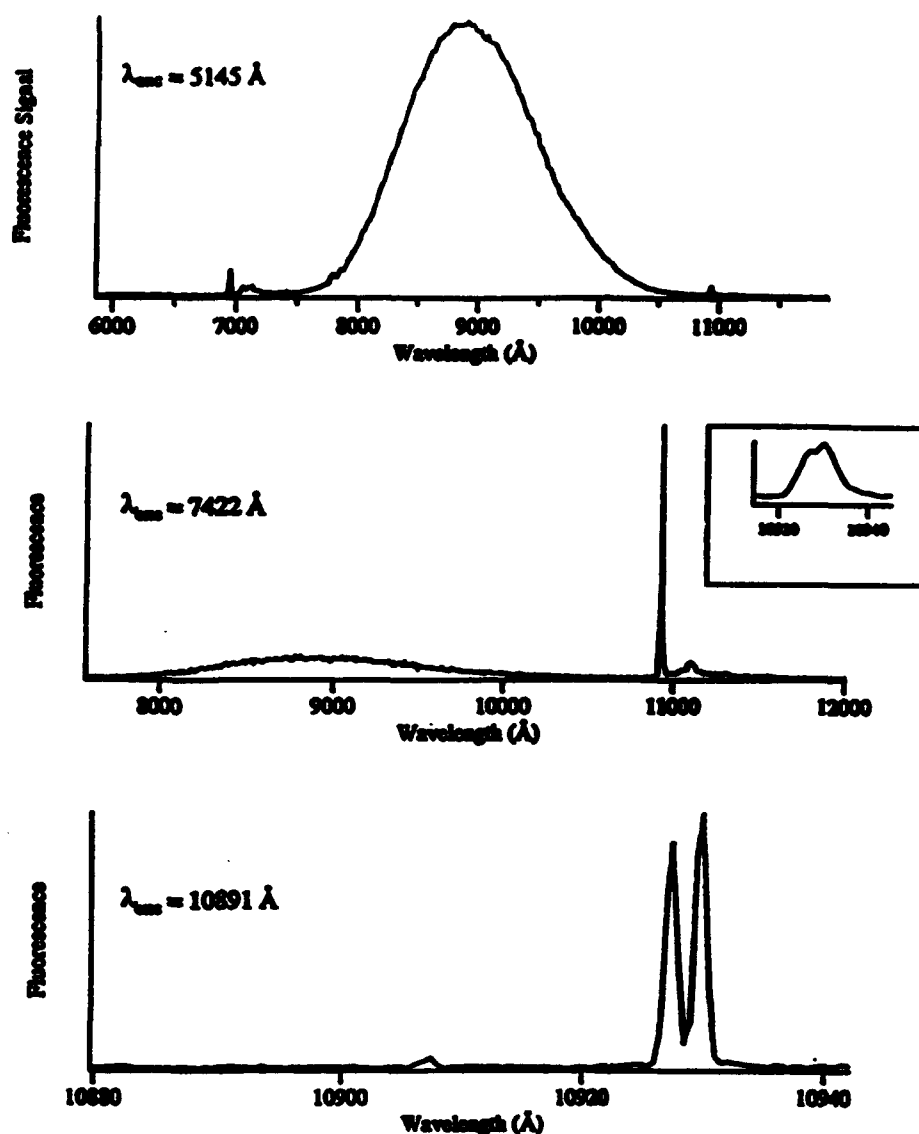


**Figure 4.4.** Comparison of fluorescence obtained from a Cr:Forsterite crystal at 2 K, using an argon ion laser (upper trace) and Ti:sapphire laser (lower two traces). The middle trace includes a higher resolution scan of the  $\text{Cr}^{4+}$  origin emission line which does not exhibit fluorescence line narrowing.

Substantial line-narrowing is evident in the fluorescence spectrum obtained with the excitation at 10981 Å ( $^3A_2 \rightarrow T_y' [^3A_1(^3T_2)]$ ), as illustrated in the bottom panel of Fig. 4.4. The spectrum exhibits a pair of dominant lines at 10927.5 and 10930 Å with linewidths of ~0.6 Å. The 2.5 Å separation of the lines is consistent with observations of Yen and coworkers.<sup>11</sup> Similar spectra are observed following excitation (at 10913 and 10927.5 Å) into the other two spin-triplet sublevels,  $T_x'$  and  $T_z'$ , of the  $^3A_1(^3T_2)$  state. These results indicate that internal conversion within the  $^3A_1(^3T_2)$  state occurs on a time scale much shorter than the fluorescence lifetime, so that the emission derives from the lowest spin sublevel,  $T_z'$ . It is interesting to note that this observation, in conjunction with the measurements reported by Baryshevski *et al.*<sup>9</sup>, suggests that the spin-lattice relaxation in the lowest excited triplet state ( $^3A_1(^3T_2)$ ) must be at least three orders of magnitude more rapid than in the ground triplet state ( $^3A_2$ ).

This view of the FLN excitation/emission cycle is reinforced by the presence of a weak feature at 10907 Å in the fluorescence spectra obtained with excitation at 10891 Å (Fig. 4.4, bottom panel). As a result of inhomogeneous broadening, the absorption lines from the ground state to each of the three spin sublevels of  $^3A_1(^3T_2)$  partially overlap. Excitation at 10891 Å thus not only predominantly pumps the upper sublevel,  $T_y'$ , but also pumps, to a limited extent, the high energy wing of the middle sublevel,  $T_x'$  (negligible pumping is expected for the high energy wing of the lower sublevel,  $T_z'$ , which is far off resonance). In effect, two distinct types of  $Cr^{4+}$  sites, line-center and wing, are excited. Upon internal conversion to the lowest excited spin sublevel,  $T_z'$ , the Stokes shift experienced by the wing sites differs from that experienced by the line-center sites by an amount equivalent to the energy difference between the two excited spin sublevels  $T_y'$  and  $T_x'$ . Thus, the wing site emission is blue-shifted from line-center emission by the energy difference between the upper and middle excited spin sublevels. The energy difference between the fluorescence feature at 10907 Å and those at 10929 Å, is equal to the energy difference of the absorption lines (and hence the two excited spin sublevels) that occur at 10891 and 10913 Å. The interpretation of the fluores-

cence is thus unambiguous: the observed emission derives only from the lowest excited state,  $T_2' \ ^3A_1[{}^3T_2]$ . In this regard, it is interesting to note that Yen and coworkers<sup>10,12</sup> opted to examine resonant FLN effects. This method leads to either very weak spectral intensities, when relaxation depopulated sublevels are monitored, or is complicated by scatter from the pump beam, when the emitting sublevel is monitored.

### **Zeeman Spectroscopy**

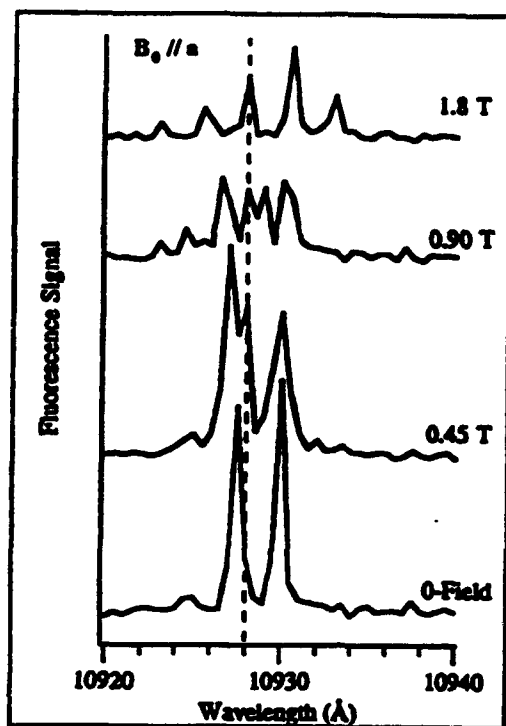
The splitting observed between the dominant peaks in the lower spectrum of Fig. 4.4 is consistent with the assignment of the emitting center as tetrahedral  $Cr^{4+}$ : on the basis of EPR measurements for the  ${}^3A_2$  ground state of tetrahedral  $Cr^{4+}$  in forsterite, the zero-field splitting is expected to be  $\sim 2\text{ cm}^{-1}$ , as illustrated in Fig. 4.2.<sup>7</sup> In order to prove this assignment, this correspondence must extend to all of the characteristic properties established by EPR, namely the two independent principal values of the fine-structure interaction tensor and the orientation of its principal axes.

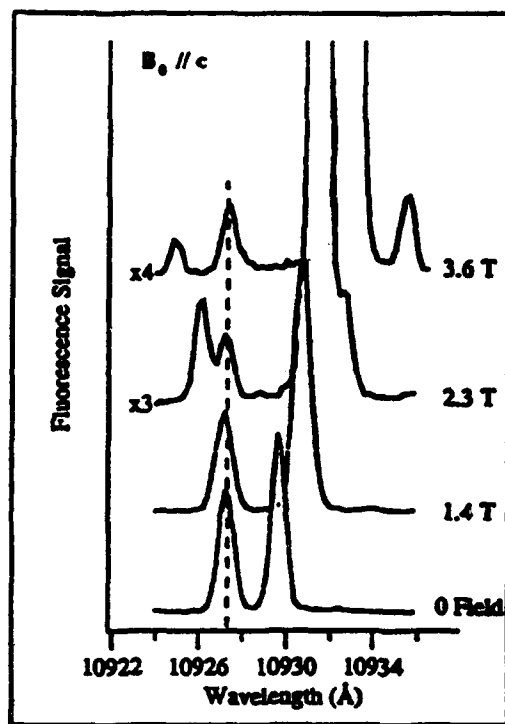
Exemplary optical Zeeman spectra, with resolution enhanced by FLN, are shown in Fig. 4.5. Spectra obtained following excitation into the  $T_y'$  spin sublevel of the  ${}^3A_1[{}^3T_2]$  excited state (10891 Å), with the field aligned along the crystallographic *a* and *c*, axes are displayed in Fig. 4.5a and 4.5b, respectively. For both field alignments, all four crystallographically equivalent  $Cr^{4+}$  ions observed by EPR are magnetically equivalent as well.<sup>8</sup> The *c* axis corresponds to a minor principal axis (*y*) of the zero-field splitting tensor, while the *a* axis is not a magnetic principal axis.<sup>7,8</sup>

Determination of the ground state sublevel structure would be trivial, if three fluorescence lines, each corresponding to the emission terminating at one of the sublevels, were observed in the spectra. In the presence of inhomogeneous broadening, however, the narrow band laser excites  $Cr^{4+}$  ions from each of the thermally populated ground state sublevels to one of the excited state sublevels.<sup>17</sup> Inasmuch as the resonant excitation selects distinct  $Cr^{4+}$  sites, three excited state populations are generated. These populations undergo

**Figure 4.5.** FLN spectra recorded at the indicated magnetic field strengths (in Tesla) applied along the crystallographic **a** and **c** axes. The laser wavelength was 10891 Å. The data for the **a**-axis was taken with lower resolution (0.5 Å steps) than the **c**-axis data (0.2 Å steps) and thus does not appear as smooth.







rapid internal conversion to the lowest spin sublevel of the excited state,  $T_z'$ , and then emit to all three ground state spin sublevels. As illustrated in Fig. 4.6, this scheme leads to a total of nine possible lines; the positions of these lines may be expressed as:

$$\nu_f = \nu_p - \nu_o - (\nu_i - \nu_f) \quad (4-1)$$

in which  $\nu_p$  refers to the pump laser frequency,  $\nu_o$  is the emission offset resulting from internal conversion, and the subscripts  $i$  and  $f$  designate the initial and final spin sublevels in the  $^3A_2$  ground electronic state involved in the FLN cycle. In our experiments,  $\nu_p$  was held constant for all values of the magnetic field. We assume in addition, that  $\nu_o$  is effectively independent of the field strength.<sup>18</sup> Accordingly, the field dependence of the FLN line positions is exclusively described by the parenthetical term in Eq. 4-1, and thus directly reveals the field dependence of the ground state spin sublevel splittings. Assignment of the emission lines to specific initial and final states is facilitated by the existence of three lines for which  $i=f$ . These lines are necessarily coincident and maintain a constant position in the spectrum at all field values; this easily identified spectral feature is highlighted by the dashed line in Fig. 4.5.

The coincidence of the three lines reduces the maximum number of distinct FLN lines from nine to seven. Because of the limits in spectral resolution and the weakness of certain transitions (discussed further in the following section) fewer lines were typically observed in the spectra. Despite the missing spectral features, a sufficient number of lines were present to permit the characterization of the field dependence of the sublevel splittings, and to determine their energies relative to a constant center-of-gravity at zero energy. In Fig. 4.7, the values derived from the FLN spectra are plotted as a function of the external magnetic field (applied along the  $a$  and  $c$  axes) and compared with sublevel energies determined by diagonalization of the triplet spin Hamiltonian with the parameter values determined by EPR.<sup>8,19</sup> Note that while a clear distinction in behavior exists for the magnetic field oriented along  $a$  or  $c$ , the agreement between the FLN and EPR data is excellent for both orientations. These results provide com-

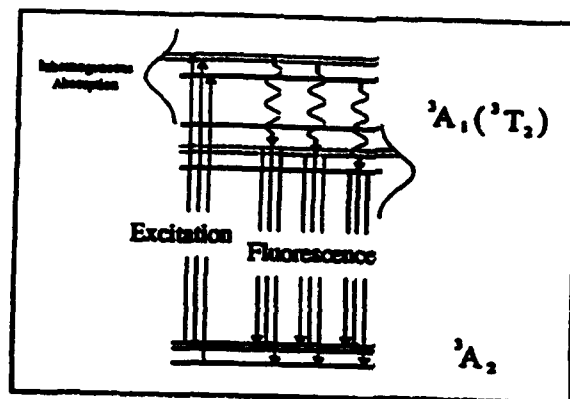


**Figure 4.6.** Illustration of nine possible fluorescence transitions in an inhomogeneously broadened  $\text{Cr}^{4+}$  system.

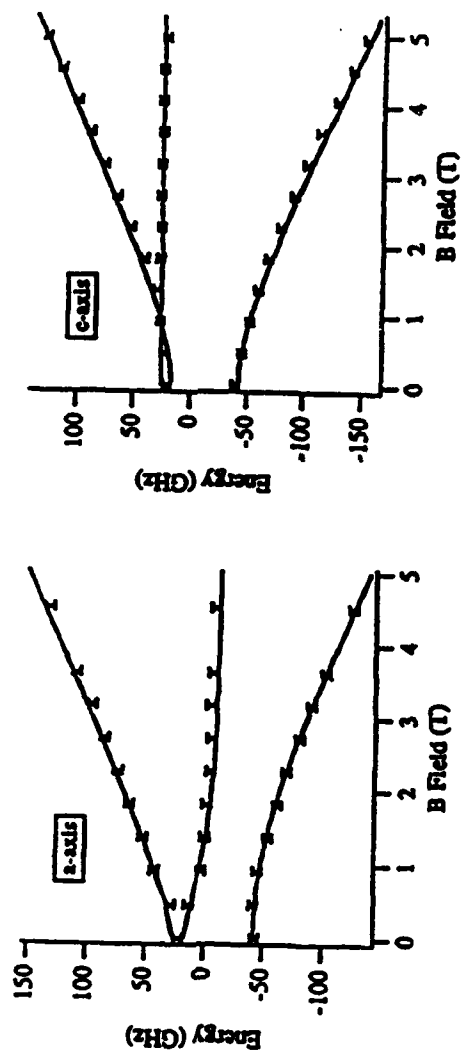


Figure 4.7. Comparison of energies derived from FLN spectra (points) with those predicted by EPR (solid curve)[8]. At field intensities where the energy levels were unresolved, a single point is drawn.

elling evidence that the EPR and optical center have the same identity, thereby identifying tetrahedral  $\text{Cr}^{4+}$  as the source of the near IR emission in Cr:forsterite.

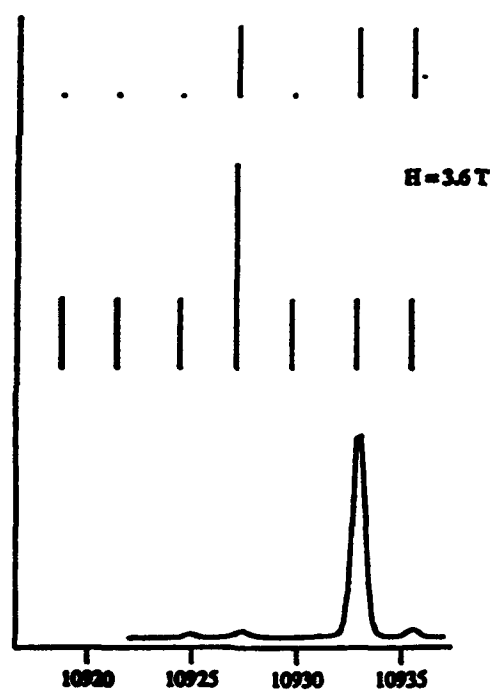
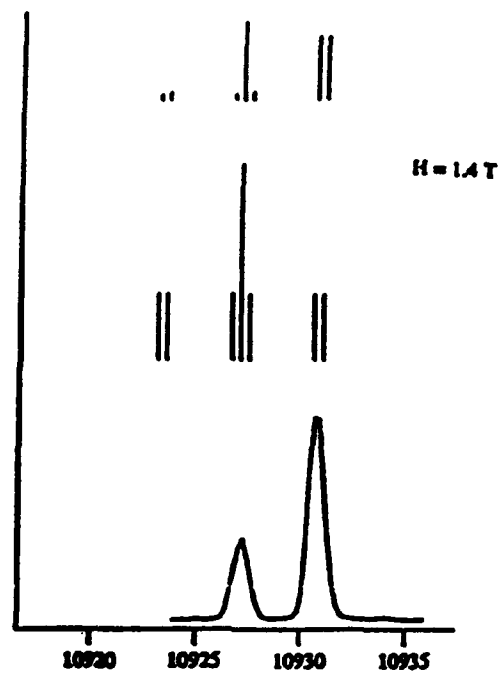
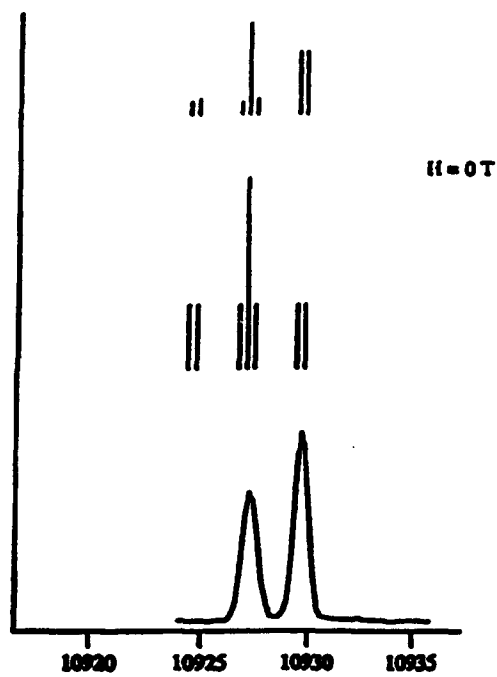
### FLN Intensities

The analysis of the line positions discussed above suffices to establish the correspondence between the near IR optical center in Cr-doped forsterite and the tetrahedral  $\text{Cr}^{4+}$  center identified by EPR. Nonetheless, it is of interest to analyze the line intensities in the FLN spectra in order to understand the factors responsible for the large variation in peak amplitudes and, in particular, explain the absence of several possible lines from the observed FLN spectrum.

In Fig. 4.8, we reproduce the FLN spectra obtained with  $B \parallel c$ , and with excitation tuned to 10891 Å. Assembled above the experimental data are two sets of stick spectra computed by associating with each field dependent line position (from Eq. 4-1) an intensity calculated in the following manner. In the lower spectra, all of the nine possible FLN transitions are given equal intensity; the central feature is composed of the three overlapping lines for which  $i=f$ . The discrepancy between these spectra and the experimental spectra is obvious. In the upper stick spectra, the line intensities are weighted with a Boltzmann factor,  $\exp(-\Delta E_i/kT)$ , in which  $\Delta E_i$  is the energy difference between the ground state sublevel from which the absorption originates and the lowest sublevel. This term greatly diminishes the intensity of all lines that do not originate in the lowest sublevel of the ground state (particularly at high field), thereby enhancing the correspondence with the experimental spectra. It is clear, however, that this factor does not fully reconcile the experimental and calculated spectra; evidently, the branching of the optical transition probabilities plays a critical role in determining the intensity distribution among the FLN lines.

Our model of the FLN cycle involves excitation from each of the ground state  $^3A_1$  sublevels,  $i$ , to a selected one of the  $^3A_1[{}^3T_2]$  sublevels,  $j$ , followed by emission from its lowest

**Figure 4.8.** Comparison of the experimental spectra obtained with  $B_0 \parallel c$  with stick spectra derived from the FLN model with (upper trace) and without (middle trace) Boltzmann factors. The dipole matrix elements have been set to unity in both calculations.





excited spin sublevel,  $T_2'$ , to the ground state sublevel  $j$ . Within this framework the intensity,  $I_{ij}$ , of the FLN line at energy  $\nu_{ij}$ , can be expressed as:

$$I_{ij} \propto e^{-\Delta E/kT} \left| \langle {}^3A_1j | \mu | {}^3A_2i \rangle \right|^2 \left| \langle {}^3A_2j | \mu | {}^3A_1T_2' \rangle \right|^2 \quad (4-2)$$

The first factor in Eq. 4-2 represents the Boltzmann population distribution among the ground state sublevels; the second and third factors denote the electric dipole transition probabilities associated with absorption and fluorescence, respectively. In writing Eq. 4-2, we have ignored any influence of the homogeneous and inhomogeneous linewidths on the absorption probabilities as well as any saturation effects. Following the spectral stability arguments of Van Vleck,<sup>20</sup> we assume that the field induced mixing of the orbital components of the states is negligible, and therefore, restrict our attention to the mixing of the (effective) triplet spin sublevels within the  ${}^3A_1[{}^3T_2]$  and  ${}^3A_2$  manifolds. Use of this approximation allows one to remove the dipole moment matrix element term, common to all transitions, and express  $I_{ij}$  in terms of spin overlap functions, so that

$$I_{ij} \propto e^{-\Delta E/kT} |K_j|^2 |K_i| |T_i|^2 \quad (4-3)$$

Under our experimental conditions only the triplet spin substates of the ground electronic state are appreciably mixed by the external field.<sup>18</sup> For convenience, we write the field-dependent, ground state spin substates  $\{|T_{-1}\rangle, |T_0\rangle, |T_{+1}\rangle\}$  as linear combinations of the zero-field triplet spin eigenstates  $\{|T_x\rangle, |T_y\rangle, |T_z\rangle\}$ . For the case  $B_0 \parallel c$ ,  $c$  being a principal axis ( $y$ ) of the fine structure interaction tensor, we may write:

$$|T_{-1}\rangle = \cos\theta |T_x\rangle + \sin\theta |T_z\rangle, \quad (4-4a)$$

$$|T_0\rangle = |T_y\rangle, \quad (4-4b)$$

$$|T_{+1}\rangle = \sin\theta |T_x\rangle - \cos\theta |T_z\rangle, \quad (4-4c)$$

in which  $\tan\theta = 1/2[(D-E) + \{(D-E)^2 + 4(g_y|\mu_B| |B_0|)^2\}^{1/2}] / g_y|\mu_B| |B_0|$  and the sublevel energies are  $(E_{\pm 1} = 1/2 [ -(D/3 + E) \pm \{(D-E)^2 + 4(g_y|\mu_B| |B_0|)^2\}^{1/2} ]$  and  $E_0 = D/3 + E$ .

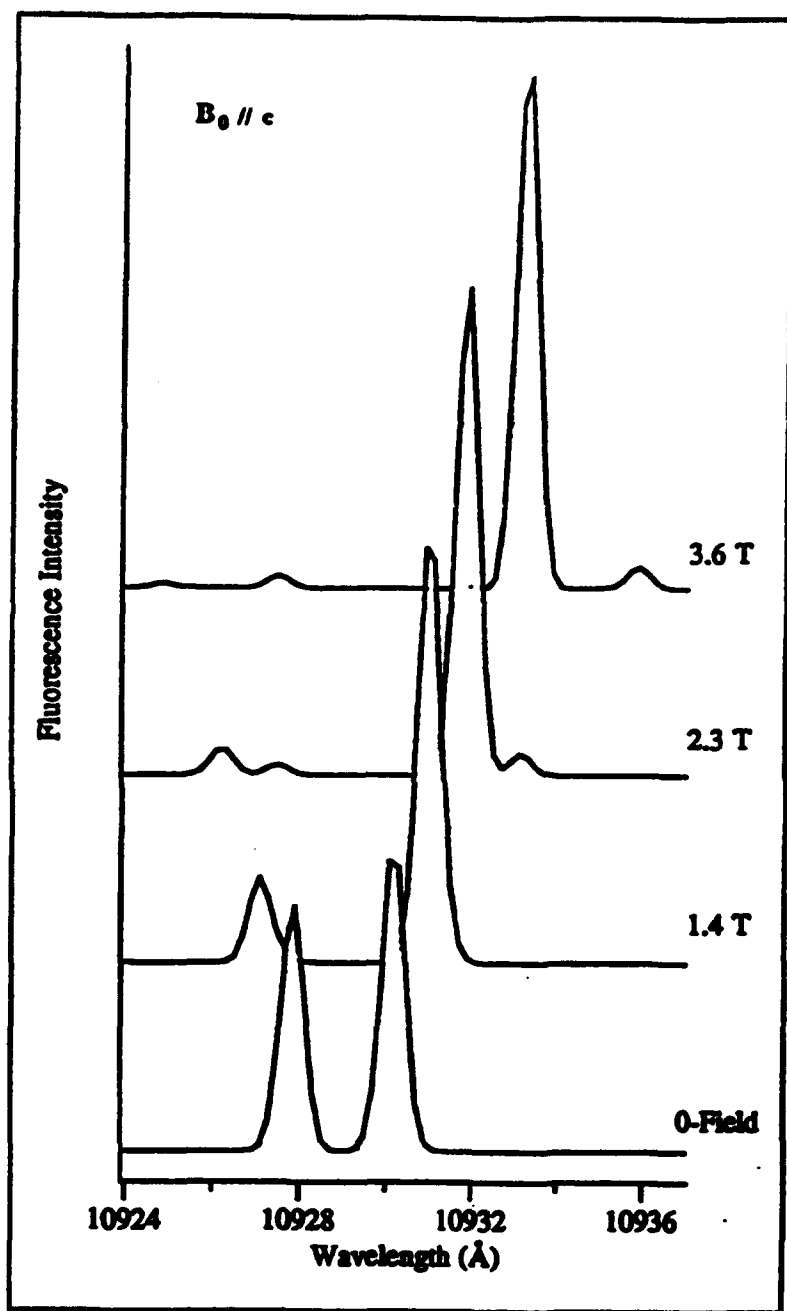
Introduction of such explicit forms for the field induced state mixing into Eq. 4-3 enables the  $J_{if}$  to be expressed entirely in terms of the applied magnetic field and the zero-field spin overlap functions. These overlap functions are taken as adjustable parameters which we evaluate through simulation and numerical analysis of the FLN spectra.

In Fig. 4.9 we present simulated FLN spectra directly comparable to the experimental spectra shown in Fig. 4.5b. These simulations are computed with the spin overlap terms listed in the matrix written below. In addition, the lines in the simulation are given a 0.6Å wide Gaussian lineshape, typical of the observed spectral profiles. The similarity of the experimental and simulated spectra, in comparison to the stick spectra in Fig. 4.8, lends support to the simple model that has been introduced.

	$T_z'$	$T_x'$	$T_y'$
$T_z$	4	$\sim 0$	$\sim 0$
$T_x$	1	$\sim 0$	1.8
$T_y$	w	1	1

In the overlap matrix we write "w" for  $\langle T_z | T_z' \rangle$  to indicate a weak but nonetheless detectable transition; the value  $\sim 0$  refers to situations in which there is no detectable transition. Because the total absorption resulting from exciting each of the three upper state sublevels was not explicitly measured, the relative magnitude of the matrix elements across the columns of the table are arbitrary; only the relative values within each column are meaningful. It is interesting to compare this matrix of zero-field triplet spin overlap integrals with the analogous matrix of effective transition strengths, obtained by Yen and co-workers<sup>11</sup> via analysis of the temperature dependence of absorption intensities. The two studies yield broadly similar results (Yen and coworkers report transition probabilities which should be compared with the squares of the overlap integrals that we have tabulated.) Some of the findings, however, are not entirely compatible. For example, we observe a weak, but detectable, absorption between  $T_z$  of  $^3A_2$  and  $T_z'$  of  $^3A_1[{}^3T_2]$ , while Yen and co-workers report the strength of this transition to be zero.<sup>11</sup> Additionally, we find no evidence of a connectivity between  $T_x$  of  $^3A_2$  and  $T_x'$  of  $^3A_1[{}^3T_2]$ .

**Figure 4.9.** Simulated FLN spectra at 2 K for  $B_0 \parallel c$  derived from the FLN model, induced spin overlap functions (see matrix in text) and an overall spectral response of 0.6 Å. A spectral step size of 0.2 Å, consistent with the experimental data, is employed.



Finally, notwithstanding the good agreement between data and the simulations illustrated in Fig. 4.9, we hasten to stipulate some limitations of our treatment, as we found that our analysis did not provide a set of parameter values that enabled equally satisfactory simulations over the entire range of the applied magnetic fields for all excitations. Factors that could degrade the quality of the agreement between the observed and simulated spectra include: 1) slight mixing of the excited state triplet sublevels; 2) detuning, which occurs when the absorption maxima are shifted from the pump wavelength by application of the magnetic field; and 3) reabsorption, which can reduce the intensity of lines terminating on the lowest ground state sublevel. This latter effect has been seen to distort the Zeeman spectra of ruby.<sup>22</sup>

#### IV. Conclusions

We have observed FLN at low temperature for the near IR emission from Cr-doped forsterite upon excitation into the lowest excited state derived from  $^3T_2$ . Excitation to higher energy levels, such as  $^3T_1$ , does not yield line-narrowed fluorescence, presumably because either the site energies are uncorrelated between  $^3T_1$  and  $^3T_2$  manifolds or energy transfer among the different sites in the inhomogeneous line occurs during the relaxation process. The FLN spectra result from emission from the lowest spin sublevel of  $^3A_1[{}^3T_2]$ , which can be populated either by direct excitation or by internal conversion following excitation to either of the two higher lying spin sublevels. The position of the lines in the FLN spectra were measured as a function of an applied magnetic field for two distinct directions in the crystal. Subsequent analysis of the line positions allowed for the determination of the ground state sublevel energies as a function of the field. This field dependence was compared to the behavior predicted for the tetrahedral  $Cr^{4+}$  paramagnetic center identified by EPR. The correspondence between the optical and EPR spectroscopic results unequivocally identifies the near IR lasing center as  $Cr^{4+}$ . A simple model of the FLN excitation/emission cycle incorporating mixing of the spin-state sublevels by the external field can be employed to describe the intensity distribution among the lines in the FLN spectra as a function of the field strength and direction.

### **Acknowledgments**

We gratefully acknowledge financial support from Aerospace Sponsored Research<sup>†</sup> and the Army Research Office<sup>‡</sup> (DAAL-03-90-0113), as well as helpful discussions with A. Pinto and W. Klemperer. We thank R.C. Morris for the forsterite sample.

## References

- [1] V. Petricevic, S.K. Gayen, R.R. Alfano, K. Yamagishi, H. Anzai, and Y. Yamaguchi, *Appl. Phys. Lett.* **52**, 1040 (1988).
- [2] V. Petricevic, S.K. Gayen, and R.R. Alfano, *Appl. Phys. Lett.* **53**, 2590 (1988).
- [3] H.R. Verdún, L.M. Thomas, D.M. Andrauskas, T. McCollum, and A. Pinto, *Appl. Phys. Lett.* **53**, 2593 (1988).
- [4] S.E. Stokowski, M.H. Randles, and R.C. Morris, *J. Quant. Elect.* **24**, 934 (1988).
- [5] W. Jia, H. Liu, S. Jaffe, W.M. Yen, and B. Denker, *Phys. Rev. B* **43**, 5234 (1991).
- [6] H.R. Verdún, L.M. Thomas, D.M. Andrauskas, and A. Pinto, in *OSA Proceedings on Tunable Solid-State Lasers*, edited by M.L. Shand and H.P. Jensen (Optical Society of America, Washington, DC, 1989), Vol. 5, p. 85.
- [7] M.H. Garrett, V.H. Chan, H.P. Jensen, M.H. Whitmore, A. Sacra, D.J. Singel, and D.J. Simkin, in *OSA Proceedings on Advanced Solid-State Lasers*, edited by G. Dubé and L. Chase (Optical Society of America, Washington, DC, 1991), Vol. 10, p. 76.
- [8] M.H. Whitmore, A. Sacra, and D.J. Singel, *J. Chem. Phys.*, in press.
- [9] V.G. Baryshevski, M.V. Korzhik, M.G. Livshitz, A.A. Tarasov, A.E. Kimaev, I.I. Mishel, M.L. Meilman, B.J. Minkov, and A.P. Shkandarevich, in *OSA Proceedings on Advanced Solid-State Lasers*, edited by G. Dubé and L. Chase (Optical Society of America, Hilton Head, NC, 1991), Vol. 10, p. 26.
- [10] K.R. Hoffman, J. Casas-Gonzalez, S.M. Jacobsen, and W.M. Yen, *Phys. Rev. B* **44**, 12589 (1991).
- [11] K.R. Hoffman, S.M. Jacobsen, J. Casas-Gonzalez, and W.M. Yen, in *OSA Proceedings on Advanced Solid-State Lasers*, edited by G. Dubé and L. Chase (Optical Society of America, Washington, DC, 1991), Vol. 10, p. 44.
- [12] J. Casas-Gonzalez, K.R. Hoffman, S.M. Jacobsen, and W.M. Yen, in *Extended Abstracts*, (The Electrochemical Society, Phoenix, AZ, 1991), p. 954.
- [13] T.S. Rose, R.A. Fields, M.H. Whitmore, and D.J. Singel, in *OSA Proceedings on Advanced Solid-State Lasers*, edited by L.L. Chase and A.A. Pinto (Optical Society of America, Washington, DC, 1992), Vol. 13, p. 17.
- [14] H. Rager, *Phys. Chem. Minerals* **1**, 371 (1977).
- [15] For clarity electronic states are addressed with  $C_{2v}$  labels following the scheme in Fig. 4.1; the triplet sublevels of the  $^3A_2$  and  $^3A_1[{}^3T_2]$  electronic states are denoted by the zero-field spin state labels  $T_i$  and  $T'_i$ , respectively, as indicated in Fig. 4.2.
- [16] R. Moncorge, G. Cormier, D.J. Simkin, and J.A. Capobianco, *J. Quant. Elect.* **27** (1), 114 (1991).
- [17] Strictly speaking, very limited excitation also occurs to the other two sublevels associated with wing transitions (vida supra). As we limit our detection to the immediate spectral region of the dominant emission lines, however, the spectra derive solely from the single predominantly excited sublevel.

- [18] The excited state spin sublevels are virtually unaffected at the field energies examined, as the Zeeman interaction remains considerably smaller than the zero field splitting of the  $^3A_1[{}^3T_2]$  at all surveyed field strengths. This approximation is implicitly incorporated in the energy level diagram of Fig. 4.2.
- [19] The given EPR parameters were determined at room temperature. The slight temperature dependence of the EPR parameters is neglected in crafting Fig. 4.7.
- [20] J.H. Van Vleck, *The Theory of Electric and Magnetic Susceptibilities*, Oxford University Press, London, 1965.
- [21] A. Carrington and A.D. McLachlan, *Introduction to Magnetic Resonance*, Harper and Row, New York, 1967.
- [22] F. Varsanyi, D.L. Wood, and A.L. Schawlow, *Phys. Rev. Lett.* 3 (12), 544 (1959).



## **Chapter 5**

### **Comparison of Chromium-Doped Forsterite and Akermanite Laser Host Crystals.**

# Comparison of Chromium-Doped Forsterite and Åkermanite Laser Host Crystals

M. H. Garrett, V. H. Chan, and H. P. Jenssen

*Department of Electrical Engineering and Computer Science and the Laboratory for Advanced Solid State Laser Materials, Massachusetts Institute of Technology, 77 Massachusetts Avenue, Room 13-3157, Cambridge, Massachusetts 02139*

M. H. Whitmore, A. Sacra, and D. J. Singel

*Department of Chemistry, Harvard University, 12 Oxford Street, Cambridge, Massachusetts 02138*

D. J. Simkin

*McGill University, 801 Shebrooke Street West, Montreal, Quebec H3A 2K6, Canada*

## Abstract

Electron paramagnetic resonance spectroscopy, and optical spectroscopy at room temperature and 10K have been used to analyze the role of chromium ions ( $\text{Cr}^{4+}$ ) in the near-infrared emission spectra of chromium-doped forsterite and Åkermanite crystals. Chromium ions ( $\text{Cr}^{4+}$ ) in nearly equivalent tetrahedral sites did not give rise to near-infrared emission from all samples.

## Introduction

Chromium-doped forsterite has received attention because it has an unusual lasing range between 1.1-1.3  $\mu\text{m}$  which does not exist for chromium ions in any other known crystal host environment. Its NIR (near-infrared) absorption and emission have been attributed to tetravalent chromium ions,  $\text{Cr}^{4+}$ , in the tetrahedrally coordinated silicon site [1]. Although there is some evidence supporting the above postulate, the presence in forsterite of two kinds of octahedral sites, (where charge compensated chromium ions of various valences (as well as other impurity ions) may be accommodated), complicates the EPR (electron paramagnetic resonance) and optical spectra making them difficult to interpret. To simplify the search for and analysis of  $\text{Cr}^{4+}$  ions in tetrahedral sites, we have grown and analyzed two chromium-doped crystals of the Åkermanite structure which have only tetrahedral sites to accommodate the  $\text{Cr}^{4+}$  ions.

In this paper we describe the crystal growth and characterization of Åkermanite crystals. We observe paramagnetic centers that are assignable to  $\text{Cr}^{4+}$  and have very similar properties in both chromium-doped forsterite and in one of the studied Åkermanite crystals. However, we measure optical absorption and emission spectra of these crystals that does not fully support the proposition that transitions from  $\text{Cr}^{4+}$  ions at

tetrahedral sites are the responsible for the NIR lasing of chromium-doped forsterite.

## Crystal Structure

The forsterite crystal,  $\text{Mg}_2\text{SiO}_4$ , has space group symmetry  $\text{Pbnm}$ . Shown in Fig. 1 is the unit cell with the atomic site locations in forsterite. There are two distinct octahedral sites, one with inversion symmetry  $C_i$  and the other with mirror symmetry  $C_s$ , that are occupied with divalent magnesium ions. The tetrahedrally coordinated 4c silicon site has mirror symmetry  $C_s$ . When Cr-doped,  $\text{Cr}^{3+}$  was found to substitute for magnesium [2], while the  $\text{Cr}^{4+}$  ions are believed to occupy the tetrahedral sites [1].

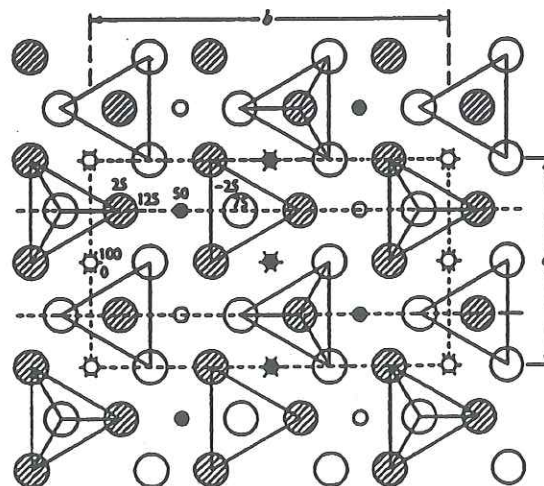


Figure 1. Unit cell of forsterite,  $\text{Mg}_2\text{SiO}_4$ . Small open and solid circles are Mg atoms, big circles are O atoms and Si atoms not shown are at the centres of the tetrahedra. (Reproduced with permission from Ref. [3].)



Shown in Fig. 2 is the structure of the  $\text{\AA}$ kermanites, generally  $\text{A}_2\text{BC}_2\text{O}_7$  [4]. We examine here BMAG ( $\text{Ba}_2\text{MgGe}_2\text{O}_7$ ) and CMSO ( $\text{Ca}_2\text{MgSi}_2\text{O}_7$ ) which have space group  $\text{P}\bar{4}2\text{m}$ . The  $\text{A}^{2+}$  ions at 4e sites have eightfold coordination and local symmetry  $\text{C}_8$  that can be substituted by rare-earth ions such as neodymium ( $\text{Nd}^{3+}$ ), (with charge compensating ions), to make a  $\text{Nd}^{3+}$  laser [5,6]. There are two tetrahedral sites,  $\text{B}^{2+}$  (T1) and  $\text{C}^{4+}$  (T2, T3). In the  $\text{\AA}$ kermanites examined here, the  $\text{B}^{2+}$  ions have magnesium ions ( $\text{Mg}^{2+}$ ) that are in an uncommon tetrahedral symmetry  $\text{S}_4$  instead of their usual octahedral symmetry. The two equivalent 4e tetrahedral sites, T2 and T3, have the same  $\text{C}_8$  symmetry as the Si site in forsterite and therefore could also be occupied by tetravalent chromium. In the  $\text{\AA}$ kermanites there are only tetrahedral  $\text{C}_8$  symmetry sites that could accommodate tetravalent chromium. This makes it an excellent host for studying the characteristics of  $\text{Cr}^{4+}$  in tetrahedral sites.

Shown in Fig. 3 are the nearly equivalent interatomic separations of the tetrahedral sites in forsterite and  $\text{\AA}$ kermanite crystals. It is apparent that a chromium ion located there would lead to nearly equivalent crystal-field strengths and thus transition energies.

### Crystal Growth

Undoped and Cr-doped BMAG and CMSO crystals were grown by the Czochralski technique from melts of nearly stoichiometric composition. An excess of germanium or silicon oxide was added to the respective melts to compensate for its loss by evaporation. The chromium concentrations in the melt were 0.01, 0.1, 0.25 and 0.5 mole percent with respect to Ge or Si. Feed materials were dehydrated prior to their weighing. Nucleation occurred at  $\sim 1400^\circ\text{C}$  and  $\sim 1450^\circ\text{C}$  for BMAG and CMSO respectively. Crystalline material for seeds

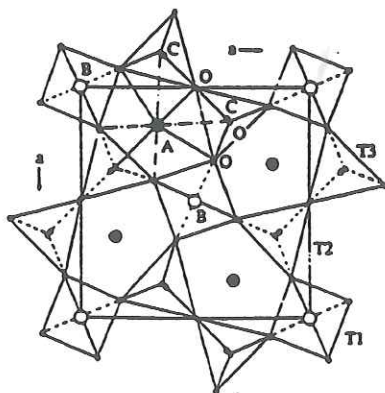


Figure 2. Unit cell of  $\text{\AA}$ kermanite, generally  $\text{A}_2\text{BC}_2\text{O}_7$  (Reproduced with permission from Ref. [4].)

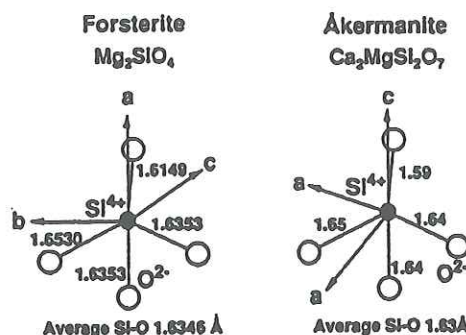


Figure 3. Local symmetry and interatomic spacings of forsterite and  $\text{\AA}$ kermanite tetrahedral sites.

was obtained by nucleation on a platinum wire. X-ray oriented seeds were cut along the (100) plane to avoid a cleavage plane along (001).

Faceted, optical quality crystals were grown in an air atmosphere environment to help oxidize  $\text{Cr}^{3+}$  to  $\text{Cr}^{4+}$ . The crystals were grown with a seed rotation rate of 30 rpm and a pull rate of 1-2 mm/hr. Chromium-doped BMAG is aqua-blue in color and CMSO is purple-blue and both crystals are dichroic. Spectroscopic samples were x-ray oriented and cut along a and c crystallographic directions. To facilitate crystal rotation for EPR experiments crystals were cut into right triangular prisms along the two a-axes and the c crystal axis. Cr-doped forsterite samples were obtained from Dr. R. Morris of Allied-Signal Corporation. These crystals were doped with a sufficient amount of chromium to distinctly color the crystals a light olive green. We also obtained a more lightly doped sample, with only faint coloration, from Professor S. Hafner from the University of Marburg.

### EPR Measurements and Analysis

In EPR experiments, we examined the 0.01 and 0.5 mole percent Cr-doped BMAG crystals. We also examined light and heavily doped forsterite samples and a 0.25 mole percent Cr-doped CMSO crystal. In the 0.5 mole percent Cr-doped BMAG crystal three strong EPR absorptions were identified:  $\text{Mn}^{2+}$  (from its characteristic nuclear hyperfine structure),  $\text{Fe}^{3+}$  (which exhibits an axial EPR spectrum very similar to  $\text{Fe}^{3+}$  in garnets), and a signal that we attribute to  $\text{Cr}^{4+}$ . In the less heavily-doped BMAG:Cr only the iron and manganese signals were detected.

The field-for-resonance of BMAG:Cr is plotted as a function of crystal orientation with respect to the external field in Fig.4(a) for the spectral feature attributed to  $\text{Cr}^{4+}$ . At a general orientation of the crystal, we observe four EPR signals that reflect four crystallographically equivalent sites (arbitrarily

designated  $\alpha$ ,  $\beta$ ,  $\gamma$ ,  $\delta$  in Fig. 5(a)). These sites become magnetically equivalent at certain crystal orientations in a manner that indicates the incorporation of this species at the crystallographic 4e site of the BMAG P42m system. Both barium and germanium lie at 4e sites. Inasmuch as substitution of  $\text{Cr}^{4+}$  for  $\text{Ba}^{2+}$  is unlikely, owing to the disparity of their ionic radii (0.44 Å vs 1.42 Å), these results indicate the incorporation of  $\text{Cr}^{4+}$  at the tetrahedral germanium sites.

We observed only one of the three EPR transitions between the three spin-levels of  $\text{Cr}^{4+}$ , indicating a large zero-field splitting. Moreover, the well-known selection rules associated with transitions between spin one (quasi) zero-field states cause the disappearance of two of the EPR lines ( $\alpha, \gamma$ ) in the [110] plane. Our ability to fully characterize the EPR parameters of the system is thus somewhat limited. The field-for-

resonance angular variation curves can nevertheless be analyzed according to the usual spin Hamiltonian for a spin one system:

$$H = -\mu_B |B_0| g \cdot S + D(S_z^2 - S^2/3) + E(S_x^2 - S_y^2),$$

in which  $g$  is taken, as a point of departure, as isotropic with the free-electron  $g$ -value, and  $D$  and  $E$  are the fine structure parameters, which we least-squares fit to the experimental data. This analysis leads to the fine-structure parameters values (standard deviations in parentheses):

$$|D| = 1.1 \times 10^2 (0.3 \times 10^2) \text{ GHz, and} \\ |E| = 4.1 (0.1) \text{ GHz.}$$

The large magnitude of  $D$  suggests that deviations of the principal values of  $g$  from the free-electron value must be taken into account in a more complete

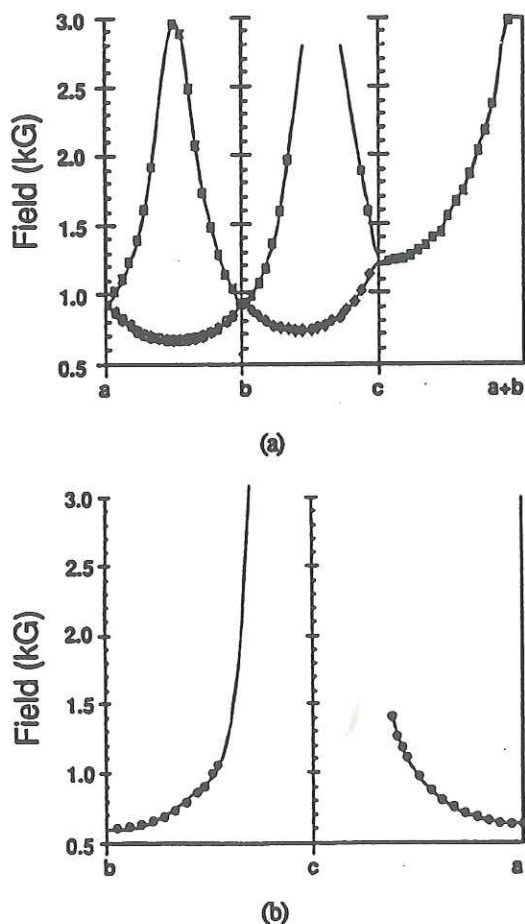


Figure 4. (a) Angular dependence of the  $\text{Cr}^{4+}$  EPR signals of Cr-doped BMAG. (b) Angular dependence of the  $\text{Cr}^{4+}$  EPR signals of Cr-doped forsterite. The crystallographic axes are indicated in the figures. The spectra were obtained at 9.51 GHz at a temperature of 298K.

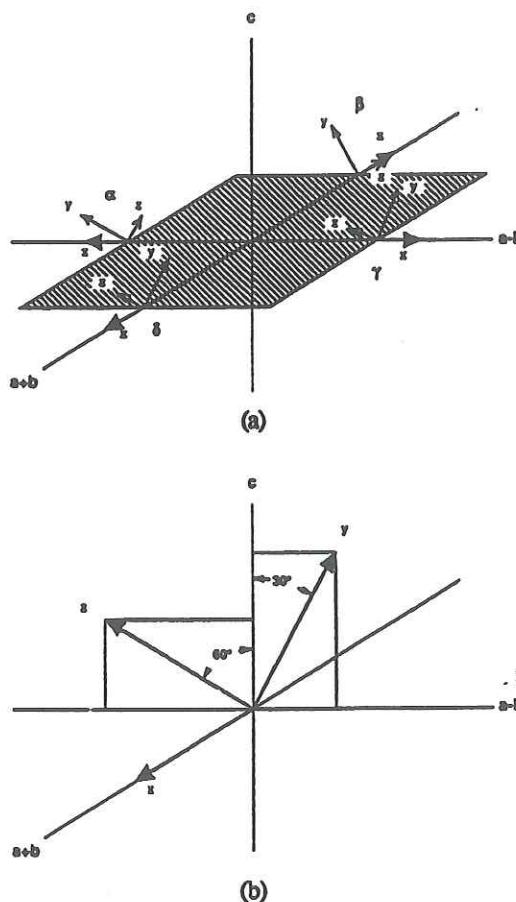


Figure 5. (a) Orientation of the  $\text{Cr}^{4+}$  centers at the 4e sites in BMAG. The relative orientations of the four centers related by the P42m space group symmetry. (b) A view of one of the sites, the  $\delta$ -site, detailing the orientations of the  $y$  and  $z$  fine-structure axes.



analysis, but that such deviations would not exceed ten percent, nor lead to significant revision of the estimated values of the fine-structure parameters. We also find that the dominant fine-structure axis (conventionally,  $z$ ) lies in the mirror plane and makes an angle of approximately  $\pi/3$  with the crystallographic  $c$  axis, while the minor ( $x$ ) axis lies normal to the mirror plane.

EPR spectra of Cr-doped forsterite reveal a paramagnetic center with EPR properties very similar to those of the  $\text{Cr}^{4+}$  center in BMAG. We observe a broad, structureless line, the intensity of which scales with the chromium-doping level. The signals are easily observed at room temperature. The pattern of magnetic equivalences exhibited by the crystallographically related signals manifests incorporation at a  $4c$  site and is thus consistent with  $\text{Cr}^{4+}$  substitution for silicon. Analysis of the angular variation of the field-for-resonance, shown in Fig. 4(b), in the manner described for BMAG leads to the fine-structure parameter values (values determined at room temperature):

$$|D| = 61. (1.) \text{ GHz and} \\ |E| = 4.588 (0.003) \text{ GHz.}$$

In forsterite, the dominant fine structure axis again lies in the mirror plane and makes an angle of approximately  $\pi/4$  with the crystallographic  $a$  axis, but the median axis ( $y$ ) lies normal to the mirror plane. An intriguing aspect of the  $\text{Cr}^{4+}$  center in forsterite, which we are continuing to study, is the decrease in the magnitude of the  $|E|$  with decreasing temperature. Because we observe the  $\text{Cr}^{4+}$  resonance near zero-field, and inasmuch as the size of the microwave quantum is very nearly equal to the zero-field splitting,  $|2E|$ , the effects of temperature on  $|E|$  can precipitate the disappearance of the  $\text{Cr}^{4+}$  EPR line (i.e., the shift of resonance position "beyond" zero-field); these effects are thus readily observed.

In preliminary studies of CMSO at 9.1 GHz, no signal of the type assigned to  $\text{Cr}^{4+}$  in BMAG and forsterite was observed. We suspect that in this system the value of  $|2E|$  exceeds the EPR frequency, and accordingly, the  $\text{Cr}^{4+}$  signal is difficult to observe.

### Optical Spectroscopy Measurements and Analysis

Polarized absorption spectra were obtained with a Perkin-Elmer Lambda 9 spectrophotometer. Room temperature and 10K spectra for Cr-doped forsterite, BMAG and CMSO are shown in Fig. 6. The 10K NIR absorption spectra are shown in the insets of Fig. 6. Zero-phonon lines are only present in forsterite and BMAG samples, at approximately the same wavelength region. The measured emissions of forsterite are about the same as published by other authors [7]. Zero-phonon lines were completely absent in the CMSO crystals. We were unable to find any emission from

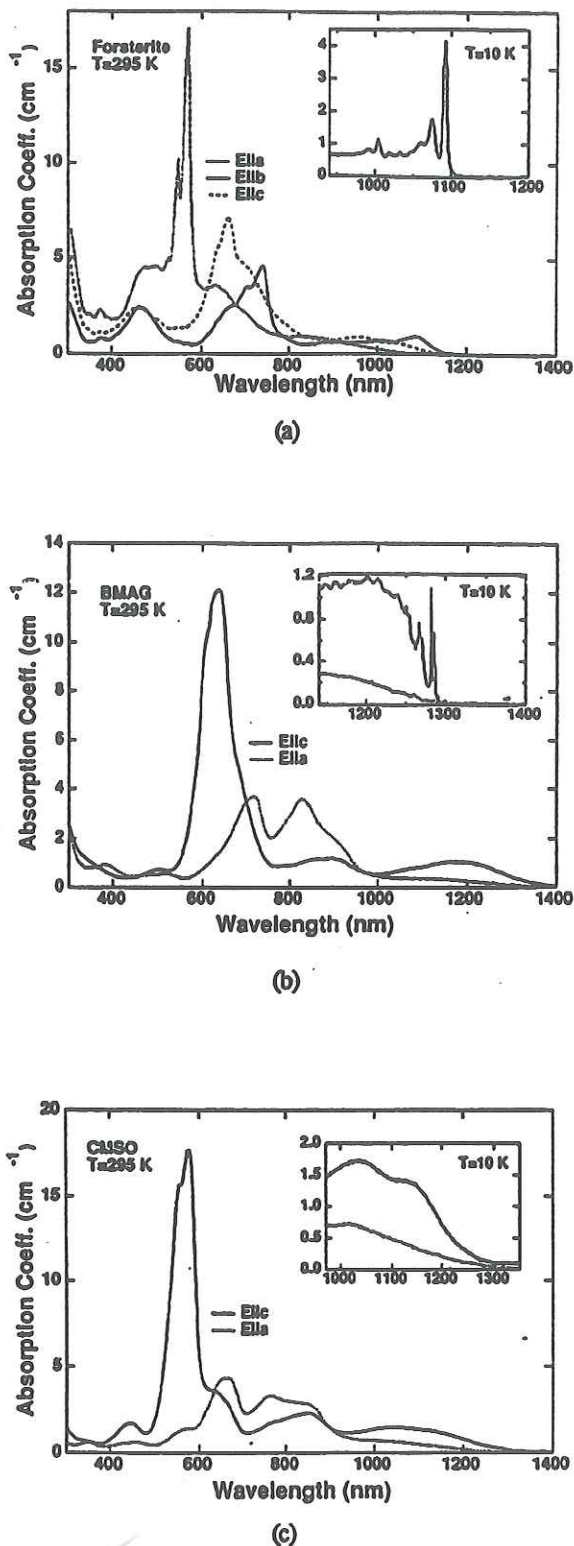


Figure 6. Room temperature and 10 K polarized absorption spectra of: (a)  $\text{Mg}_2\text{SiO}_4:\text{Cr}$ , (b)  $\text{Ba}_2\text{MgGe}_2\text{O}_7:\text{Cr}$  and (c)  $\text{Ca}_2\text{MgSi}_2\text{O}_7:\text{Cr}$ .



both Cr-doped åkermanites, even at liquid helium temperature.

To check the influence of a valency change in our åkermanite crystals on the spectra, we attempted to reduce the crystals in an oxygen partial pressure of  $10^{-17}$  atm at 750°C for 36 hours. The room temperature absorption remained the same and emission was still absent (indicating low oxygen diffusion). Lower oxygen partial pressures were obtained with forming gas (95% N<sub>2</sub> and 5% H<sub>2</sub>) and the samples were heated to 1000°C for 24 hours and then quenched. After reduction the absorption of CMSO:Cr is smaller by ~25% for E||c throughout the spectrum and still without emission (measured at room temperature).

In the absorption spectra of the three crystals we observed the same characteristic large absorption bands ascribed to the  $^3A_2 \rightarrow ^3T_1$  Cr<sup>4+</sup> in tetrahedral sites, (three absorption bands arise from the reduction of symmetry of T<sub>d</sub> to C<sub>s</sub>). Their peaks are given in Table 1.

Table 1. Absorption peaks of three Cr-doped crystals.

Crystals	Absorption Peaks (nm)
Mg <sub>2</sub> SiO <sub>4</sub> :Cr	571, 662, 742
Ca <sub>2</sub> MgSi <sub>2</sub> O <sub>7</sub> :Cr	579, 660, 767
Ba <sub>2</sub> MgGe <sub>2</sub> O <sub>7</sub> :Cr	636, 728, 832

The absorption peaks of BMAG are red-shifted relative to the other two crystals because of the smaller crystal-field strength at the Ge site. The absorption peaks of CMSO are almost identical to forsterite, as we would expect due to their similar average Si-O bond length of 1.63 Å and the same local C<sub>s</sub> symmetry (see Fig. 3) [8,9]. These absorption characteristics must come from having similar species in nearly identical local environments in these crystals. Comparing the crystal structure of forsterite and åkermanite, the only similarity is the Si (Ge) tetrahedral site with symmetry C<sub>s</sub>. Also, in these åkermanite crystals there are no chromium charge compensating species possible thus, Cr<sup>4+</sup> can only be substituted into the Si<sup>4+</sup> or Ge<sup>4+</sup> site. We deduce, (consistent with our EPR results), that Cr<sup>4+</sup> is in the tetrahedral site in all of the three crystals, Mg<sub>2</sub>SiO<sub>4</sub>:Cr, BMAG:Cr and CMSO:Cr.

However, considerable differences in the low temperature NIR absorption spectra exist (insets Fig. 6). First, although we observed zero-phonon lines both in the BMAG (1290 nm) and forsterite (1090 nm), they occurred in different polarizations since the c-axis of åkermanite corresponds to a-axis of forsterite when considering the orientation of the tetrahedra (see Fig. 3 note, forsterite's axis system is left-handed.). Second, zero-phonon lines (around 1.1-1.3 µm) are completely

absent in CMSO. Third, emission was not detected from any of the åkermanite crystals at room temperature or 10K. Based on the sensitivity of our spectrometer, the åkermanite emission intensity must be at least a factor of 100 less than that of forsterite. The radiative quantum efficiency must therefore be extremely low for Cr-doped åkermanites.

## Conclusions

From EPR measurements of the Cr-doped crystals and the similarity of their optical absorption spectra we believe that there indeed exists Cr<sup>4+</sup> in tetrahedral sites in all three crystals. However, because the zero-phonon lines and emission spectra differ for tetravalent chromium occupying tetrahedral sites in these three hosts we infer that it is unlikely that the mechanism responsible for the NIR lasing of Cr-doped forsterite is due solely to transitions of Cr<sup>4+</sup> ions in tetrahedral sites. It is interesting to note that the same conclusion was reached in Ref. [10] based solely on spectroscopy of forsterite.

## Acknowledgments

\*This work supported by ONR under agreement N00014-90-J-4073

‡This work supported by ARO under agreement DAAL03-90-0113

## References

1. V. Petricevic, S. K. Gayen and R. R. Alfano, "Laser Action in Chromium-Activated Forsterite for Near-infrared Excitation: Is Cr<sup>4+</sup> the lasing ion?," *Appl. Phys. Lett.* **53** (26), 2590 (1988). H. M. Verdun, L. M. Thomas, D. M. Andrauskas T. McCollum, and A. Pinto, "Chromium-Doped Forsterite Laser Pumped with 1.06 µm Radiation," *Appl. Phys. Lett.* **53** (26), 2593 (1988).
2. H. Rager, "Electron Spin Resonance of Trivalent Chromium in Forsterite Mg<sub>2</sub>SiO<sub>4</sub>," *Phys. and Chem. Minerals* **1**, 371, (1977).
3. W. A. Deer, R. A. Howie and J. Zussman, *Rock Forming Minerals* (Longmans, Green & Co. LTD, London, 1965), Vol. 1, pp 236-237.
4. S. F. Bartram, "Crystal Structure of Y<sub>2</sub>SiBe<sub>2</sub>O<sub>7</sub>," *Acta Cryst.* **B25**, 791 (1969).
5. T. H. Allik, M. J. Ferry, R. J. Reeves, R. C. Powell, W. W. Hovis, D. P. Caffey, R. A. Utano, L. Merkle and C. F. Campana, "Crystallography, Spectroscopic Analysis, and Lasing Properties of Nd<sup>3+</sup>:Ba<sub>2</sub>ZnGe<sub>2</sub>O<sub>7</sub>," *Opt. Soc. Am. B* **7** (7), 1190 (1990).
6. M. Alam, K. H. Goen, B. D. Bartolo, A. Linz, E. Sharp, L. Gillespie and G. Jannery, "Optical Spectra

and Laser Action of Neodymium in a Crystal  $\text{Ba}_2\text{MgGe}_2\text{O}_7$ ," J. Appl. Phys. **39**, 4728-4730 (1968).

7. R. Moncorgé, G. Cormier, D. S. Simkin and J. A. Capobianco, "Spectroscopic Properties and Fluorescence Dynamics in Chromium-Doped Forsterite," in Proceedings of the Topical Meeting on Solid State Lasers, Cape Cod, MA, OSA Proceeding **5**, 93 (1989).

8. J. V. Smith, "Reexamination of the Crystal Structure of Melilite", Amer. Min. **38**, 643 (1953).

9. H. R. Verdun, L. M. Thomas, D. M. Andrauskas and A. Pinto, "Laser Performance of Chromium-Aluminum-Doped Forsterite," in Proceedings of the Topical Meeting on Solid State Lasers, Cape Cod, MA, OSA Proceeding **5**, 985 (1989).

10. R. Moncorgé, G. Cormier, D. J. Simkin, and J. A. Capobianco, "Fluorescence Analysis of Chromium-Doped Forsterite ( $\text{Mg}_2\text{SiO}_4$ )," IEEE J. Quantum Electron., Vol. QE-27, 114 (1991).

## **Chapter 6**

### **Electron Paramagnetic Resonance Spectroscopy of Chromium-doped Gehlenites.**



Several chromium-doped gehlenite single crystals were examined by EPR. We were unable to identify any signals arising from tetrahedral  $\text{Cr}^{4+}$ .

Single crystals of the chromium-doped gehlenites  $\text{Ca}_2\text{Al}_2\text{SiO}_7$  and  $\text{Ca}_2\text{Ga}_2\text{SiO}_7$  were obtained from Dr. Bruce H. T. Chai of the University of Central Florida Center for Research in Electro-Optics and Lasers. Samples were doped with 0.5 to 1.0 weight percent chromium in the melt. Color ranged from light to deep blue with increasing chromium concentration.

Gehlenites are members of the melilite solid solution family and are thus isostructural with the melilite  $\text{\AA}$ kermanite. As is the case with BMaG, there are two possible tetrahedral cation substitution positions 2a and 4e. In gehlenite the 2a sites are occupied by  $\text{Al}^{2+}(\text{Ga}^{2+})$  ions and the 4e site occupancy is split between  $\text{Si}^{4+}$  and  $\text{Al}^{4+}(\text{Ga}^{4+})$ .<sup>1</sup> Rotation patterns for ions in the two sites are expected to be equivalent to those for BMaG.

Samples of both  $\text{Ca}_2\text{Al}_2\text{SiO}_7$  and  $\text{Ca}_2\text{Ga}_2\text{SiO}_7$  were examined with magnetic field rotation in the *ac* and *ab* planes; the experimental setup was same as that used for the study of BMaG. Typical EPR spectra for  $\text{Ca}_2\text{Al}_2\text{SiO}_7$  are shown in Figure 1 and for  $\text{Ca}_2\text{Ga}_2\text{SiO}_7$  in Figure 2. In both crystals only a single strong transition was observed. In  $\text{Ca}_2\text{Al}_2\text{SiO}_7$  the signal remained stationary at a resonance field of 3453 G for magnetic field rotation in all planes; the line width of this signal varied from 150 to 250 G with field rotation. In  $\text{Ca}_2\text{Ga}_2\text{SiO}_7$  the signal remained nearly stationary at a resonance field of approximately 1400 G for magnetic field rotation in all planes; the line width of this signal varied dramatically with field rotation, ranging from 20 G to 200 G. Several smaller signals were also observed in each crystal.

---

<sup>1</sup>P. Korczak, H. Schichl, and F. Raaz. *Fortschr. Mineral.*, 50 (1973) p. 211.

**FIG. 1.** Typical EPR rotational spectra of chromium-doped  $\text{Ca}_2\text{Al}_2\text{SiO}_7$  with  $B_0$  in the *ab* crystallographic plane.

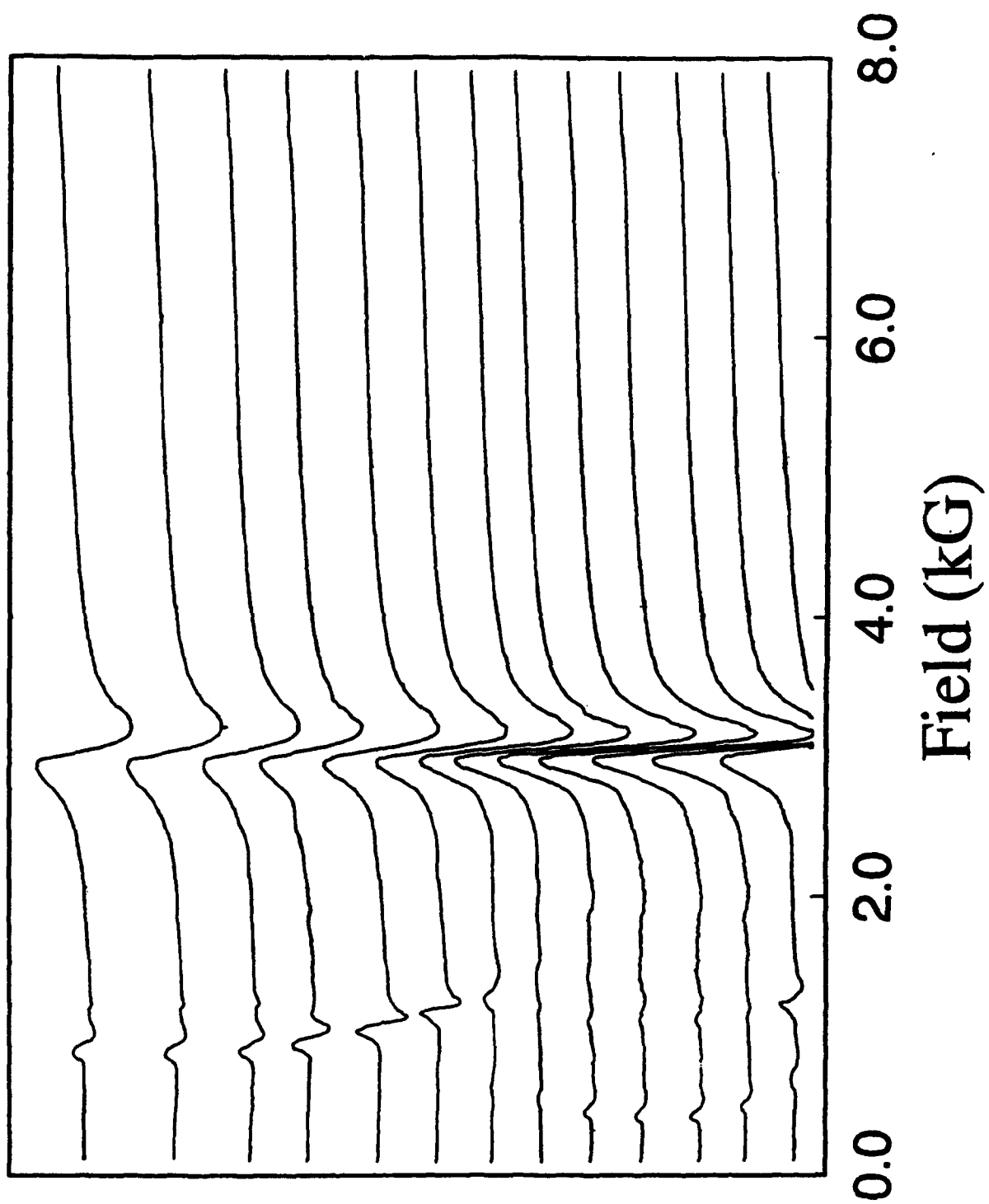
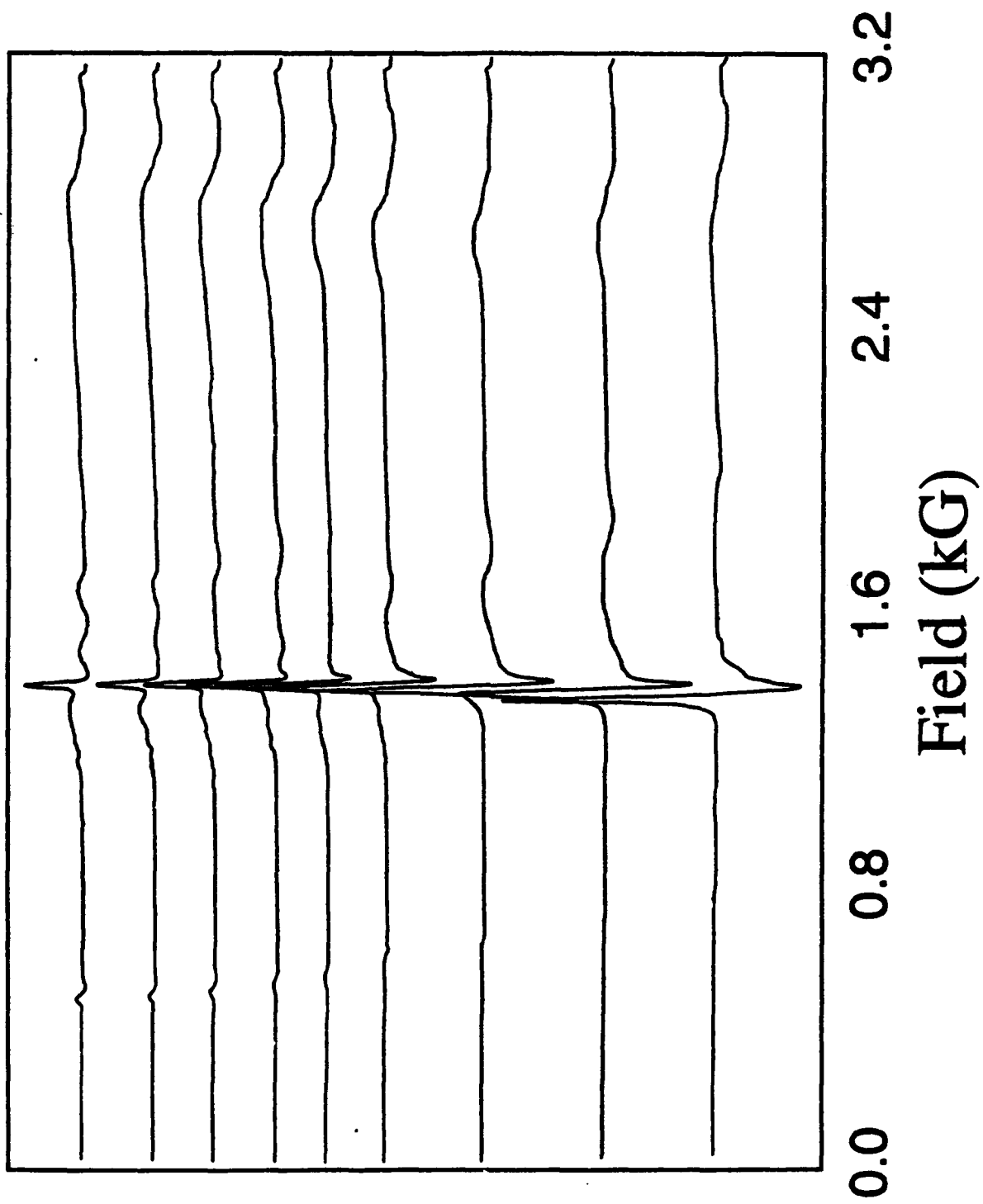


**FIG. 2.** Typical EPR rotational spectra of chromium-doped  $\text{Ca}_2\text{Ga}_2\text{SiO}_7$  with  $B_0$  in the ac crystallographic plane.



## Chapter 7

**Electron Paramagnetic Resonance Spectroscopy of Manganese-doped  
 $\text{Ba}_3(\text{VO}_4)_2$  : Identification of tetrahedral  $\text{Mn}^{5+}$  and  $\text{Mn}^{4+}$  centers.**

**Electron Paramagnetic Resonance Spectroscopy of Manganese-doped  
 $\text{Ba}_3(\text{VO}_4)_2$  : Identification of Tetrahedral  $\text{Mn}^{5+}$  and  $\text{Mn}^{4+}$  centers.**

Michael H. Whitmore<sup>#</sup>, Horacio R. Verdún<sup>†</sup>, and David J. Singel<sup>#\*</sup>

<sup>#</sup>*Department of Chemistry, Harvard University, 12 Oxford Street, Cambridge, Massachusetts 02138*

<sup>†</sup>*Fibertek, Inc., 510-A Herndon Parkway, Herndon, Virginia 22070*

**ABSTRACT**

EPR (electron paramagnetic resonance) spectra of single crystals of a new solid-state laser material, manganese-doped  $\text{Ba}_3(\text{VO}_4)_2$ , are reported. The spectra reveal incorporation of the putative active ion,  $\text{Mn}^{5+}$ , in place of the tetrahedrally coordinate  $\text{V}^{5+}$  ion at sites of  $\text{C}_{3v}$  symmetry. The spin Hamiltonian parameters that characterize the  $\text{Mn}^{5+}$  center are  $D=5.81$  GHz,  $g_{\parallel}=1.9608$ ,  $g_{\perp}=1.9722$ ,  $A_{\parallel}=70 \times 10^{-4} \text{ cm}^{-1}$ ,  $A_{\perp}=60 \times 10^{-4} \text{ cm}^{-1}$ . The substitution of  $\text{Mn}^{4+}$  for  $\text{V}^{5+}$ , at approximately one-fifth the abundance of  $\text{Mn}^{5+}$ , is also indicated. The  $\text{Mn}^{4+}$  spin Hamiltonian parameters are  $D=28$  GHz,  $g_{\parallel}=1.977$ ,  $g_{\perp}=1.985$ ,  $A_{\parallel}=80 \times 10^{-4} \text{ cm}^{-1}$ ,  $A_{\perp}=19 \times 10^{-4} \text{ cm}^{-1}$ .

## I. INTRODUCTION

Recently there has been considerable interest in the characterization new solid-state laser materials in which the active optical centers consist of  $3d^2$  ions incorporated at tetrahedral host lattices sites. Primary interest in such materials was sparked by the discovery of near IR (infrared) laser emission in chromium-doped forsterite ( $\text{Cr:Mg}_2\text{SiO}_4$ ).<sup>1-3</sup> The optical center in this material was assigned — by a combination of optical,<sup>4-11</sup> EPR (electron paramagnetic resonance),<sup>10,12-14</sup> and optical-Zeeman spectroscopies<sup>10,12,15,16</sup> — as  $\text{Cr}^{4+}$  substituting for  $\text{Si}^{4+}$  in the silicate tetrahedra. Near IR laser action has also been observed from tetrahedral  $\text{Cr}^{4+}$  in YAG<sup>17</sup> and  $\text{Y}_2\text{SiO}_5$ .<sup>18</sup> These studies have prompted interest in the broader examination of materials which incorporate other  $3d^2$  ions, such as  $\text{Mn}^{5+}$ , in tetrahedral coordination environments.

Pentavalent manganese in tetra-oxo coordination has been studied by optical and EPR spectroscopy in a number of manganese-doped arsenates, phosphates, and vanadates.<sup>19-27</sup> Capobianco *et al.*<sup>28</sup> have recently reported near IR emission from manganese-doped  $\text{Sr}_5(\text{PO}_4)_3\text{Cl}$  (apatite structure) and  $\text{Ca}_2\text{PO}_4\text{Cl}$  (spodiosite structure); Herren *et al.*<sup>29</sup> have reported similar results for manganese-doped  $\text{Ba}_5(\text{PO}_4)_3\text{Cl}$  and  $\text{Ca}_2\text{VO}_4\text{Cl}$ ; both groups have assigned the near IR emission to the  ${}^1\text{E}$  to  ${}^3\text{A}_2$  transition of  $\text{Mn}^{5+}$  ions located at tetrahedral sites. Very recently, Merkle *et al.* have reported a similar optical spectrum, and more significantly, laser action from manganese-doped  $\text{Ba}_3(\text{VO}_4)_2$ ; they have suggested that the lasing center is  $\text{Mn}^{5+}$ , substituting for  $\text{V}^{5+}$  at tetrahedral vanadate sites.<sup>30</sup>

In this paper we present EPR spectral studies of manganese-doped  $\text{Ba}_3(\text{VO}_4)_2$  that demonstrate the presence of  $\text{Mn}^{5+}$  ions substitutionally incorporated at tetrahedral lattice sites. In addition, these studies show that  $d^3$   $\text{Mn}^{4+}$  ions are also incorporated at tetrahedral sites in this material.



## II. CRYSTAL STRUCTURE OF $\text{Ba}_3(\text{VO}_4)_2$

The  $\text{Ba}_3(\text{VO}_4)_2$  crystal has trigonal symmetry and space group  $R\bar{3}2/m$ .<sup>31</sup> The structure is composed of discrete  $\text{VO}_4^{3-}$  tetrahedra linked by six- and ten-fold coordinate  $\text{Ba}^{2+}$  ions. Three  $\text{Ba}_3(\text{VO}_4)_2$  formula units constitute the hexagonal unit cell. Crystallographic data for  $\text{Ba}_3(\text{VO}_4)_2$  is given in Table 7.1, and the crystal lattice is shown in Figs. 7.1, 7.2, and 7.3.

The  $\text{V}^{5+}$  ions are situated at the hexagonal 6c position; the  $\text{Ba}^{2+}$  ions lie at two distinct positions, 3a (six-coordinate) and 6c (ten-coordinate).<sup>31</sup> Cationic substitution of manganese can thus occur only at the 3a or 6c positions. The former have site symmetry  $\bar{3}m$  and the latter have site symmetry  $3m$ , with the three-fold axes parallel to the crystallographic c axis. The three-fold symmetry of an ion situated at either of these positions ordains axial magnetic interaction matrices, with the unique axis (conventionally, z) coincident with c. Accordingly, all crystallographically equivalent sites, from both the 3a and 6c positions, must be magnetically equivalent for any orientation of the external magnetic field within the crystal. The EPR signal resonance-fields of ions located at these sites are invariant to rotation of the external field about c; field rotation perpendicular to c provides a complete specification of the relevant magnetic interactions. EPR measurements can thus clearly reveal the substitutional nature of guest cation incorporation in  $\text{Ba}_3(\text{VO}_4)_2$ . Unfortunately, inasmuch as all of the cation sites exhibit identical patterns of magnetic equivalences, EPR measurements cannot directly specify the occupied site, nor reveal the coordination number. For the presumptive guests — manganese ions in higher oxidation states — considerations of ionic charge as well as comparison of the ionic radii of  $\text{Ba}^{2+}$  (1.56 Å<sup>32</sup>) and  $\text{V}^{5+}$  (0.50 Å<sup>32</sup>) make the tetrahedral  $\text{V}^{5+}$  site the only plausible cation substitution site. This site is illustrated in Fig. 7.4

Ion	Site	Sym.	Coordinates			q
			x	y	z	
Ba <sub>1</sub>	3a	$\bar{3}m$	0	0	0	+2
Ba <sub>2</sub>	6c	3m	0	0	0.20525	+2
V	6c	3m	0	0	0.40798	+4
O <sub>1</sub>	6c	3m	0	0	0.3278	-2
O <sub>2</sub>	18h	m	0.1610	-0.1610	0.5654	-2

**TABLE 7.1.** Crystallographic data for Ba<sub>3</sub>(VO<sub>4</sub>)<sub>2</sub>. Orthorhombic  $R\bar{3}2/m$ .  $a=5.762$  Å,  $c=21.29$  Å. Coordinates are given for hexagonal system.<sup>31</sup>

**FIG 7.1.**  $\text{Ba}_3(\text{VO}_4)_2$  crystal lattice showing vanadate tetrahedra. View is parallel to the a-axis with the c-axis vertical.

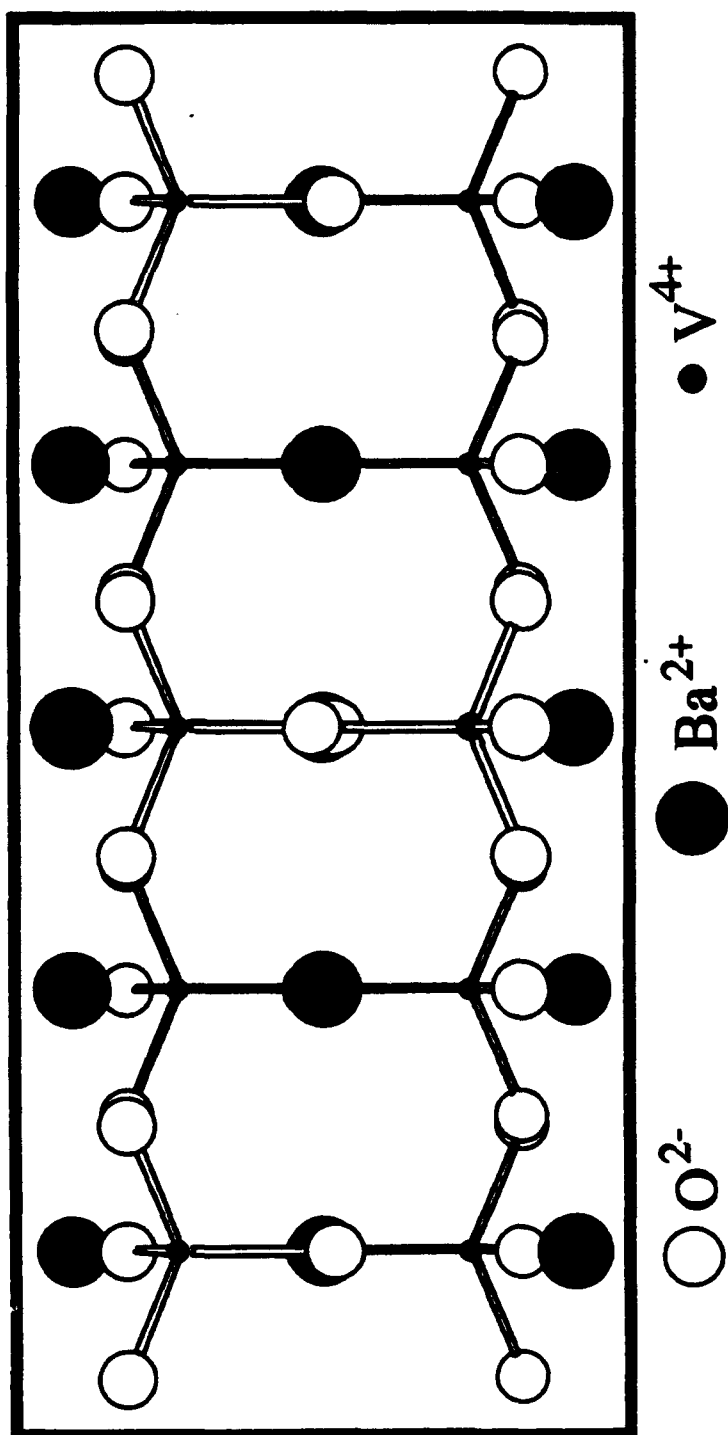
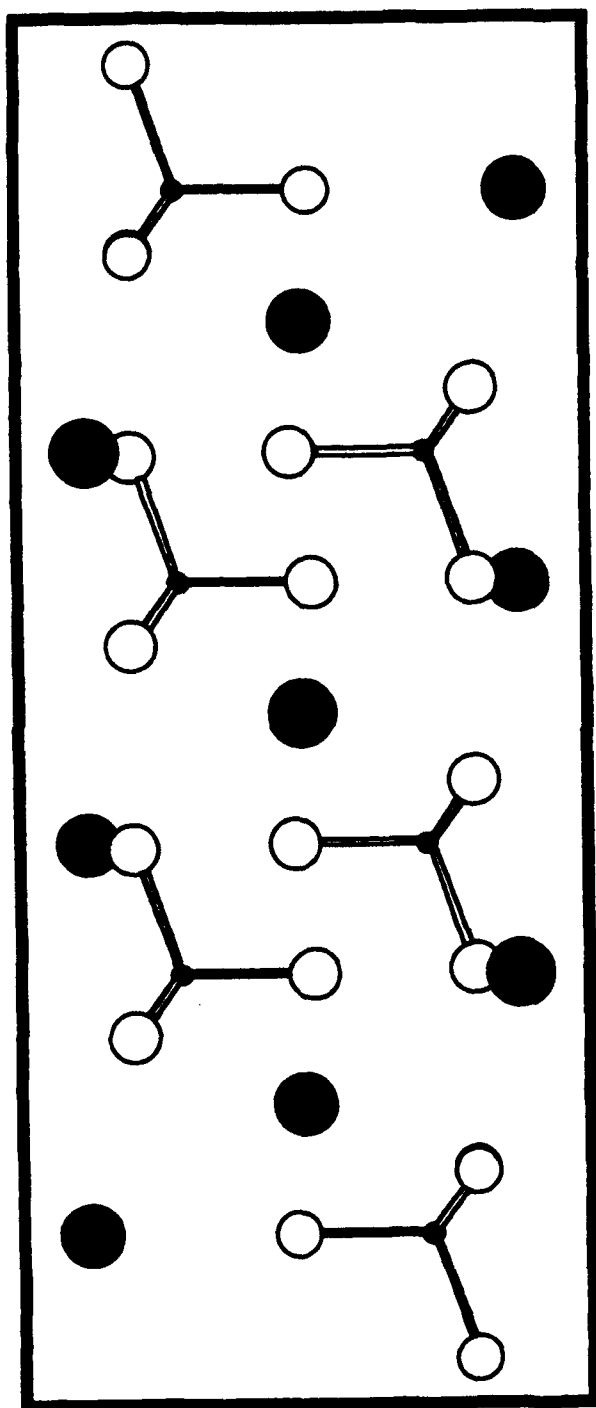


**FIG 7.2.**  $\text{Ba}_3(\text{VO}_4)_2$  crystal lattice showing vanadate tetrahedra. View is  $\pi/4$  to the a-axis with the c-axis vertical.



●  $V^{4+}$

●  $Ba^{2+}$

○  $O^{2-}$

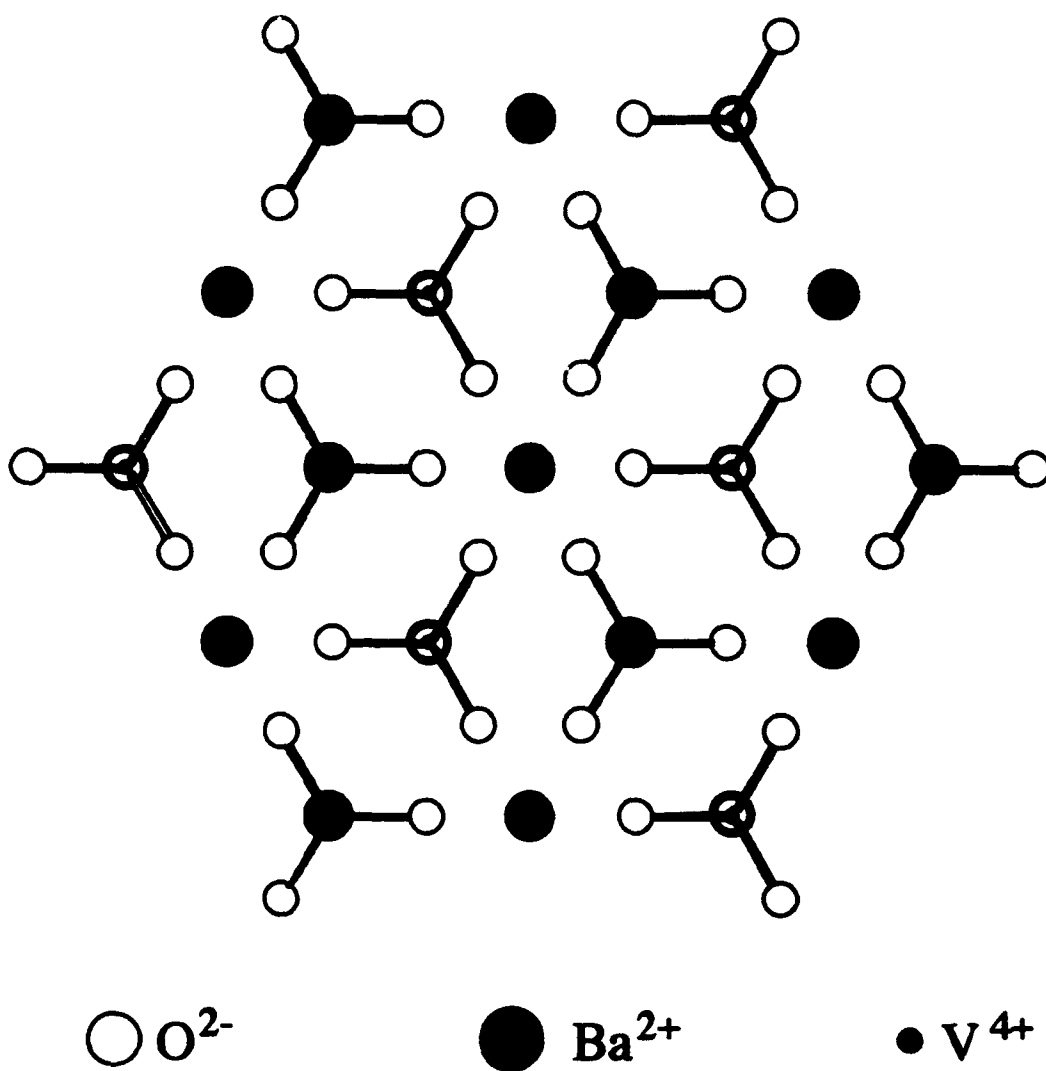


**FIG 7.3.**  $\text{Ba}_3(\text{VO}_4)_2$  crystal lattice showing hexagonal unit cell and vanadate tetrahedra. View is parallel to the trigonal axis,  $c$ .

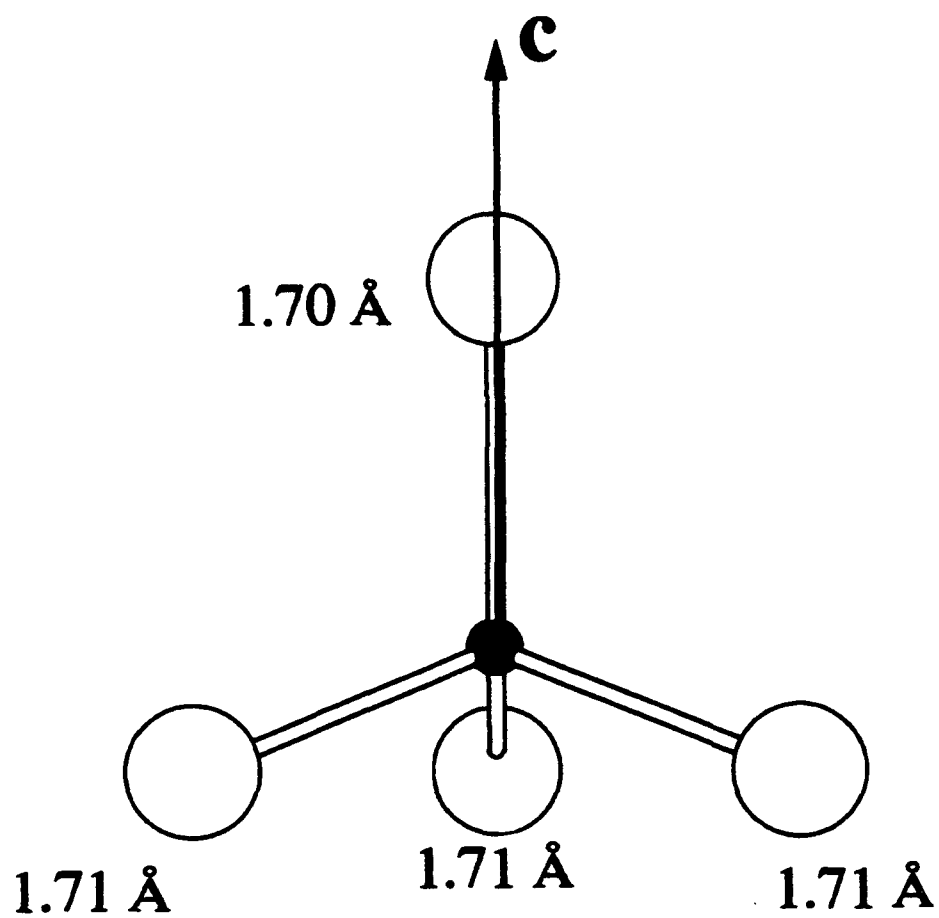


**FIG 7.4.** Vanadate tetrahedra in  $\text{Ba}_3(\text{VO}_4)_2$ . The view is perpendicular to the trigonal axis.



### III. APPARATUS AND EXPERIMENTAL PROCEDURES

#### A. Crystals

Single crystals of manganese-doped  $\text{Ba}_3(\text{VO}_4)_2$  were grown by the laser heat pedestal growth method under an oxidizing atmosphere designed to promote manganese inclusion as  $\text{Mn}^{5+}$ . The crystals were examined optically and shown to manifest absorptions associated with the putative  $\text{Mn}^{5+}$  center.<sup>30</sup> Samples were aquamarine in color and contained 0.25 weight percent manganese in the melt. The crystals were roughly cylindrical fibers of approximately 1 mm in diameter with  $c$  lying perpendicular to the cylinder axis. Sample volumes were approximately  $0.004 \text{ cm}^3$ .

#### B. EPR Spectroscopy

EPR experiments were performed with a Varian E-109 X-band spectrometer using 100kHz modulation and a Varian E-231  $\text{TE}_{102}$  rectangular cavity. The field was varied over a range of 0.05 to 9.5 kG and measured with a Walker Scientific MG-3D gaussmeter that was calibrated with a Micro-Now Instruments Model 515B-1 proton gaussmeter. Observations were obtained at a frequency of 9.09 GHz. All experiments were carried out with samples at ambient temperature.

The sample crystals were mounted by use of Apiezon N grease on rexolite sample rods. The normal to the desired crystal rotation plane was aligned by eye along the rod rotation axis; the alignment error in mounting was not more than approximately  $30 \text{ m}\pi$ . The rods were then mounted in a Varian goniometer and rotated in the cavity about an axis parallel to the microwave field,  $B_1$ , and perpendicular to the magnetic field,  $B_0$ . The uncertainty in the angular orientation of the sample due to the rotator gear was approximately  $2 \text{ m}\pi$ .

#### IV. EXPERIMENTS and RESULTS

Measurements were made on  $\text{Ba}_3(\text{VO}_4)_2$  with magnetic field rotation in the  $aa$  and  $ac$  crystallographic planes. As indicated in Sec. II, crystallographic symmetry requires that the principal axes of the fine structure and electron Zeeman interaction lie within these planes for any cation incorporated substitutionally in the  $\text{Ba}_3(\text{VO}_4)_2$  crystal. The EPR spectrum observed with  $B_0$  along  $c$  is illustrated in Fig. 7.5. Four strong, multiplet signals are evident. They can be identified as arising from manganese ions because of the characteristic sextet hyperfine structure.<sup>33</sup> In addition a number of weak signals, which were not further analyzed, appear in the spectrum.

The variation in field-for-resonance of the strong manganese EPR signals as a function of orientation of  $B_0$  within the  $ac$  crystallographic plane is illustrated in Fig. 7.6; the plotted points designate the center field value of each hyperfine multiplet. For magnetic field rotation in the  $aa$  plane, the fields-for-resonance remain stationary at values equivalent to those observed for  $B_0$  along  $a$  in the  $ac$  plane. The rotational patterns obtained for the two planes clearly exhibit the properties anticipated for cation substitution.

A readily recognizable relation between three of the four strong signals — those marked with circles in Fig. 7.6 — is apparent upon closer examination of the figure. The two higher field signals are roughly symmetrically disposed about a mean field value that is approximately twice that of the nearly stationary, lower field signal. This relation is characteristic of an  $S=1$  system with a fine structure interaction smaller than its Zeeman interaction. The EPR signals of the  $S=1$  system also jointly display large intensity variations with magnetic field orientation (in the  $ac$  plane) and nearly constant hyperfine splittings. In contradistinction, the fourth strong signal — marked with squares in Fig. 7.6 — shows little intensity variation with orientation of the magnetic field, but a large anisotropy in its hyperfine splittings (87 G with  $B_0$  along  $c$  and 20 G with  $B_0$  perpendicular to  $c$ ). The maximum intensity of this signal is approximately one-fifth of the other three. Evidently, this signal

**FIG 7.5.** Exemplary EPR spectra of manganese-doped:  $\text{Ba}_3(\text{VO}_4)_2$  with  $B_0$  near  $c$  in the  $ac$  crystallographic plane. The EPR multiplet lines assigned to  $\text{Mn}^{5+}$  and  $\text{Mn}^{4+}$  ions are indicated.

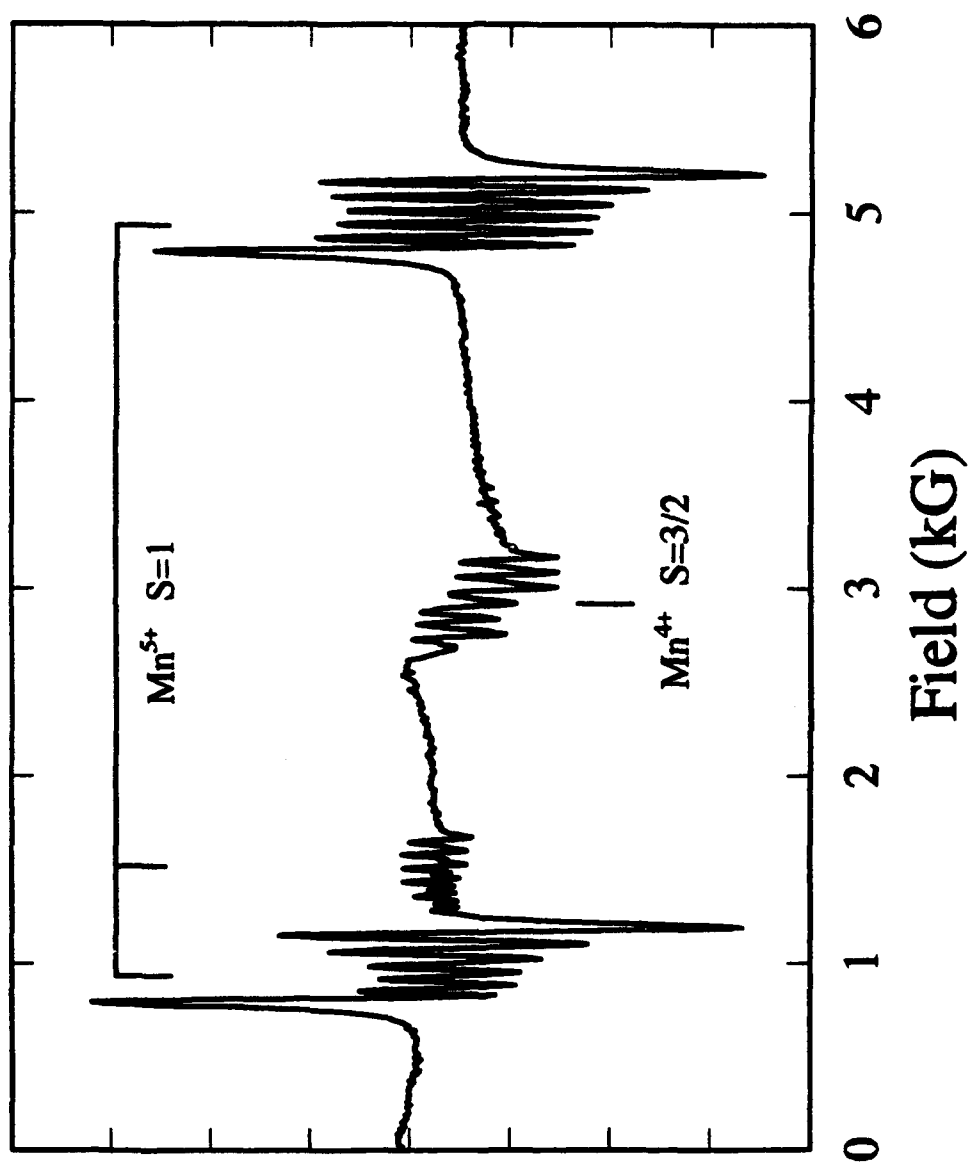
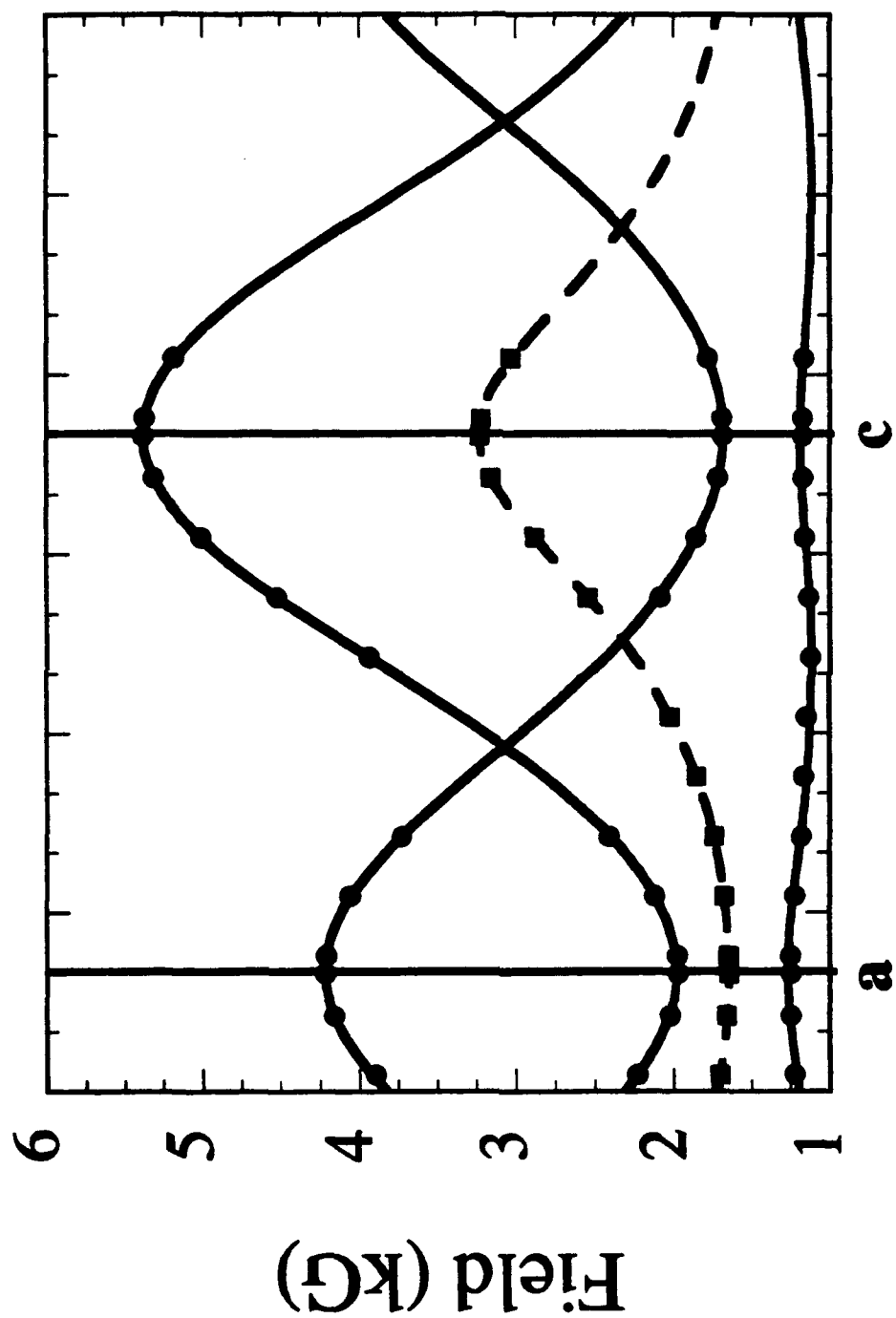


**FIG 7.6.** Field-for-resonance *versus* orientation of  $B_0$  in the *ac* crystallographic plane for  $Mn^{5+}$  (circles) and  $Mn^{4+}$  (squares) in  $Ba_3(VO_4)_2$ . The points correspond to the center field of the  $^{55}Mn$  hyperfine sextets observed experimentally. The solid curves derive from the best fit spin-Hamiltonian parameters of the  $S=1$   $Mn^{5+}$  ion, and the dashed curve derives from the  $S=3/2$   $Mn^{4+}$  ion, as discussed in the text.



Orientation of Magnetic Field

arises from a second type of paramagnetic manganese ion; its assignment is discussed below.

## V. ANALYSIS AND DISCUSSION

### A. $S=1$ Center

We employed crystal growth conditions designed to introduce manganese in its higher oxidation states, of which only  $Mn^{5+}$  admits a triplet spin state. The EPR rotation patterns clearly demonstrate that the manganese ions substitute for cations in the  $Ba_3(VO_4)_2$  structure; as noted above, both ionic charge and size ( $Mn^{5+}$ , ionic radius  $0.47 \text{ \AA}^{32}$ ) considerations clearly imply that the ions are incorporated in place of the  $V^{5+}$  ions, in tetrahedral coordination. Accordingly, the  $S=1$  manganese center in  $Ba_3(VO_4)_2$  is assignable as a tetrahedrally coordinated  $Mn^{5+}$  ion with energy levels as illustrated in Fig. 7.7.

The pentavalent manganese ion has a ground electronic configuration of  $[Ar]3d^2$  with the lowest energy Russell-Saunders term of  $^3F$ . In a weak tetrahedral crystal field the  $^3F$  term is split with the  $^3A_2$  state lying lowest. The existence of an isolated, orbitally non-degenerate ground state supports the observability of the  $Mn^{5+}$  EPR signals at room temperature.<sup>34</sup>

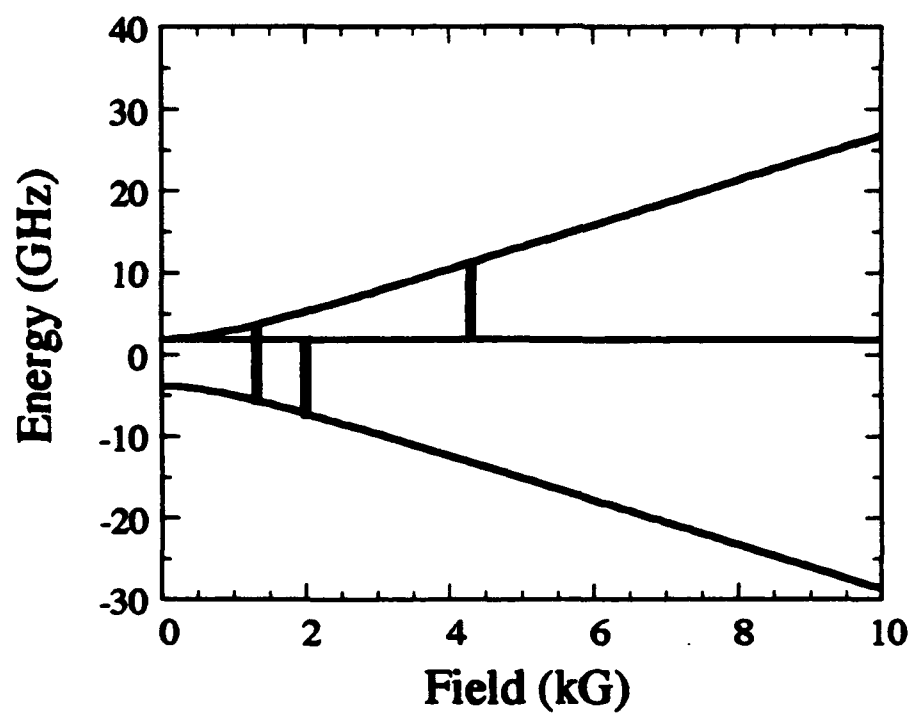
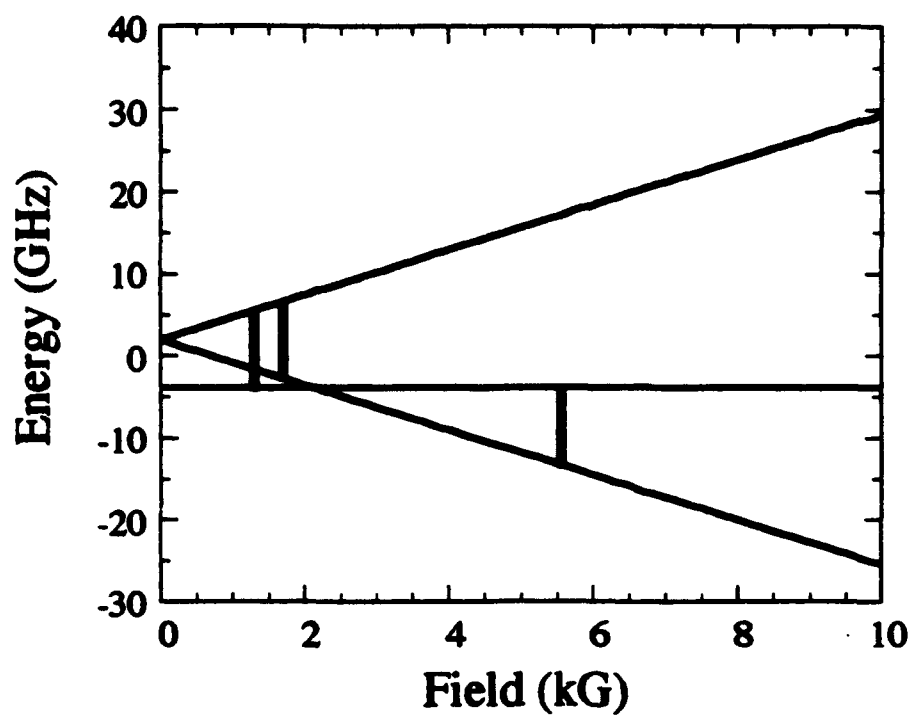
For the purpose of summarizing the EPR results, we may consider the conventional spin Hamiltonian,<sup>34</sup>

$$H = -|\mu_B| B_0 \cdot g \cdot S + D(S_z^2 - S \cdot S / 3) + S \cdot A \cdot I + I \cdot P \cdot I + g_n |\mu_n| B_0 \cdot I \quad (7-1)$$

in which  $|\mu_B|$  is the magnitude of the Bohr magneton and  $|\mu_n|$  the nuclear magneton;  $B_0$  is the external magnetic field;  $S$  is the electron spin operator with  $S=1$ , and  $I$  is the nuclear spin operator for  $^{55}Mn$  with  $I=5/2$ ;<sup>33</sup>  $g$ ,  $A$ , and  $P$  are axially symmetric matrices that represent the electron Zeeman interaction, the  $^{55}Mn$  hyperfine interaction, and the nuclear

**FIG 7.7.** Energy levels of the triplet spin, ground electronic state of  $\text{Mn}^{5+}$  in the presence of an external field aligned parallel (top panel) and perpendicular (bottom panel) to the  $z$  magnetic principal axis. The heavy lines show the transitions possible at 9.09 GHz.





quadrupole interaction, respectively;  $D$  is the fine structure interaction parameter; and  $g_n$  is the  $^{55}\text{Mn}$  nuclear  $g$  factor. The symmetry axis is taken as  $z$ . Principal values of the magnetic interaction matrices belonging to  $z$  are designated by the subscript  $\parallel$ , while those belonging to the principal axes orthogonal to  $z$  are designated with the subscript  $\perp$ . The spin Hamiltonian of Eq. (7-1) is suitable for detailed analysis of the EPR hyperfine multiplets, in particular, the small asymmetries in the line positions intensities that occur within the multiplets. We opt to ignore such subtleties, however, and employ a simplified method of analysis that nonetheless enables us to characterize the manganese centers sufficiently for comparison with related systems.

$D$  and  $g$  values were obtained by fitting the adjustable parameters of the first two terms of Eq. (7-1) to the center field values of the hyperfine multiplets. To perform this calculation we employed a Levenberg-Marquardt<sup>35</sup> non-linear fitting routine, together with an eigenfield algorithm similar to the one described by Belford *et al.*<sup>36</sup> The resonant field data utilized in the fitting procedure was limited to the values obtained for  $B_0$  in the  $ac$  plane. Best fit values were calculated for  $D$ ,  $g_{\parallel}$ , and  $g_{\perp}$ . In addition, a fourth parameter,  $\phi$ , was fit to account for any tilt of  $B_0$  out of the  $ac$  plane as a result of a misalignment of the crystal; a value of  $34\text{m}\pi$  was found for the parameter  $\phi$ . Best-fit spin Hamiltonian parameter values are shown in Table 7.2 together with  $\delta_{\text{rms}}$ , the root mean squared deviation between the observed and calculated resonant field values. These best-fit spin Hamiltonian parameter values were used to generate the solid curves in Fig. 7.6. Relative transition intensities were also calculated based on these values, and were found to be entirely consistent with the experimental observations.

In evaluating the principal values of the hyperfine interaction matrix,  $A$ , we neglect the mixing of the Zeeman states by both the hyperfine and fine structure interactions and utilize the simple perturbation formula:<sup>34</sup>

$$g^2 A^2 = g_{\parallel}^2 A_{\parallel}^2 \cos^2 \theta + g_{\perp}^2 A_{\perp}^2 \sin^2 \theta, \quad (7-2)$$

in which,

$$g^2 = g_{\parallel}^2 \cos^2 \theta + g_{\perp}^2 \sin^2 \theta, \quad (7-3)$$

$\theta$  is the angle between  $z$  ( $= c$ ) and  $B_0$ , and  $A$  is the mean value of the hyperfine splittings observed within each multiplet. Best fit values of  $A_{\parallel}^2$  and  $A_{\perp}^2$  were calculated by linear least squares fitting program based on Eqs. (7-2) and (7-3), from the data obtained with  $B_0$  in the  $ac$  plane. The resulting best fit values are shown in Table 7.3 and were used to generate the solid curve shown in Fig. 7.8.

The EPR data ascribed to the  $Mn^{5+}$  ion are well summarized by the  $S=1$  spin Hamiltonian. The parameter values obtained for the electron Zeeman, fine structure, and  $^{55}Mn$  hyperfine interactions are comparable to those of similar tetrahedral  $Mn^{5+}$  centers in apatite and spodiosite.<sup>20</sup> In all of these systems, the manganese centers have the following characteristics: small fine structure interactions with  $D \approx 4-15$  GHz; principal  $g$ -values that are all approximately equal to  $g_0$ , the free-electron  $g$ -value; and nearly isotropic  $^{55}Mn$  hyperfine interactions with isotropic coupling constants of  $\sim 58-70 \times 10^{-4} \text{ cm}^{-1}$ .<sup>20,21</sup> The  $g$ - and  $D$ -values appear to be typical for  $d^2$  ions — including  $Ti^{2+}$ ,<sup>37-40</sup>  $V^{3+}$ ,<sup>41-45</sup>  $Cr^{4+}$ ,<sup>46-48</sup> and  $Fe^{5+}$ .<sup>19,49</sup> In slightly distorted tetrahedral environments. In the tetrahedral sites of forsterite ( $Mg_2SiO_4$ ) and BMaG ( $Ba_2MgGe_2O_7$ ), however,  $Cr^{4+}$  exhibits a much larger fine structure interaction with respective  $D$ -values of  $\sim 2$  and  $\sim 4 \text{ cm}^{-1}$ .<sup>10,12-14</sup> For both of these systems, the optical spectra indicate that the lowest excited state derives from the  $^3T_2$  term,<sup>4,5,8</sup> rather than from  $^1E$  as in the studied tetrahedral  $Mn^{5+}$  systems.<sup>28-30</sup> This ordering reflects the impact that slightly weaker and more distorted ligand fields have on the position and the splitting of  $^3T_2$ ; these properties likewise largely determine the size of the fine structure parameters.<sup>8,50</sup>

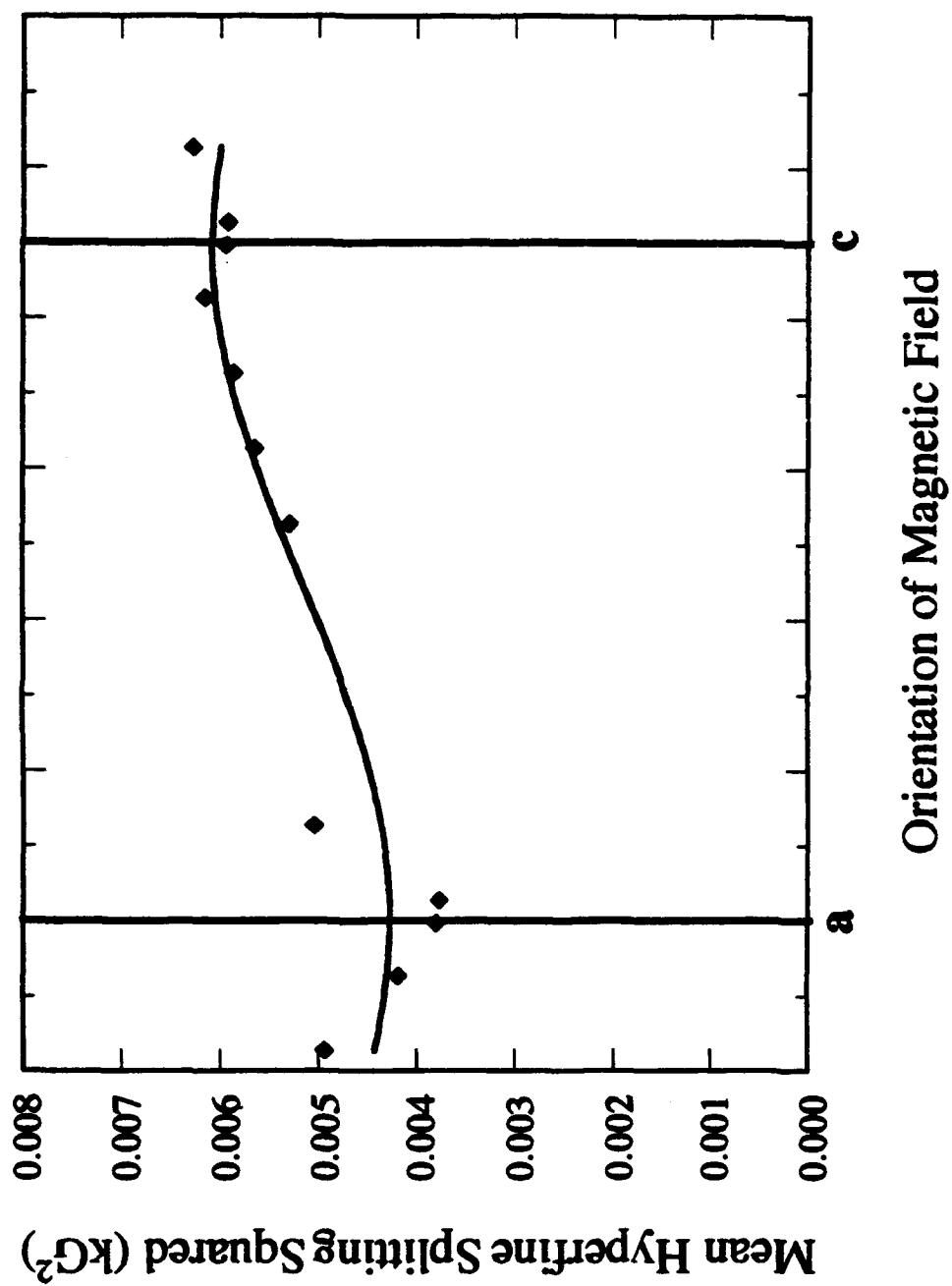
Parameter	Mn <sup>5+</sup>	Mn <sup>4+</sup>
$\delta_{ms}$ (G)	7.8	1.8
D (GHz)	$\pm 5.81$ (0.01)	$\pm 28$ (8)
$g_{  }$	1.9608 (0.0003)	1.977 (0.001)
$g_{\perp}$	1.9722 (0.0004)	1.985 (0.002)
$\phi$ (radians)	0.105 (0.003)	0.105

**TABLE 7.2.** Spin Hamiltonian parameters for  $S=3/2$  Mn<sup>4+</sup> and  $S=1$  Mn<sup>5+</sup> substituting for V<sup>5+</sup> in Ba<sub>3</sub>(VO<sub>4</sub>)<sub>2</sub> single crystals. The tabulated values (standard deviations in parentheses) are determined by least-squares adjustment as described in the text.

Parameter	Mn <sup>5+</sup>	Mn <sup>4+</sup>
$A_{  }$ (10 <sup>-4</sup> cm <sup>-1</sup> )	$\pm 70$ (10)	$\pm 80$ (4)
$A_{\perp}$ (10 <sup>-4</sup> cm <sup>-1</sup> )	$\pm 60$ (10)	$\pm 19$ (3)

**TABLE 7.3.** <sup>55</sup>Mn hyperfine interaction principal values for  $S=1$  Mn<sup>5+</sup> and  $S=3/2$  Mn<sup>4+</sup> substituting for V<sup>5+</sup> in Ba<sub>3</sub>(VO<sub>4</sub>)<sub>2</sub> single crystals. The tabulated values (standard deviations in parentheses) are determined by least-squares adjustment as described in the text.

**FIG 7.8.** Mean hyperfine splitting vs. orientation of  $B_0$  in the  $ac$  crystallographic plane for  $Mn^{5+}$  in  $Ba_3(VO_4)_2$ . The points are the experimental data, and the solid curves derive from the best fit hyperfine parameters, as described in the text.



## B. Additional Center

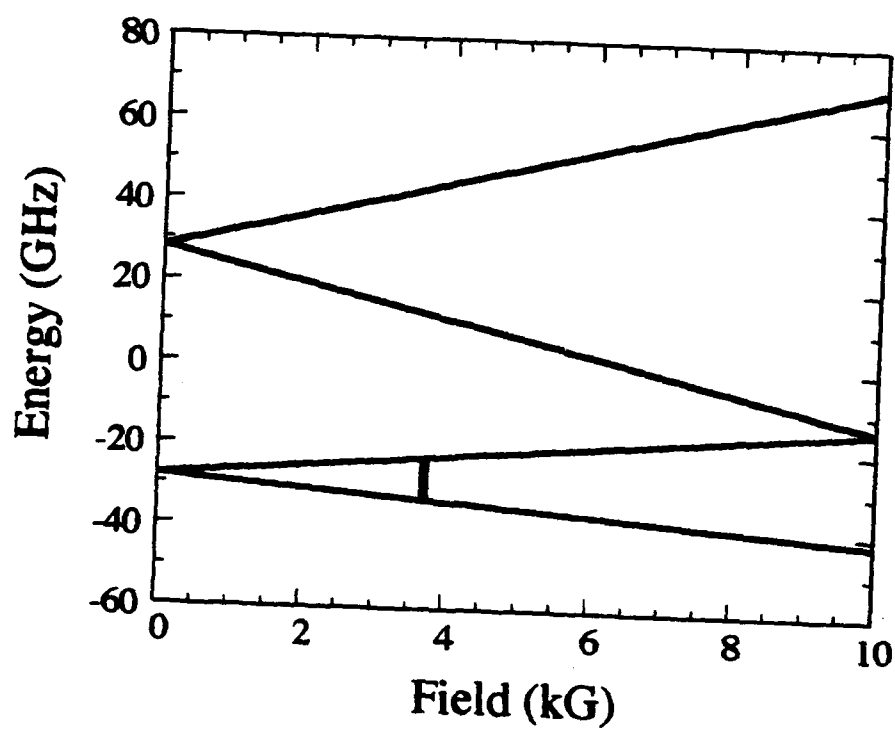
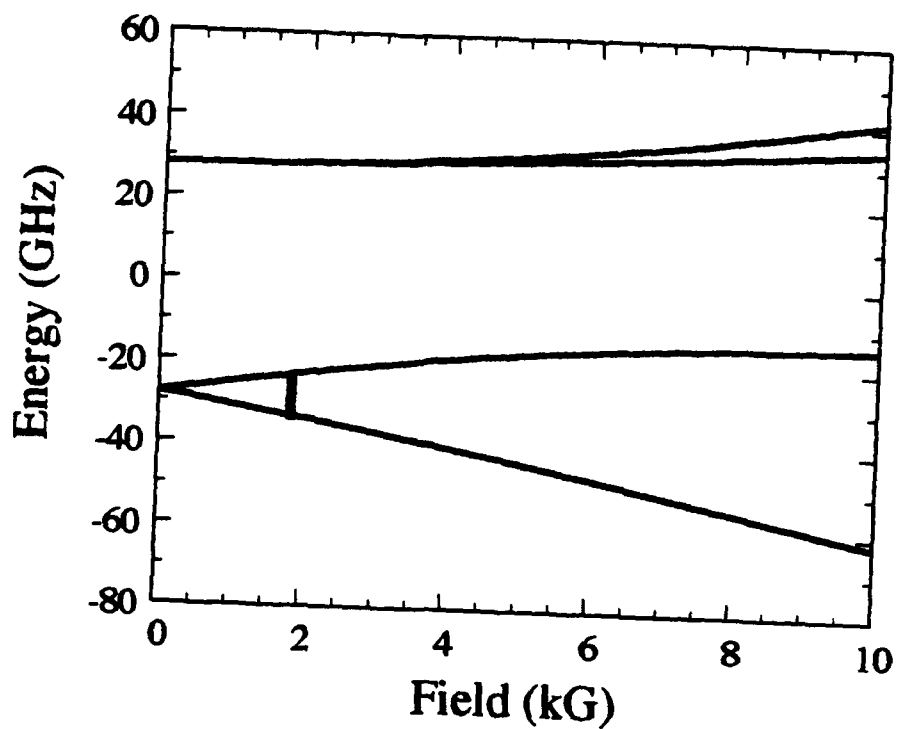
The remaining strong manganese EPR signal entails a single multiplet that exhibits a rotational pattern compatible with assignment as either an authentic  $S=1/2$  ion, or an effective doublet system — for example, an  $S=3/2$  system with a fine structure interaction sufficiently large that only the transitions between the  $\pm 1/2$  Zeeman levels are observable under our experimental conditions, as illustrated in Fig. 7.9. Given the oxidizing conditions for growth of the crystals, the only reasonable choices for the paramagnetic center are  $\text{Mn}^{4+}$  ( $S=1/2$  or  $S=3/2$ ) or  $\text{Mn}^{6+}$  ( $S=1/2$ ).

The tetravalent manganese ion has a ground electronic configuration of  $[\text{Ar}]3d^3$  with the lowest energy Russell-Saunders term of  $^4F$ . In a weak tetrahedral crystal field the  $^4F$  term is split with the  $^4T_1$  state lying lowest. Trigonal distortion of the ligand tetrahedron leads to either a  $^4A_2$  or a  $^4E$  ground state. In strong tetrahedral crystal fields the ground state is  $^2E$  with trigonal distortions producing no further splitting. Hexavalent manganese has a ground electronic configuration of  $[\text{Ar}]3d^1$  with a free ion term of  $^2D$ . In a tetrahedral crystal field, the  $^2D$  term is split with the  $^2E$  state lying lowest; trigonal distortions produce no further splitting. Of the three possibilities — high-spin  $\text{Mn}^{4+}$ , low-spin  $\text{Mn}^{4+}$ , or  $\text{Mn}^{6+}$  — only the first admits an orbitally non-degenerate ground state in  $C_{3v}$  symmetry, and would thus be most conducive to the detection of EPR at room temperature.

To muster additional support for this assignment, we explore the comparative suitability of spin Hamiltonians appropriate for either an  $S=1/2$  and  $S=3/2$  system to account for the experimental data of Fig. 7.6, specifically, the magnetic field strength at the center of the hyperfine multiplets. Relevant parameter values were calculated by a procedure analogous to that outlined above for the  $S=1$  ion. For the  $S=1/2$  treatment only the first term of Eq. (7-1) was considered; the adjustable parameters in the fit were limited to  $g_{\parallel}$  and  $g_{\perp}$ . For the  $S=3/2$  case, the first two terms of Eq. (7-1) were considered and both  $D$  and the  $g$ -values were adjusted.

**FIG 7.9.** Energy levels of the quartet spin, ground electronic state of  $\text{Mn}^{4+}$  in the presence of an external field aligned perpendicular (top panel) and parallel (bottom panel) to the  $z$  magnetic principal axis. The diagram illustrates the restrictions on possible EPR transitions of an  $S=3/2$  system that apply when the fine-structure interaction is large compared to the EPR frequency. The splitting ( $2D$ ) between the zero-field doublets is 56 GHz; the arrows show the transitions possible at 9.09 GHz.





For all calculations, resonant field data employed in the fitting procedure was limited to the values obtained for  $B_0$  in the  $ac$  plane. The parameter,  $\phi$ , was fixed to the value of  $34m\pi$  obtained for the  $S=1$  ion above. Best-fit spin Hamiltonian parameter values for both cases are shown in Table 7.4 together with  $\delta_{rms}$ , the root mean squared deviation between the observed and calculated resonant field values.

Two features of the best-fit values shown in Table 7.4 indicate that the assignment of the manganese center as an  $S=3/2$  ion is correct. First, the addition of  $D$  as an adjustable parameter results in a significant (by chi-square testing <sup>35</sup>) decrease in the value of  $\delta_{rms}$ . Second, according to the  $S=1/2$  treatment we find  $g_{\perp} \approx 4$ . While such a value, which greatly deviates from  $g_e$ , is not beyond the realm of possibility, the fact that  $g_{\perp}$  assumes a value that is very close to  $2g_e$  readily lends itself to an alternative, more plausible explanation. As detailed in the appendix, the  $S=3/2$  spin Hamiltonian matrix can be block factored, for large  $D$ , into  $\pm 1/2$  and  $\pm 3/2$  manifolds; the  $\pm 1/2$  manifold is identical to an  $S=1/2$  Hamiltonian matrix with a doubling of the value of  $g_{\perp}$ . The  $g$ -values shown in the first column of Table 7.4 may thus be regarded as a signature of an  $S=3/2$  system with  $g$ -values near  $g_e$ , but with a large fine structure interaction. Accordingly, we assign this center to high-spin,  $Mn^{4+}$  ion.

The best-fit spin Hamiltonian parameter values for the  $S=3/2$  ion were used to generate the dashed curve in Fig. 7.6. EPR transition intensities calculated for the  $S=3/2$  ion based on these best fit spin Hamiltonian parameter values were also found to be consistent with the experimental observations. As suggested by the illustrations in Fig. 7.9, the observation, under our experimental conditions, of only a single EPR transition — belonging to the  $M_s = \pm 1/2$  Zeeman levels of the  $S=3/2$  system — establishes that  $D$  must be larger than  $\sim 20$  GHz. The value of  $D$  obtained in the fitting procedure conforms to this requirement. Inasmuch as the effect of the fine structure interaction on the resonant energy levels varies as  $(g_{\perp} \mu_B B_0 \sin \theta)^2 / 2D$ , the precision with which the value of  $D$  is determined is modest. There is also a correspondingly a larger error in  $g_{\perp}$  than in  $g_{\parallel}$ : when  $B_0 \parallel z$ , the observed EPR transition has no dependence on  $D$ . To evaluate the hyperfine interaction parameters

Parameter	$S=1/2$	$S=3/2$ (Mn <sup>4+</sup> )
$\delta_{\text{rms}}$ (G)	3.7	1.8
D (GHz)	—	$\pm 28$ (8)
$g_{\parallel}$	1.980 (0.001)	1.977 (0.001)
$g_{\perp}$	3.955 (0.003)	1.985 (0.002)

**TABLE 7.4.** Spin Hamiltonian parameters for the “additional” manganese center, calculated by least-squares adjustment under the alternative assumptions:  $S=1/2$ , and  $S=3/2$ .

for the  $S=3/2$  center, we utilized Eqs. (7-2) and (7-3) in essentially the same manner employed for the  $S=1$  system. The best fit values of  $A_{\parallel}$  and  $A_{\perp}$  obtained for the  $S=3/2$  center are shown in Table 7.3. These values were used to generate solid curve in Fig. 7.10.

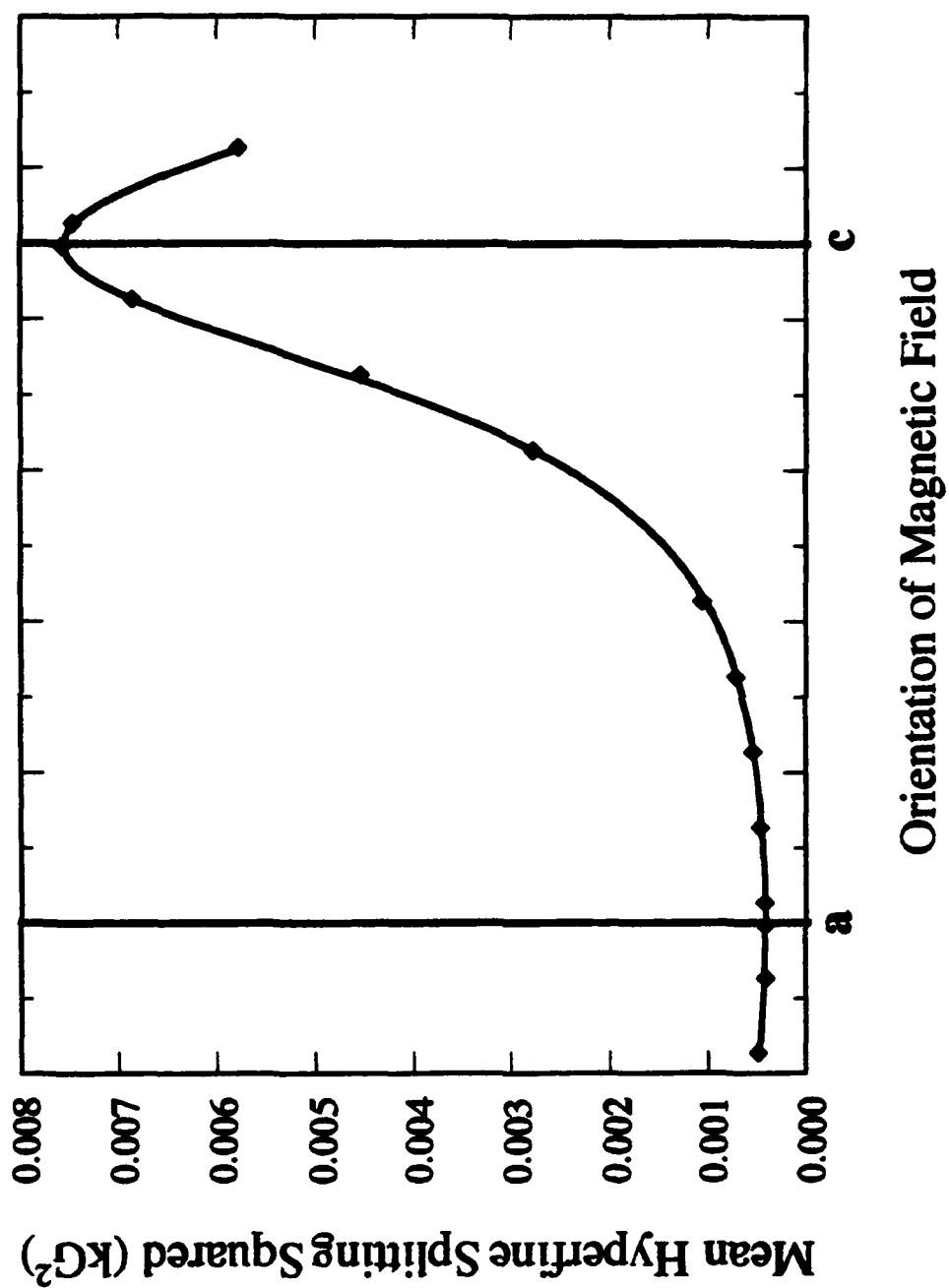
The  $Mn^{4+}$  ion is clearly revealed by the single crystal rotation patterns to occupy a cation site in the  $Ba_3(VO_4)_2$  structure. As noted above, ionic size considerations ( $Mn^{4+}$ , ionic radius 0.53 Å<sup>32</sup>) imply that the ions are incorporated in place of  $V^{5+}$ , in tetrahedral coordination. Such coordination of  $d^3$  ions is unusual, although not without precedent. Tetrahedral  $Cr^{3+}$  has been found in host crystals of  $Be_2SiO_4$ <sup>51</sup> and  $AlPO_4$ .<sup>52</sup> In addition, Mowat *et al.*<sup>46</sup> have described an organometallic complex,  $Cr(CH_2SiMe_3)^4$ , that contains tetrahedrally ligated  $Cr^{3+}$ . In all of these systems, only the  $\pm 1/2$  transition was observed in the EPR spectra because of the large value of  $D$ ;  $g$ -values near  $g_e$  were also reported for these systems. A few optical studies of tetrahedral  $Cr^{3+}$  have also been reported.<sup>53-55</sup>

The observation of  $Mn^{4+}$  centers in the  $Ba_3(VO_4)_2$  crystals is particularly intriguing because no such centers were reported in the studies of manganese-doped phosphates (apatites and spodosites).<sup>20</sup> Vanadate crystals are commonly darkened by the presence of defects that appear to involve  $V^{4+}$  ions.<sup>56</sup> It is tempting to suggest that in the manganese-doped vanadate, a fraction of the  $Mn^{5+}$  impurities oxidize the  $V^{4+}$  to the normal, vanadate valence state. This process would both eliminate  $V^{4+}$  paramagnetic centers, which were not detected in our EPR experiments, and yield the observed  $Mn^{4+}$  centers.

## VI. CONCLUSION

From this single crystal EPR study, we have demonstrated the incorporation of two distinct paramagnetic manganese centers at cation sites in  $Ba_3(VO_4)_2$ . Analysis of their EPR spectra indicates that the two centers are high-spin  $Mn^{5+}$  and  $Mn^{4+}$  ions, with relative abundances of  $\sim 5:1$ . Although the exact substitution position can not be positively determined from the EPR spectroscopy — as both  $Ba^{2+}$  and  $V^{5+}$  occupy positions of similar crystallographic symmetry — it is certain that the  $Mn^{4+}$  and  $Mn^{5+}$  ions, with radii of

**FIG 7.10.** Mean hyperfine splitting vs. orientation of  $B_0$  in the *ac* crystallographic plane for  $Mn^{4+}$  in  $Ba_3(VO_4)_2$ . The points are the experimental data, and the solid curves derive from the best fit hyperfine parameters, as described in the text.



0.53 Å and 0.47 Å respectively, substitute for the nearly equivalent tetrahedral  $V^{5+}$  (0.50 Å) rather than the much larger  $Ba^{2+}$  (1.56 Å) ion.<sup>32</sup> The presence of  $Mn^{4+}$  in tetrahedral lattice sites has not been reported previously, although the isoelectronic  $Cr^{3+}$  ion has been observed in tetrahedral coordination.<sup>51-55</sup> The spin Hamiltonian parameters obtained for the  $Mn^{5+}$  center are consistent with values found for  $Mn^{5+}$  and for other  $d^2$  ions in slightly distorted tetrahedral environments.<sup>19-21,37-49</sup> The fine structure interaction is substantially smaller, however, than exhibited by  $Cr^{4+}$  in the tetrahedral sites of forsterite.<sup>10,12-14</sup>

#### ACKNOWLEDGEMENTS

Support of this work by the Army Research Office (DAAL03-90-0113) and helpful conversations with Dr. Al Pinto are gratefully acknowledged.

### Appendix: $S=3/2$ with $D \gg h\nu$

The fine structure and Zeeman terms of the spin Hamiltonian of an  $S=3/2$  ion in an axial field can be represented in the basis of high field Zeeman states  $\{1/2, -1/2, 3/2, -3/2\}$  as,

$$\begin{pmatrix} -D + \frac{1}{2}a & b & \sqrt{3}b & 0 \\ b & -D - \frac{1}{2}a & 0 & \sqrt{3}b \\ \sqrt{3}b & 0 & D + \frac{3}{2}a & 0 \\ 0 & \sqrt{3}b & 0 & D - \frac{3}{2}a \end{pmatrix} \quad (7-4)$$

in which,

$$a = g_1 |\mu_B| B_0 \cos \vartheta, \quad (7-5)$$

and

$$b = g_1 |\mu_B| B_0 \sin \vartheta. \quad (7-6)$$

If  $2D$ , the separation between the  $\pm 1/2$  and  $\pm 3/2$  manifolds, is much larger than the resonance frequency, then the matrix elements connecting them are negligible, and the matrix is effectively block diagonalized. In this situation, EPR transitions are forbidden within the  $\pm 3/2$  manifold but are allowed within the  $\pm 1/2$  manifold, the spin Hamiltonian of which is represented, apart from an inconsequential scalar term, as:

$$\frac{1}{2} \cdot \begin{pmatrix} g_1 |\mu_B| B_0 \cos \vartheta & 2g_1 |\mu_B| B_0 \sin \vartheta \\ 2g_1 |\mu_B| B_0 \sin \vartheta & -g_1 |\mu_B| B_0 \cos \vartheta \end{pmatrix} \quad (7-7)$$

This form is identical to the spin Hamiltonian matrix of an  $S=1/2$  system, provided that one identifies

$$g_1 (S = \frac{1}{2}) = 2g_1 (S = \frac{3}{2}). \quad (7-8)$$

The factor of two in (7-8) proceeds from the  $S$ -dependence of the matrix elements of the operators  $S_{\pm}$ . An analogous result also applies to the hyperfine interaction.



## REFERENCES

- [1] V. Petricevic, S.K. Gayen, R.R. Alfano, K. Yamagishi, H. Anzai, and Y. Yamaguchi, *Appl. Phys. Lett.* **52**, 1040 (1988).
- [2] V. Petricevic, S.K. Gayen, and R.R. Alfano, *Appl. Phys. Lett.* **53**, 2590 (1988).
- [3] H.R. Verdún, L.M. Thomas, D.M. Andrauskas, T. McCollum, and A. Pinto, *Appl. Phys. Lett.* **53**, 2593 (1988).
- [4] V. Petricevic, S.K. Gayen, and R.R. Alfano, in *OSA Proceedings on Tunable Solid State Lasers*, edited by M.L. Shand and H.P. Jensen (Optical Society of America, Washington, DC, 1989), Vol. 5, p. 77.
- [5] H.R. Verdún, L.M. Thomas, D.M. Andrauskas, and A. Pinto, in *OSA Proceedings on Tunable Solid-State Lasers*, edited by M.L. Shand and H.P. Jensen (Optical Society of America, Washington, DC, 1989), Vol. 5, p. 85.
- [6] R. Moncorgé, D.J. Simkin, G. Cormier, and J.A. Capobianco, in *OSA Proceedings on Tunable Solid State Lasers*, edited by M.L. Shand and H.P. Jensen (Optical Society of America, Washington, DC, 1989), Vol. 5, p. 93.
- [7] W. Jia, L. Lu, B.M. Tissue, and W.M. Yen, *J. Cryst. Growth* **109**, 329 (1991).
- [8] W. Jia, H. Liu, S. Jaffe, W.M. Yen, and B. Denker, *Phys. Rev. B* **43**, 5234 (1991).
- [9] R. Moncorgé, G. Cormier, D.J. Simkin, and J.A. Capobianco, *IEEE J. Quantum Electron.* **27**, 114 (1991).
- [10] V.G. Baryshevski, M.V. Korzhik, M.G. Livshitz, A.A. Tarasov, A.E. Kimaev, I.I. Mishel, M.L. Meilman, B.J. Minkov, and A.P. Shkandarevich, in *OSA Proceedings on Advanced Solid-State Lasers*, edited by G. Dubé and L. Chase (Optical Society of America, Hilton Head, NC, 1991), Vol. 10, p. 26.
- [11] K.R. Hoffman, S.M. Jacobsen, J. Casas-Gonzalez, and W.M. Yen, in *OSA Proceedings on Advanced Solid-State Lasers*, edited by G. Dubé and L. Chase (Optical Society of America, Washington, DC, 1991), Vol. 10, p. 44.
- [12] K.R. Hoffman, J. Casas-Gonzalez, S.M. Jacobsen, and W.M. Yen, *Phys. Rev. B* **44**, 12589 (1991).
- [13] M.H. Garrett, V.H. Chan, H.P. Jensen, M.H. Whitmore, A. Sacra, D.J. Singel, and D.J. Simkin, in *OSA Proceedings on Advanced Solid-State Lasers*, edited by G. Dubé and L. Chase (Optical Society of America, Washington, DC, 1991), Vol. 10, p. 76.
- [14] M.H. Whitmore, A. Sacra, and D.J. Singel, *J. Chem. Phys.*, in press.
- [15] T.S. Rose, R.A. Fields, M.H. Whitmore, and D.J. Singel, in *OSA Proceedings on Advanced Solid-State Lasers*, edited by L.L. Chase and A.A. Pinto (Optical Society of America, Washington, DC, 1992), Vol. 13, p. 17.
- [16] T.S. Rose, M.H. Whitmore, R.A. Fields, and D.J. Singel, *J. Am. Opt. Soc.:B*, submitted for publication.
- [17] N.B. Angert, N.I. Borodin, V.M. Garmash, V.A. Zhitnyuk, A.G. Okhrimchuk, O.G. Siyuchenko, and A.V. Shestakov, *Sov. J. Quantum Electron.* **18**, 73 (1988).

- [18] B.H.T. Chai, Y. Shimony, C. Deka, X.X. Zhang, E. Munin, and M. Bass, in *OSA Proceedings on Advanced Solid-State Lasers*, edited by L.L. Chase and A.A. Pinto (Optical Society of America, Washington, DC, 1992), Vol. 13, p. 28.
- [19] A. Carrington, D.J.E. Ingram, K.A.K. Lott, D.S. Schonland, and M.C.R. Symons, *Proc. R. Soc. A* **254**, 101 (1960).
- [20] H. Lachwa and D. Reinen, *Inorg. Chem.* **28**, 1044 (1989).
- [21] D. Reinen, H. Lachwa, and R. Allmann, *Z. Anorg. Allg. Chem.* **542**, 71 (1986).
- [22] J. D. Kingsley, J.S. Prener, and B. Segall, *Phys. Rev.* **137**, A189 (1965).
- [23] R. Borromei, L. Oleari, and P. Day, *J. Chem. Soc., Faraday Trans. 2* **73**, 135 (1977).
- [24] R. Borromei, L. Oleari, and P. Day, *J. Chem. Soc., Faraday Trans. 2* **77**, 1563 (1981).
- [25] R. Borromei and E. Fisicaro, *Chim. Ital.* **109**, 191 (1979).
- [26] J. Milstein and S.L. Holt, *Inorg. Chem.* **8**, 1021 (1969).
- [27] J.B. Milstein, J. Ackerman, S.L. Holt, and B.R. McGarvey, *Inorg. Chem.* **11**, 1178 (1972).
- [28] J.A. Capobianco, G. Cormier, R. Moncorgé, H. Manaa, and M. Bettinelli, *Appl. Phys. Lett.* **60**, 163 (1992).
- [29] M. Herren, J. Güdel, C. Albrecht, and D. Reinen, *Chem. Phys. Lett.* **183**, 98 (1991).
- [30] L.D. Merkle, A. Pinto, H.R. Verún, and B. McIntosh, *Appl. Phys. Lett.* **61**, 2386 (1992).
- [31] P. Süsse and M.J. Buerger, *Z. Kristallogr.* **131**, 161 (1970).
- [32] J.E. Huheey, *Inorganic Chemistry* (Harper and Row, New York, NY, 1983).
- [33]  $^{55}\text{Mn}$  ( $I=5/2$ ) occurs with 100. % natural abundance.
- [34] A. Abragam and B. Bleaney, *Electron Paramagnetic Resonance of Transition Ions* (Dover Publications, Inc., New York, NY, 1970).
- [35] W.H. Press, B.P. Flannery, S.A. Teukolsky, and W.T. Vetterling, *Numerical Recipes* (Cambridge University Press, , 1986).
- [36] G.G. Belford, R.L. Belford, and J.F. Burkhalter, *J. Mag. Res.* **11**, 251 (1973).
- [37] J. Schneider and A. Räuber, *Phys. Lett.* **21**, 380 (1966).
- [38] J. Dziesiaty and R. Böttcher, *Phys. Stat. Sol.* **26**, K21 (1968).
- [39] M.M. Zaripov, V.S. Kropotov, and L.D. Livanova, *Fiz. Tverd. Tela* **9**, 1265 (1967).
- [40] M.M. Zaripov, V.S. Kropotov, L.D. Livanova, and V.G. Stepanov, *Fiz. Tverd. Tela* **9**, 2985 (1967).
- [41] W.C. Holton, J. Schneider, and T.L. Estle, *Phys. Rev.* **133**, A1638 (1964).
- [42] H.H. Woodbury and G.W. Ludwig, *Bull. Am. Phys. Soc.* **6**, 118 (1961).

- [43] M.M. Zaripov, V.S. Kropotov, L.D. Livanova, and V.G. Stepanov, *Fiz. Tverd. Tela* **9**, 209 (1967).
- [44] M.M. Zaripov, V.S. Kropotov, L.D. Livanova, and V.G. Stepanov, *Doklady AN SSSR* **173**, 1043 (1967).
- [45] M.M. Zaripov, V.S. Kropotov, L.D. Livanova, and V.G. Stepanov, *Fiz. Tverd. Tela* **10**, 325 (1968).
- [46] W. Mowat, A. Shortland, G. Yagupsky, N.J. Hill, M. Yagupsky, and G. Wilkinson, *J. C. S. Dalton* (7), 533 (1972).
- [47] W. Mowat, A.J. Shortland, N.J. Hill, and G. Wilkinson, *J. C. S. Dalton* (4), 770 (1973).
- [48] E.C. Alyea, J.S. Basi, D.C. Bradley, and M.H. Chisholm, *J. Chem. Soc. A* **5**, 772 (1971).
- [49] R. Debuyst, F. Dejehet, and D. Apers, *J. Inorg. Nucl. Chem.* **37**, 338 (1975).
- [50] J.E. Wertz and J.R. Bolton, *Electron Spin Resonance* (Chapman and Hall, New York, NY, 1986).
- [51] M. Tsukioka and H. Kojima, *J. Phys. Soc. Jap.* **35**, 818 (1973).
- [52] J.C.M. Henning, J. Liebertz, and R.P.V. Stapele, *J. Phys. Chem. Solids* **28**, 1109 (1967).
- [53] E.C. Alyea, J.S. Basi, D.C.B. ., and M.H. Chisholm, *Chem. Comm.* , 495 (1968).
- [54] D.J. Machin, D.F.C. Morris, and E.L. Short, *J. Chem. Soc.* , 4659 (1962).
- [55] D.H. Brown, *J. Chem. Soc.* , 3322 (1962).
- [56] K. Chow and H. G. McKnight, *Mat Res. Bull.* **8**, 1343 (1973). G. A. Anderson and W. D. Compton, *J. Chem. Phys.* **52**, 6166 (1970). M. Sayer, H. Erdogan and C. D. Cox, *Electrochem. Soc.* **119**, 265 (1972).

## **Chapter 8.**

### **Electron Paramagnetic Resonance Spectroscopy of Chromium-Doped Lanthanum Lutetium Gallium Garnet.**

**Electron Paramagnetic Resonance Spectroscopy of  
Chromium-Doped Lanthanum Lutetium Gallium Garnets.**

Michael H. Whitmore and David J. Singel

*Department of Chemistry, Harvard University,  
12 Oxford Street, Cambridge, Massachusetts 02138*

**ABSTRACT**

EPR (electron paramagnetic resonance) spectra of single crystals of the solid-state laser material, chromium-doped lanthanum lutetium gallium garnet (LLGG), are reported. The spectra reveal the incorporation of  $\text{Cr}^{3+}$  ions at tetrahedral  $\text{Ga}^{3+}$  sites. These results are at variance with the work of Lewis (Appl. Phys. **A52**, 31 (1991)) who suggested the presence of  $\text{Cr}^{3+}$  in octahedral sites with severe distortions.

## I. INTRODUCTION

Chromium ions are well known to substitutionally incorporate as  $\text{Cr}^{3+}$  at octahedral sites in a variety of garnets — including YAG,<sup>1-4</sup> YGG,<sup>5,6</sup> and GSGG.<sup>7</sup> This substitution is of significance for both the activation and radiation protection of lasers made from such materials. Recently, Lewis reported the single crystal EPR (electron paramagnetic resonance) investigation of  $\text{Cr}^{3+}$  centers in chromium-doped lanthanum lutetium gallium garnet (LLGG), a material of specific interest owing to its unusually large octahedral sites.<sup>8</sup> The EPR spectra obtained for LLGG were, however, vastly different from those found for other chromium-doped garnets systems. Lewis accounted for these unusual spectra by postulating substantial distortion of the octahedral sites occupied by the  $\text{Cr}^{3+}$  ions.

In current work, we are utilizing EPR spectroscopy to characterize the incorporation of  $3d^2$  ions in host crystals with potential as near IR, tunable solid state lasers. In particular, we have investigated the Cr:forsterite laser ( $\text{Cr}:\text{Mg}_2\text{SiO}_4$ ),<sup>9-12</sup> for which the active species was assigned to  $\text{Cr}^{4+}$  substituting for  $\text{Si}^{4+}$  at tetrahedral lattice sites, and the Mn: $\text{Ba}_3(\text{VO}_4)_2$  laser,<sup>13</sup> for which the active center was assigned to  $\text{Mn}^{5+}$  substituting for tetrahedral  $\text{V}^{5+}$ .<sup>14</sup> The latter material also showed the presence of  $\text{Mn}^{4+}$  at the tetrahedral sites — an unusual coordination geometry for a  $3d^3$  ion.<sup>14</sup> The report of near IR laser activity in chromium-doped garnets, ascribed to tetrahedral  $\text{Cr}^{4+}$  centers,<sup>15,16</sup> motivated us to examine the EPR spectrum of chromium-doped LLGG. In this letter we report the results of this study. In agreement with Lewis,<sup>8</sup> we attribute the dominant EPR lines in LLGG to  $\text{Cr}^{3+}$  ions. We suggest, however, that these ions are lodged — like the  $\text{Mn}^{4+}$  centers in barium vanadate<sup>14</sup> — at tetrahedral lattice sites.

## II. EXPERIMENTAL METHODS

Single crystals of chromium-doped LLGG were obtained from Dr. M. R. Kokta of Union Carbide Corporation. The crystals were medium green in color and free of visible

flaws. The samples were cut into right triangular prisms with faces perpendicular to the [100], the [110] and (nominally) the [111] directions; the latter face was misaligned by approximately 30 m $\mu$ . Sample volumes were approximately 0.01 to 0.02 cm<sup>3</sup>.

EPR experiments were performed with a Varian E-109 X-band spectrometer using 100kHz modulation and a Varian E-231 TE<sub>102</sub> rectangular cavity. The field was varied over a range of 0.05 to 10 kG and measured with a Walker Scientific MG-3D gaussmeter that was calibrated with a Micro-Now Instruments Model 515B-1 proton gaussmeter. Observations were obtained at frequencies of 9.5 GHz. Most experiments were carried out with samples at ambient temperatures, although some were performed at temperatures of approximately 100 K and 10 K. Low temperatures were achieved using either a Varian E-257 Variable Temperature Accessory or an Air Products LTD-3-110 HeliTran liquid He transfer system. The sample crystals were rotated for field orientation studies with a Varian goniometer system described previously.<sup>11</sup>

### III. RESULTS AND ANALYSIS

Measurements were made on LLGG with magnetic field rotation in the (100), (110), and the nominal (111) crystallographic planes. Only three major EPR features are found at room temperature. The first consists of two or three symmetry related lines (approximately 50-60 G in width) which are observed in all three planes. These lines are several times larger than any other signals; we assign them to chromium ions. The second consists of a single line (approximately 50 G in width) which remains stationary in all three planes at a resonance field of 3451 G. The third, observed only with  $B_0$  in (100) and (110), consists of a single line (approximately 20 G in width) which remains nearly stationary at 2513 G and has appreciable intensity only with  $B_0$  within  $\pm 20^\circ$  of [100]. In addition, a number of broad and weak transitions were observed at resonance field below 1750 G. Typical spectra for LLGG are shown in Figures 8.1 and 8.2.

**FIG 8.1.** Typical EPR spectra of chromium-doped LLGG with  $B_0$  along a  $[100]$  direction and  $B_1$  along a second  $[100]$  direction. The two large lines arise from chromium ions at tetrahedral lattice sites.



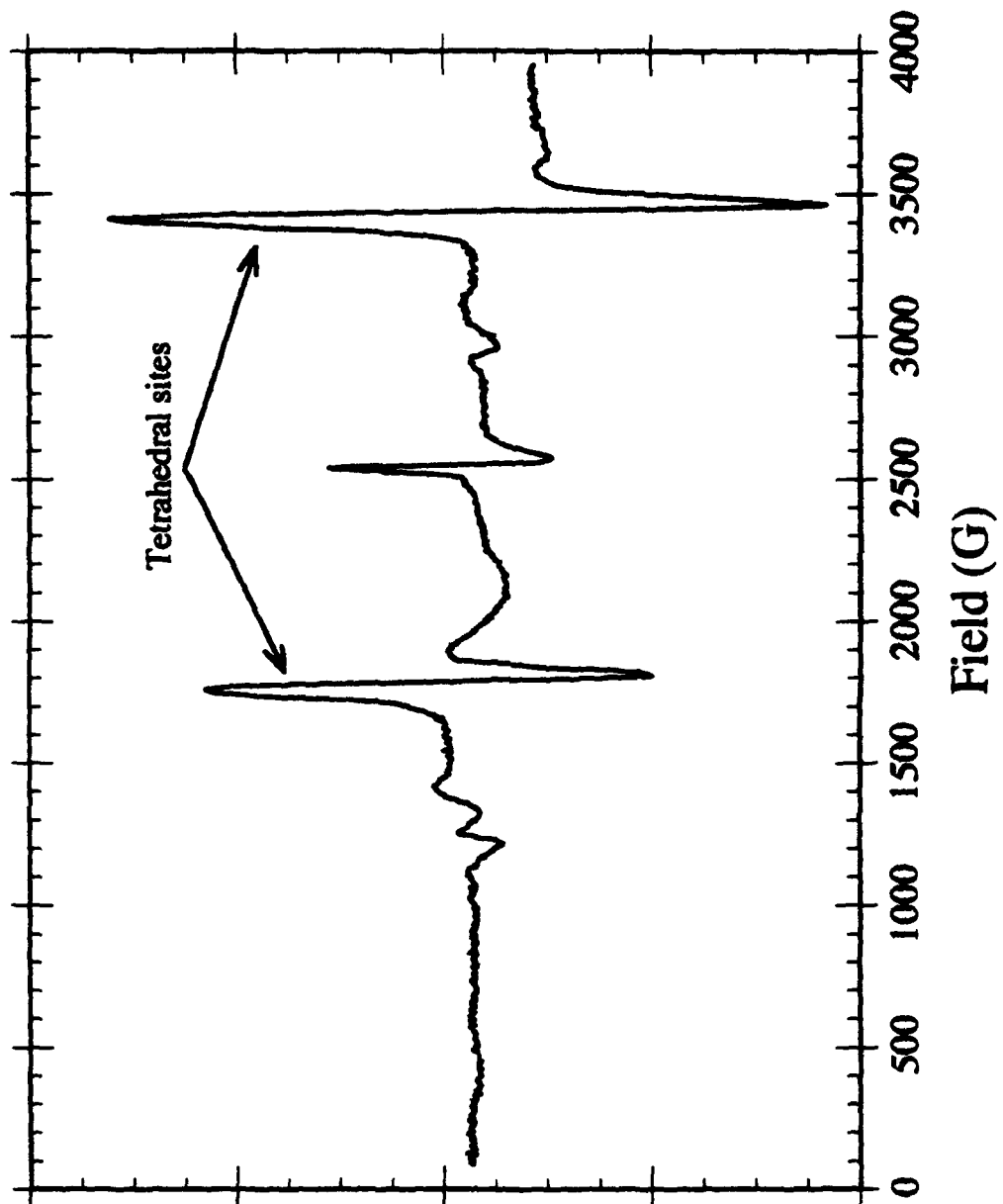
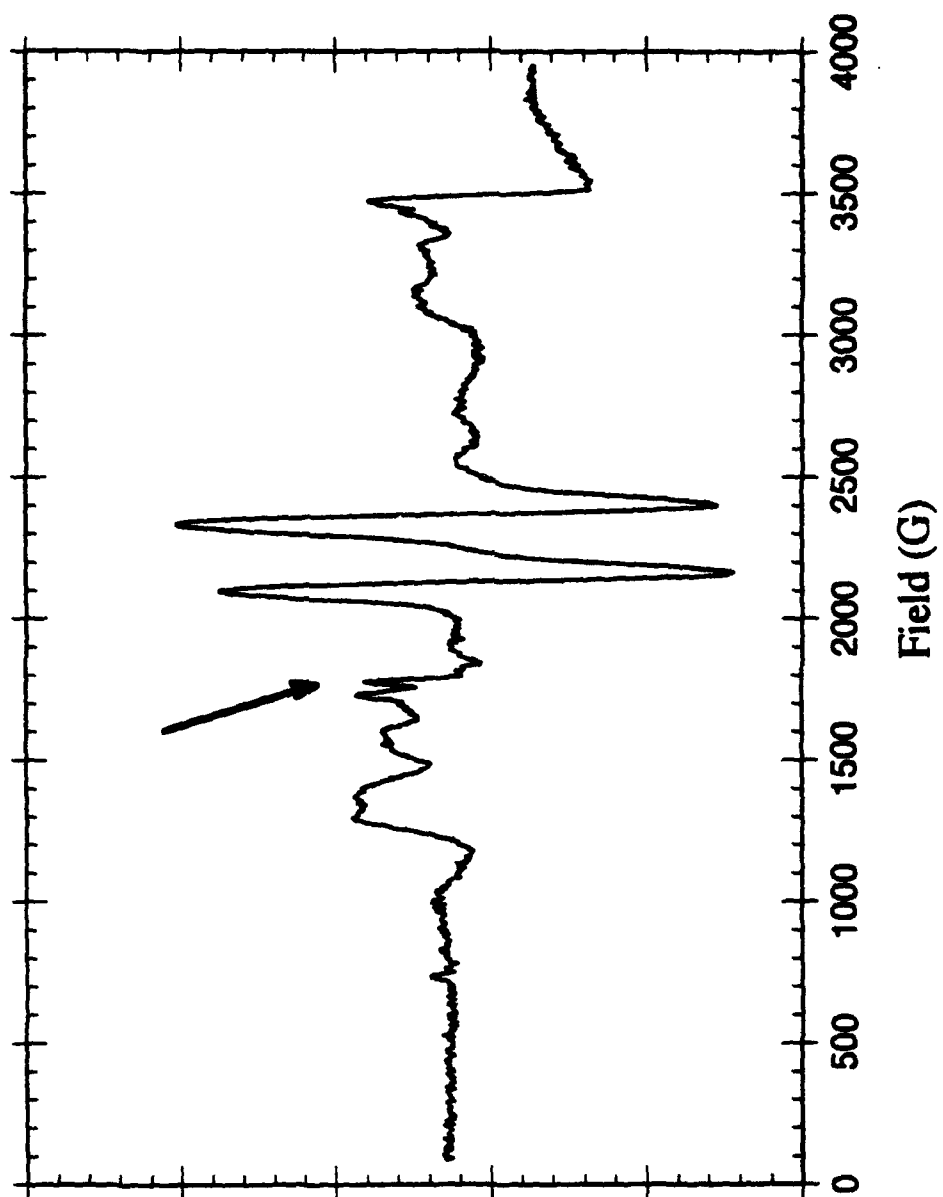


**FIG 8.2.** Typical EPR spectra of chromium-doped LLGG with  $B_0$  along a  $[100]$  direction and  $B_1$  along a second  $[100]$  direction. The two large lines arise from chromium ions at tetrahedral lattice sites. The arrow shows the weaker EPR line from the third tetrahedral site.



The fields-for-resonance of the chromium lines were measured as a function of orientation of  $B_0$  within the (110), (100), and the nominal (111) crystallographic planes. The results for the latter two planes are shown as the plotted points in Figures 8.3 and 8.4. The presence of two lines moving  $90^\circ$  out of phase for rotation of  $B_0$  in the (100) plane and the existence of line extrema for  $B_0$  along [100] indicate that the signals originate from tetrahedral sites (see appendix 1). This is in contrast to patterns expected for ions located at octahedral sites, for which the resonant field extrema should occur with  $B_0$  along [110]. The curves also reveal that only one resonance transition is observed for each magnetically inequivalent site.

The assignment to tetrahedral sites is further confirmed by the observation of the three lines moving (approximately)  $60^\circ$  out of phase for  $B_0$  rotation in the nominal (111) plane. Differences in the resonance field maxima of the three lines for rotation in this plane are due to misalignment of the crystal: this misalignment allows  $B_0$  to make a slightly different angle with each tetrahedral site's z-axis. On the other hand, regardless of misalignment,  $B_0$  must still pass perpendicular to the z-axis of each site for rotation of the field near this plane. Thus the resonance-field for each line should be equivalent at one extrema: this is the case for the minima of each line.

There is one anomaly in this analysis of the signals: the absence, for field rotation in the (100) plane, of the line that corresponds to the tetrahedral site for which  $B_0$  is always in perpendicular to z (see appendix 1). The results above indicate that this line should remain stationary at the resonance field minima of the two symmetry related lines actually observed in this plane. To resolve this conflict, spectra were taken with  $B_0$  rotation in the (110) plane and specifically with  $B_0$  aligned along [110]. These spectra show two strong lines: one at a resonance field corresponding to the crossing of the two lines for  $B_0$  along [110] in the (100) plane and a second corresponding to the missing line in the (100) plane. With this in mind, careful examination of spectra with  $B_0$  rotation in the (100) plane revealed the predicted stationary line, albeit at much lower intensity than observed for

**FIG 8.3.** Field-for-resonance vs. orientation of  $B_0$  in the (100) crystallographic plane for chromium in LLGG. The points are the experimental data.

# Cr-doped LLG Garnet

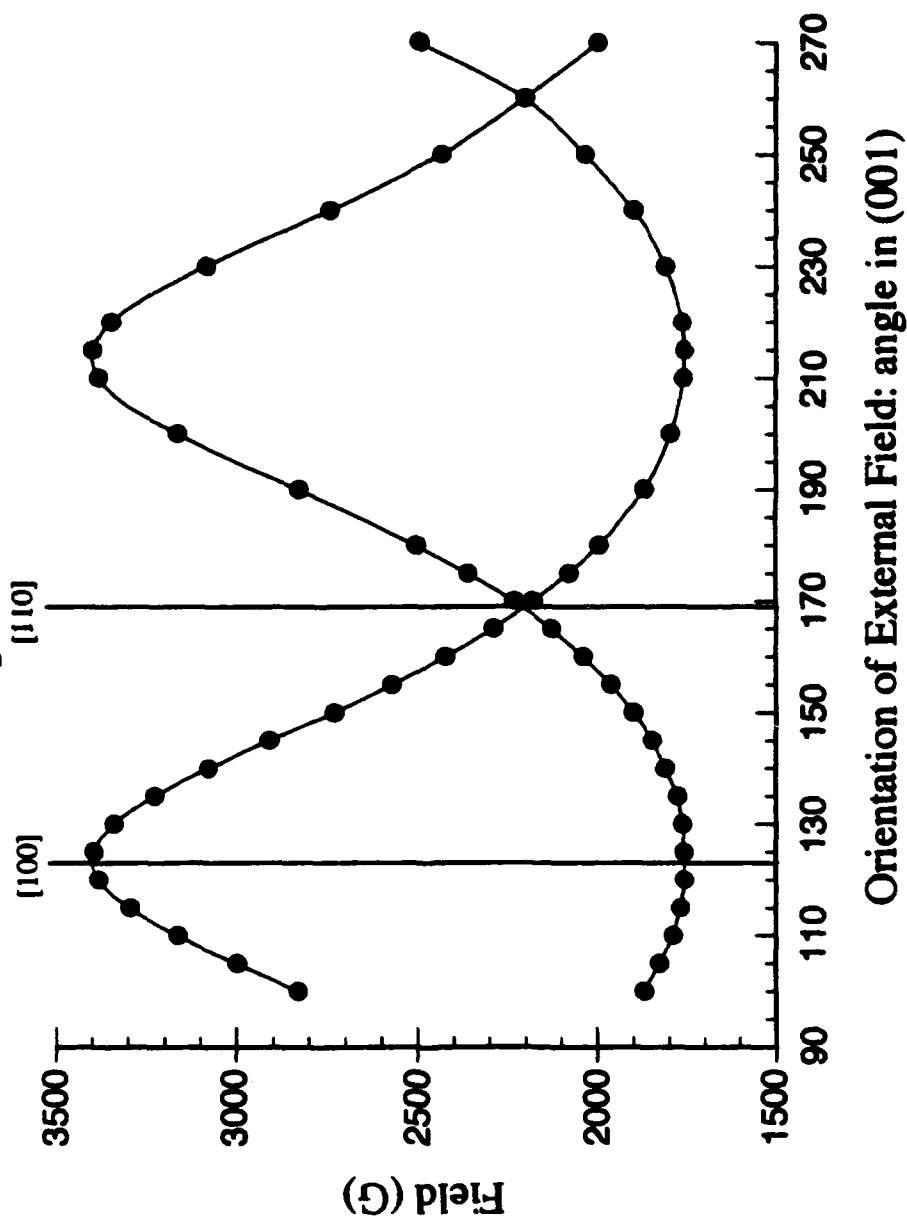
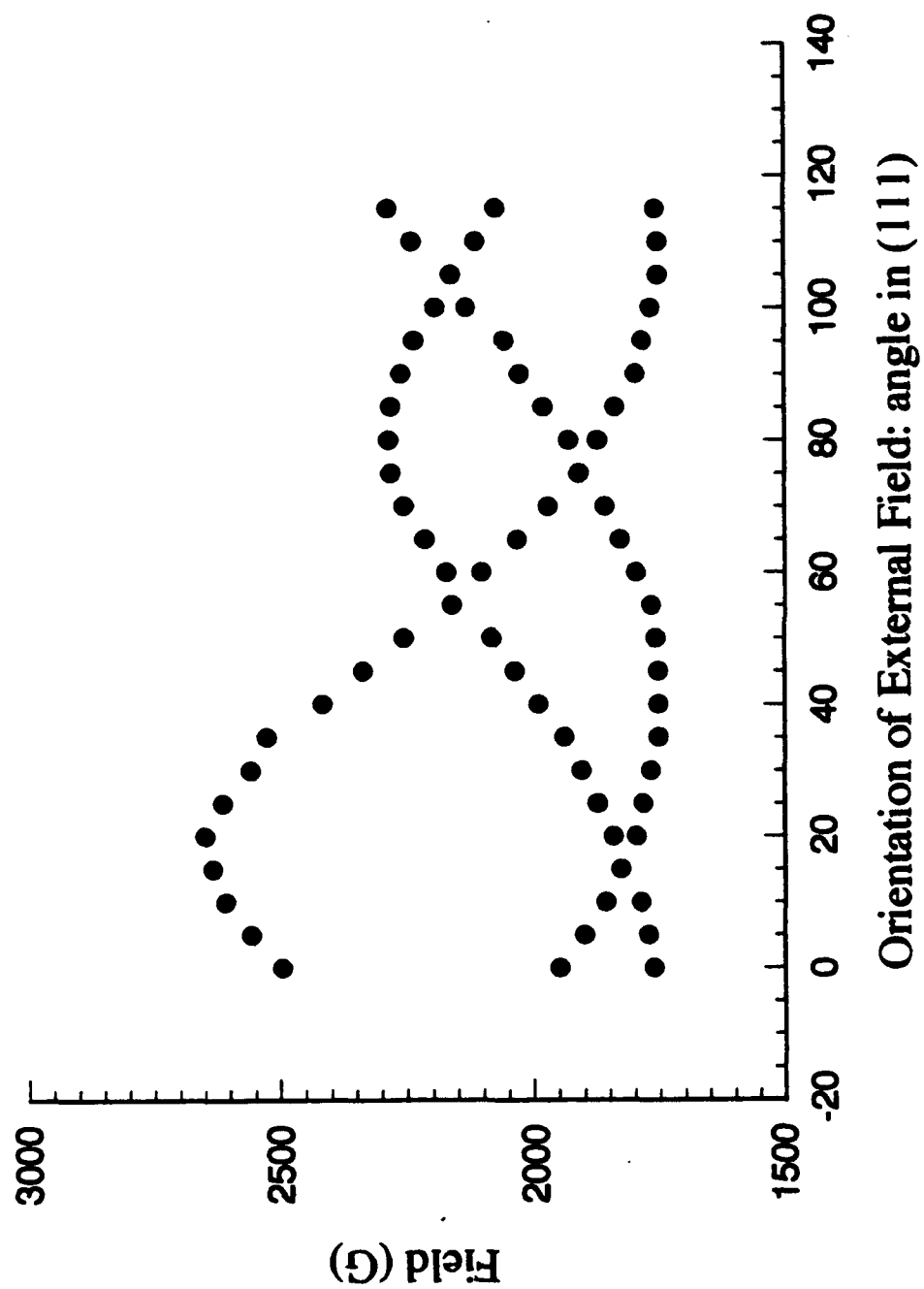


**FIG 8.4.** Field-for-resonance vs. orientation of  $B_0$  near the (111) crystallographic plane for chromium in LLGG. The points are the experimental data. As explained in the text the different maxima for the three curves are due to misalignment of the crystal which allows  $B_0$  to make a different angle with each sites magnetic  $z$ -axis.

## Cr-doped LLG Garnet





either the corresponding line in the (110) plane or the other two symmetry related lines in the (100) plane; this low intensity line is indicated in Figure 8.2 by an arrow. It is evident from these findings that the intensity of the observed transition is dependent on the orientation of the microwave field,  $B_1$ . For rotation of  $B_0$  in (100), the site corresponding to the stationary line has  $B_1$  along its z-axis, whereas for rotation of  $B_0$  in (110) the same site has  $B_1$  perpendicular to its z-axis;  $B_1$  is also perpendicular to the z-axes of the sites corresponding to the two strong transitions observed for rotation of  $B_0$  in the (100) plane.

In assigning the proper spin multiplicity to the chromium center in LLGG three key observations must be accounted for: 1) the presence of only a single resonance absorption per magnetically inequivalent site in the surveyed field range, 2) the dependence of the intensity of the signal on the microwave field orientation within the crystal, and 3) the existence of a resonance field maxima for  $B_0$  along the ion's magnetic z-axis and corresponding minima for  $B_0$  perpendicular to this axis. These results indicate the signal arises from the  $S=\pm 1/2$  transition of an  $S=3/2$   $Cr^{3+}$  ion with a large D splitting.

Lewis<sup>8</sup> observed signals similar to ours for rotation of  $B_0$  in the (1,-2,1) plane of LLGG and analyzed them in terms of  $S=3/2$   $Cr^{3+}$ . He obtained an isotropic  $g=1.978$  and a fine structure splitting, D, of approximately 14.4 GHz.<sup>8</sup> Although these parameter values are reasonably consistent with the single transition we observed, spectral simulations indicate that these values should produce several additional strong transitions in the 0 to 10 kG range (see appendix 2) which were not detected in our more detailed study. As these additional transitions would move outside our experimental field range for  $D \sim 20$  GHz, and the  $S=\pm 1/2$  transition is relatively insensitive to the value of D, we suspect the true D value to be somewhat higher than that predicted by Lewis.

#### IV. DISCUSSION

Chromium cation substitution in LLGG can potentially occur at either octahedral or tetrahedral lattice sites. In undistorted garnet the site symmetry of the former is  $\bar{3}$  while

that of the latter is  $\bar{4}$ ; both imply uniaxial magnetic interaction parameters ( $E=0$ ) with the unique fine structure axis oriented along the  $[111]$  directions for octahedral sites and along  $[100]$  directions for tetrahedral sites. This orientation of axes in turn implies specific patterns of magnetic equivalences and field-for-resonance extrema when  $B_0$  is rotated in the (100) plane. For ions at tetrahedral positions there are three magnetically inequivalent sites: two with signals that move  $\pi/2$  out of phase and have extrema for  $B_0$  parallel to a  $[100]$  direction and a third with signals stationary at an extrema. For ions at octahedral positions, there are two magnetically inequivalent pairs of sites. Signals for the pairs move  $\pi/2$  out of phase and have extrema for  $B_0$  parallel to a  $[110]$  direction. The data reported here are clearly compatible with assignment to ions at tetrahedral sites both in the vanishing of  $E$  and in the orientation of magnetic axes.

On the basis of ionic radii considerations, chromium cation substitution in the LLGG lattice is most likely at those sites for which  $Ga^{3+}$  occupation is also possible. At the time of Lewis's report,  $Ga^{3+}$  was thought to occupy all tetrahedral and a small fraction (~3%) of the octahedral sites in LLGG.<sup>17</sup> It was therefore feasible to suggest that  $Cr^{3+}$  ions could occupy distorted octahedral sites similar to those thought to be inhabited by  $Ga^{3+}$ . The recent, more detailed, report of Parise *et al.*,<sup>18</sup> however, shows  $Ga^{3+}$  to occupy only tetrahedral sites with all octahedral sites occupied by the much larger lutetium. If we assume an incorporation of  $Cr^{3+}$  ions in the LLGG lattice analogous to that of  $Ga^{3+}$  ions (which have equivalent charge and ionic radii), then our observations outlined above are quite reasonable. On the other hand,  $Cr^{3+}$  ions would pay a price in ligand field stabilization energy for incorporation in tetrahedral rather than octahedral coordination. These ions might therefore have a preference for placement at octahedral sites. Such a preference is implicitly assumed by Lewis.<sup>8</sup> If this view is correct, then to explain the EPR spectra,  $Cr^{3+}$  octahedra in LLGG should be characterized by a distortion that moves the fine structure axes from parallel to the  $[111]$  directions to parallel to the  $[100]$  directions while nonetheless maintaining an axial fine structure interaction ( $E=0$ ). Such a distortion,

while possible, is implausible, especially in view of the nonexistence of octahedral sites occupied by  $\text{Ga}^{3+}$ . We believe that the simplest explanation of the experimental results is to assign  $\text{Cr}^{3+}$  to the tetrahedral sites. Although tetrahedrally coordinate  $d^3$  ions are rare, they are not unprecedented. Tetrahedral  $\text{Cr}^{3+}$  has been found in host crystals of  $\text{Be}_2\text{SiO}_4$ <sup>19</sup> and  $\text{AlPO}_4$ .<sup>20</sup> Mowat *et al.*<sup>21</sup> have described an organometallic complex,  $\text{Cr}(\text{CH}_2\text{SiMe}_3)^4$ , that contains tetrahedrally ligated  $\text{Cr}^{3+}$ . In addition, tetrahedral  $\text{Mn}^{4+}$  has been reported in  $\text{Ba}_3(\text{VO}_4)_2$ .<sup>14</sup> In all of these systems, only the  $\pm 1/2$  transition is observed in the EPR spectra because of the large size of D, and g-values near  $g_e$  are found. These results are very similar those reported by us above and by Lewis<sup>8</sup> for  $\text{Cr}^{3+}$  in LLGG. In contrast, EPR studies of octahedral coordinate  $\text{Cr}^{3+}$  in YAG and YGG have found smaller D-values with several EPR transitions observed.<sup>1,5,6</sup> A few optical studies of tetrahedral  $\text{Cr}^{3+}$  have also been reported.<sup>22,23,24</sup>

It is puzzling that no EPR signals from tetrahedral  $\text{Cr}^{4+}$  ions are observed in LLGG — though it is possible that some of the smaller lines, which were not analyzed, could arise from this center. At this time, the only account of  $\text{Cr}^{4+}$  ions in garnet is that of Akhmadulin *et al.*, who report acoustic EPR of octahedral  $\text{Cr}^{4+}$  in YAG.<sup>25</sup> A possible rationale for the lack of observed tetrahedral  $\text{Cr}^{4+}$  signals in garnets is a large D splitting for the chromium ion in combination with the tetrahedral site's axial symmetry. Chromium ions located at axially symmetric sites would have a fine structure parameter  $E = 0$ , making it impossible to detect the type of transitions that have been observed for tetrahedral  $d^2$  ions in forsterite,<sup>11</sup> BMaG,<sup>11</sup> and  $\text{Ba}_3(\text{VO}_4)_2$ .<sup>14</sup> If the chromium ion had a D splitting considerably larger than the microwave quanta, detection of signals would only be possible in a very narrow range of crystal orientations for the magnetic field strengths used here (see appendix 2).

## Appendix I: Crystal Structure of LLGG

Garnets have the general molecular formula  $\{A\}_3\{B\}_2\{C\}_3O_{12}$  where A is a trivalent rare earth or uranium group ion in dodecahedral coordination, B is a trivalent iron group ion in octahedral coordination, and C is a trivalent iron group ion in tetrahedral coordination.<sup>26</sup> In mixed garnets, such as LLGG, there is partial replacement of A ions by B ions and B ions by C ions. It has been possible to dope garnets with a great variety of trivalent cations, as well as charge compensated tetravalent and bivalent cations. Regardless of composition, garnet crystals are of cubic symmetry with the space group  $1a3d$ . The structure is composed of  $O^{2-}$  ions linking a six-coordinate  $B^{3+}$  ion, a four-coordinate  $C^{3+}$  ion and two eight coordinate  $A^{3+}$  ions.<sup>27</sup> Eight  $\{A\}_3\{B\}_2\{C\}_3O_{12}$  formula units constitute the unit cell. The  $A^{3+}$  ions are situated at the crystallographic 24c positions, the  $B^{3+}$  ions at the 16a positions and the  $C^{3+}$  ions at the 24d positions.<sup>26</sup> All of the cation positions are located at invariant, specific coordinates, whereas the  $O^{2-}$  ion's general coordinates, as well as the lattice constant  $a$ , vary for differently constituted garnets. Lanthanum lutetium gallium garnet (LLGG) has a nominal formula  $La_3Lu_2Ga_3O_{12}$ , but electron microprobe analysis shows an actual distribution corresponding approximately to the formula  $\{La_{2.37}Lu_{0.55}\}[Lu_{2.0}](Ga_{3.0})O_{12}$ .<sup>18</sup> Crystallographic data for LLGG is given in Table 8.1.

As the ionic radii of the  $A^{3+}$  ions is quite large compared to that of  $Cr^{3+}$  or  $Cr^{4+}$ , incorporation of chromium through cationic substitution can occur only at the 16a or 24d positions. The former have site symmetry  $\bar{3}$ , whereas the latter have site symmetry  $\bar{4}$ . Ions at the 16a positions have trigonal distortions of the octahedra such that the  $\bar{3}$  axis lies along one the four  $[111]$  directions of the cubic crystal. In addition, pairs of ions sharing a common distortion axis are rotated in opposite directions about this axis by an angle of  $\pm\alpha$  for a total of eight possible magnetically inequivalent sites.<sup>28</sup> Fortunately, ions with electron spins of  $S=3/2$  or less are magnetically indistinguishable for rotation about a symmetry axis;

Ion	Site	Sym.	Coordinates			q
			x	y	z	
La	24c	222	0	0.2500	0.1250	+3
Lu	16a	$\bar{3}$	0	0	0	+3
Ga	24d	$\bar{4}$	0	0.2500	0.3750	+3
O	96h	T	0.0300	0.0576	0.6569	-2

**TABLE 8.1.** Crystallographic data for LLGG ( $\text{La}_3\text{Lu}_2\text{Ga}_3\text{O}_{12}$ ). Cubic  $\text{Ia}\bar{3}\text{d}_1$ .

$a=12.930 \text{ \AA}$ .<sup>17</sup>

therefore, there will be only four magnetically distinguishable sites, each with axial symmetry about one of the four  $[111]$  directions.

Ions at the 24d positions have tetragonal distortions of the tetrahedra such that the  $\bar{4}$  axis lies along one of the four  $[100]$  directions of the cubic crystal. In addition, pairs of ions sharing a common distortion axis are rotated in opposite directions about this axis by an angle of  $\pm\beta$  for a total of six possible magnetically inequivalent sites.<sup>28</sup> As above, only half of these sites will be magnetically distinguishable for ions of  $S=3/2$  or less, and thus there will be only three magnetically distinguishable sites. Each site will have axial symmetry about one of the three  $[100]$  directions.

Due to the multiple orientations of the symmetry axes for ions at both the octahedral and tetrahedral sites, the patterns of magnetic equivalencies are complex. For ions located at octahedral sites, a magnetic field,  $B_0$ , along a  $[111]$  direction produces one inequivalent site with  $B_0$  along the site's symmetry axis, conventionally labeled  $z$ , and three equivalent sites each with  $B_0$  at an angle of  $70.5^\circ$  to the ions'  $z$  axes.  $B_0$  along a  $[110]$  direction produces two pairs of equivalent sites; the first with  $B_0$  perpendicular to  $z$  and the second with  $B_0$   $35.3^\circ$  to  $z$ .  $B_0$  along the  $[100]$  direction produces four equivalent sites with  $B_0$  at  $54.7^\circ$  to the ions'  $z$  axes.

For octahedral sites rotation of  $B_0$  in the  $(111)$  plane produces three inequivalent sites for which  $B_0$  moves from perpendicular to  $z$  to  $19.5^\circ$  to  $z$ ; there is a  $60^\circ$  phase difference with respect to the field orientation between the each of the three sites. For the fourth inequivalent site  $B_0$  is constantly perpendicular to  $z$ . Rotation of  $B_0$  in the  $(110)$  plane produces two inequivalent sites for which  $B_0$  moves from parallel to  $z$  for each site (along  $[111]$ ) to perpendicular to  $z$  for each site  $109.5^\circ$  out of phase. These sites are equivalent with  $B_0$  along the  $[110]$  direction. The remaining two sites are always equivalent as  $B_0$  moves from perpendicular to  $z$  (along  $[110]$ ) to  $54.5^\circ$  to  $z$  (along  $[100]$ ). All four sites are equivalent with  $B_0$  along  $[100]$ . Finally, rotation of  $B_0$  in the  $(100)$  plane produces two

pairs of equivalent sites for which  $B_0$  moves from perpendicular to  $z$  (along one  $[110]$ ) to  $35.3^\circ$  to  $z$  (along a second  $[110]$ )  $90^\circ$  out of phase for the two pairs; all sites are equivalent for  $B_0$  along  $[100]$ .

For ions located at tetrahedral sites,  $B_0$  along a  $[111]$  direction produces three equivalent sites each with  $B_0$  at  $54.7^\circ$  to each site's  $z$  axis.  $B_0$  along the  $[110]$  direction produces a pair of equivalent sites for which  $B_0$  is  $45^\circ$  to each site's  $z$  and a third site for which  $B_0$  is perpendicular to the site's  $z$ . Finally,  $B_0$  along the  $[100]$  direction produces a pair of sites with  $B_0$  perpendicular to  $z$  and a single site with  $B_0$  parallel to  $z$ .

For tetrahedral sites, rotation of  $B_0$  in the  $(111)$  plane produces three inequivalent sites for which  $B_0$  moves from perpendicular to  $z$  to  $35.3^\circ$  to  $z$ ; there is a  $60^\circ$  phase difference with respect to orientation of the field between each site. Rotation of  $B_0$  in the  $(110)$  plane produces a single site for which  $B_0$  moves from parallel to  $z$  (along  $[100]$ ) to perpendicular to  $z$  (along  $[110]$ ) and a pair of equivalent sites for which  $B_0$  moves from perpendicular to  $z$  (along  $[100]$ ) to  $45^\circ$  to  $z$  (along  $[110]$ ); all sites are equivalent for  $B_0$  along  $[111]$ . Rotation of  $B_0$  in the  $(100)$  plane produces a single site for which  $B_0$  remains constantly perpendicular to  $z$  and a pair of sites for which  $B_0$  moves from perpendicular to  $z$  (along  $[100]$ ) to parallel to  $z$  (along a second  $[100]$ ). The latter two sites are equivalent with  $B_0$  along  $[110]$  and move  $90^\circ$  out of phase with respect to orientation of  $B_0$ .

The disparate patterns of magnetic equivalences for the octahedral and tetrahedral sites should permit ready identification of the crystallographic position of a substituted ion. Rotation in the  $(110)$  plane should provide complete specification for an ion incorporated at an octahedral site: for two sites  $B_0$  moves from parallel to the unique axis,  $z$ , to the axial plane, perpendicular to  $z$ . In the same way rotation in the  $(100)$  plane should provide complete specification for an ion incorporated at a tetrahedral site.

## APPENDIX 2: Simulations

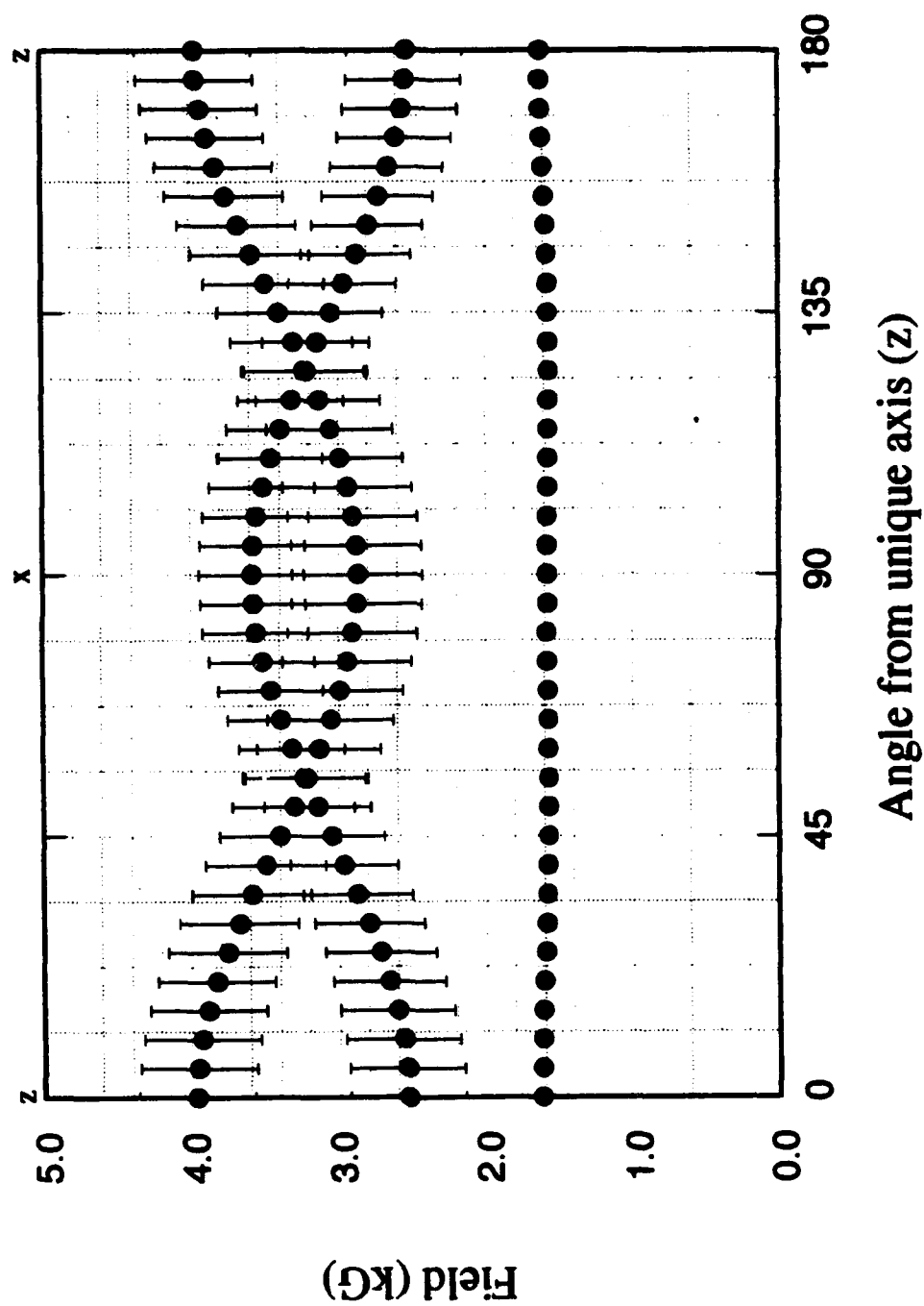
The following figures are spectral simulations of  $S=1$  and  $S=3/2$  centers in sites of axial symmetry — such as  $\text{Cr}^{4+}$  and  $\text{Cr}^{3+}$  in the octahedral and tetrahedral sites in garnets — for various values of the fine structure parameter,  $D$ . The figures plot angle of orientation of  $\mathbf{B}_0$  in a plane containing the unique axis,  $z$ , (i.e., the (100) plane in garnet for tetrahedral sites) *versus* signal resonance field. These plots were calculated using the eigenfield algorithm given in the appendix and the spin Hamiltonian,

$$H = -|\mu_B| \mathbf{B}_0 \cdot \mathbf{g} \cdot \mathbf{S} + D (S_z^2 - S \cdot S / 3)$$

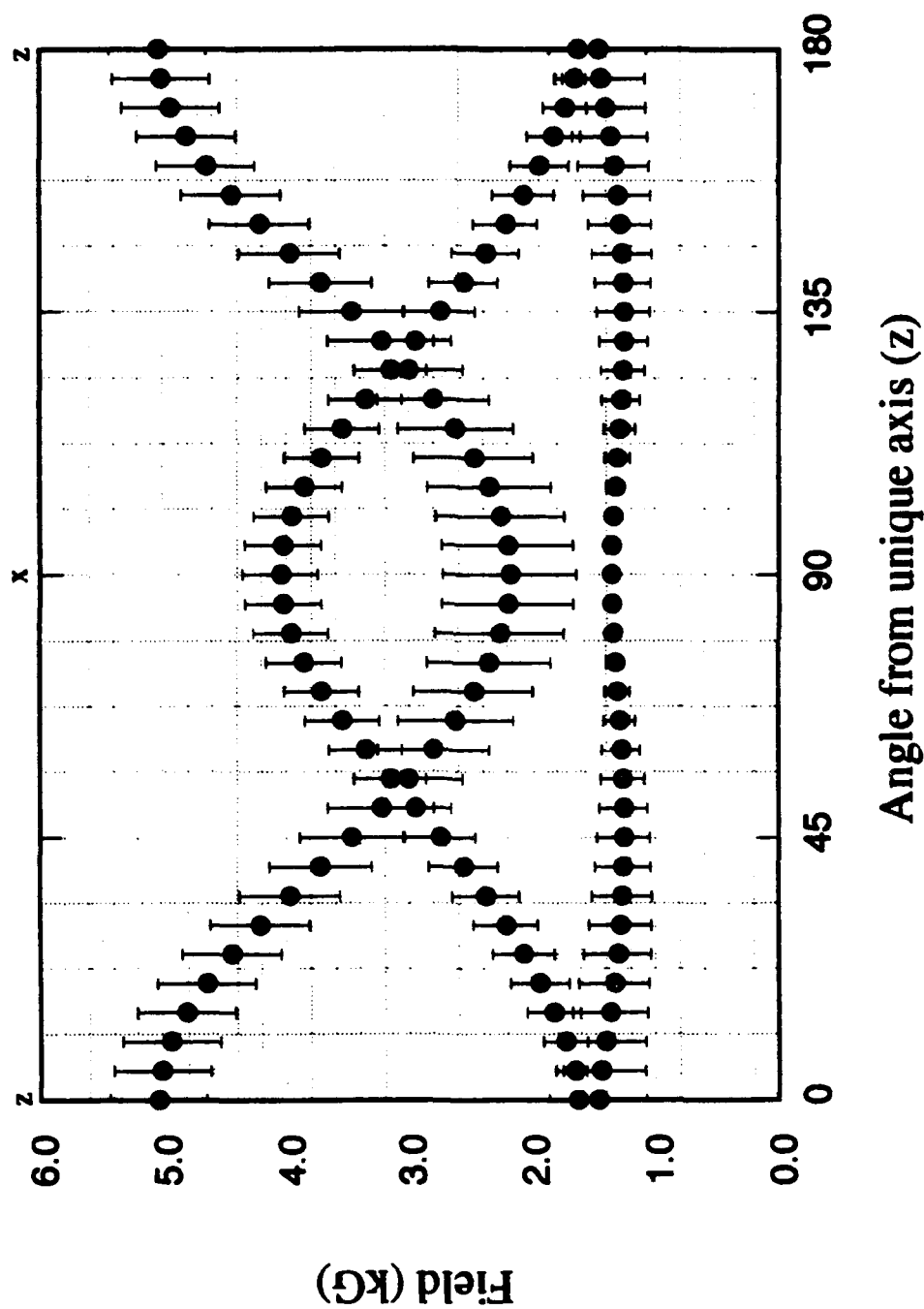
in which  $|\mu_B|$  is the magnitude of the Bohr magneton,  $\mathbf{B}_0$  is the laboratory field,  $\mathbf{g}$  is the Zeeman interaction matrix,  $\mathbf{S}$  is the electron spin operator, with  $S=1$  or  $S=3/2$ , and  $D$  is the fine structure parameter;  $x$ ,  $y$ , and  $z$  comprise the principal axes of the fine structure interaction. To simplify the calculations  $\mathbf{g}$  was assumed to be isotropic with a value of approximately  $g_e$ . Relative signal intensities were also calculated and are shown as the error bars on the data points.



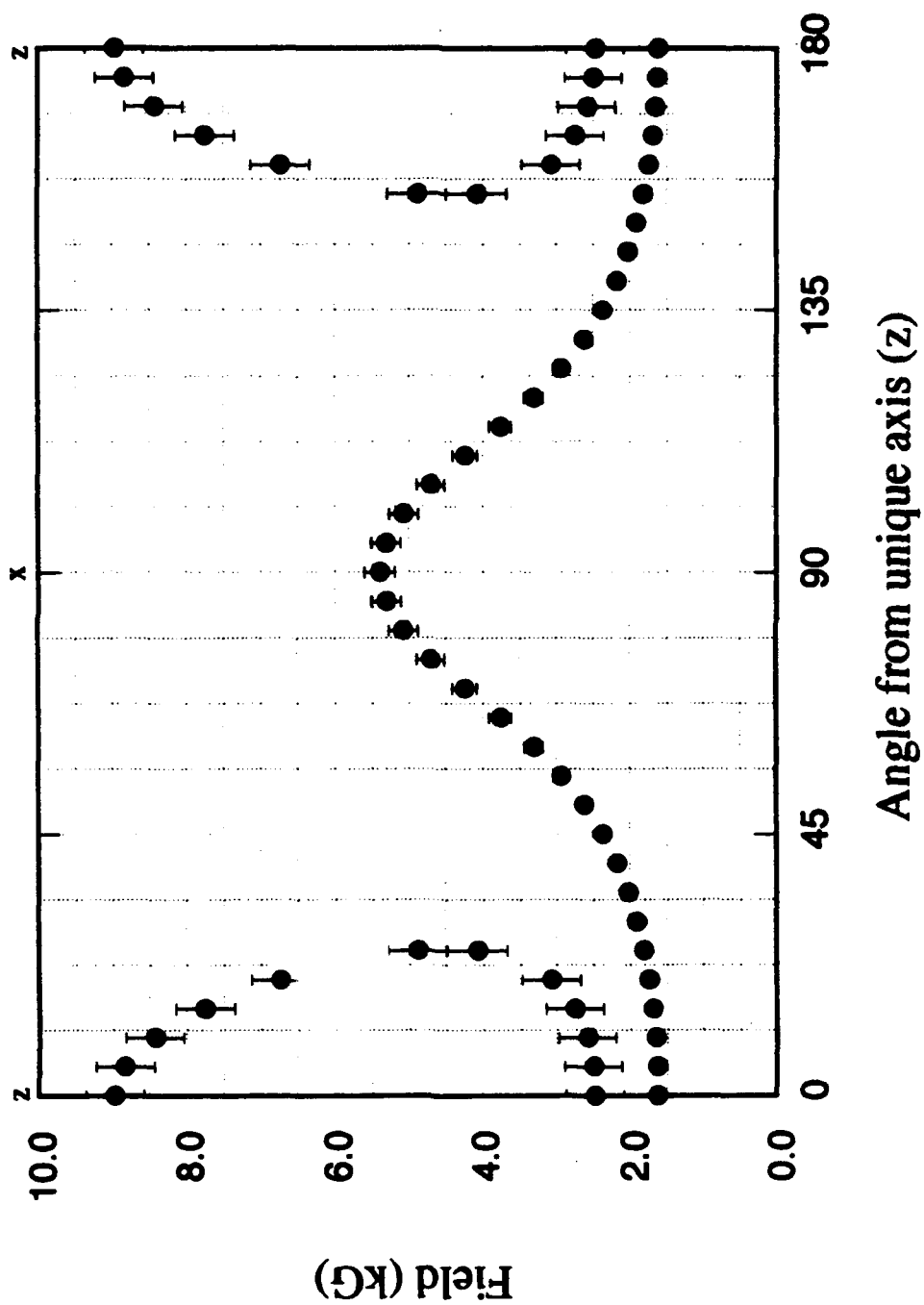
Spin 1 at 9.5 GHz  
 $D=2$  GHz,  $E=0.0$  GHz,  $g=2.0$



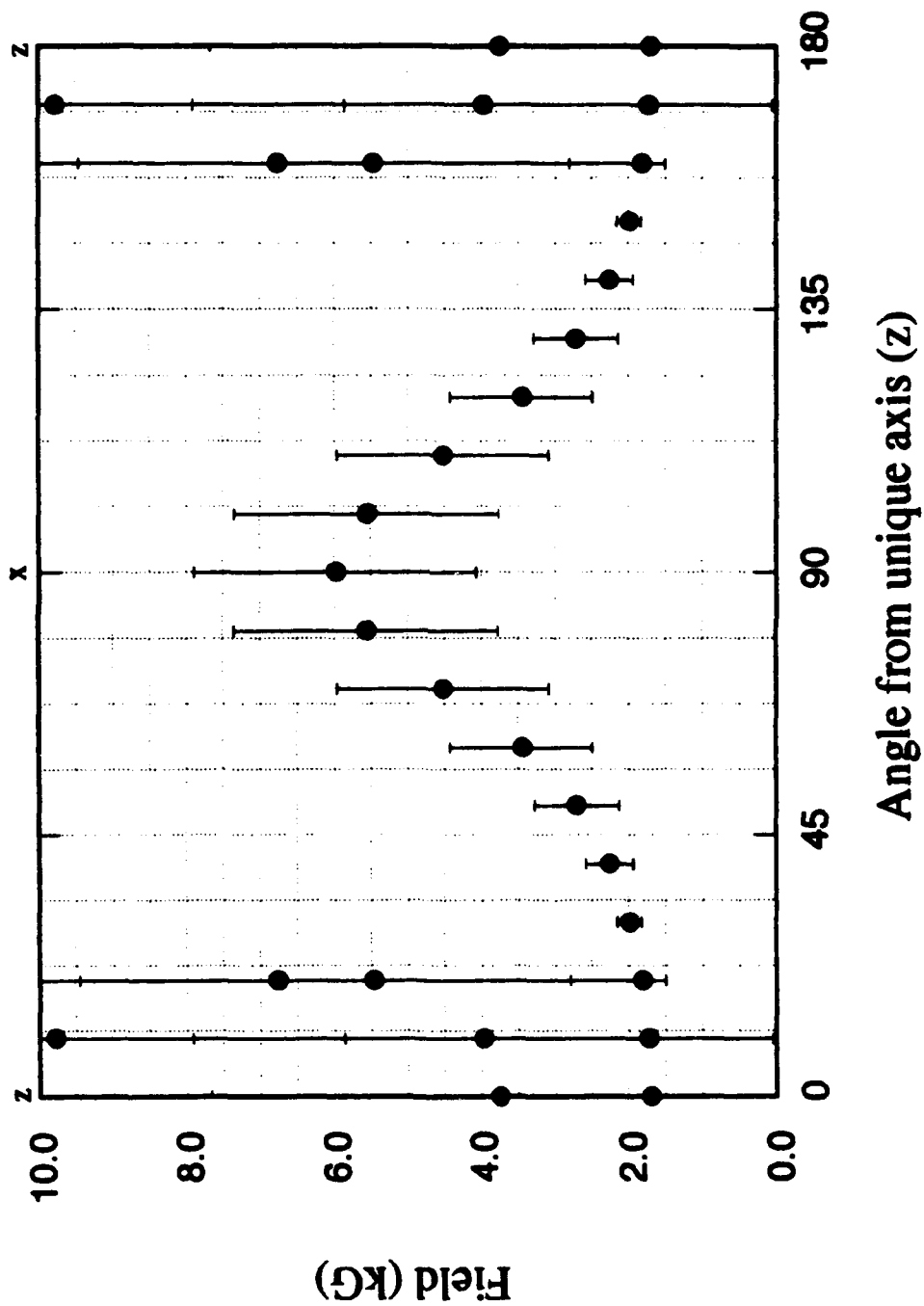
Spin 1 at 9.5 GHz  
 $D=3$  GHz,  $E=0.0$  GHz,  $g=2.0$



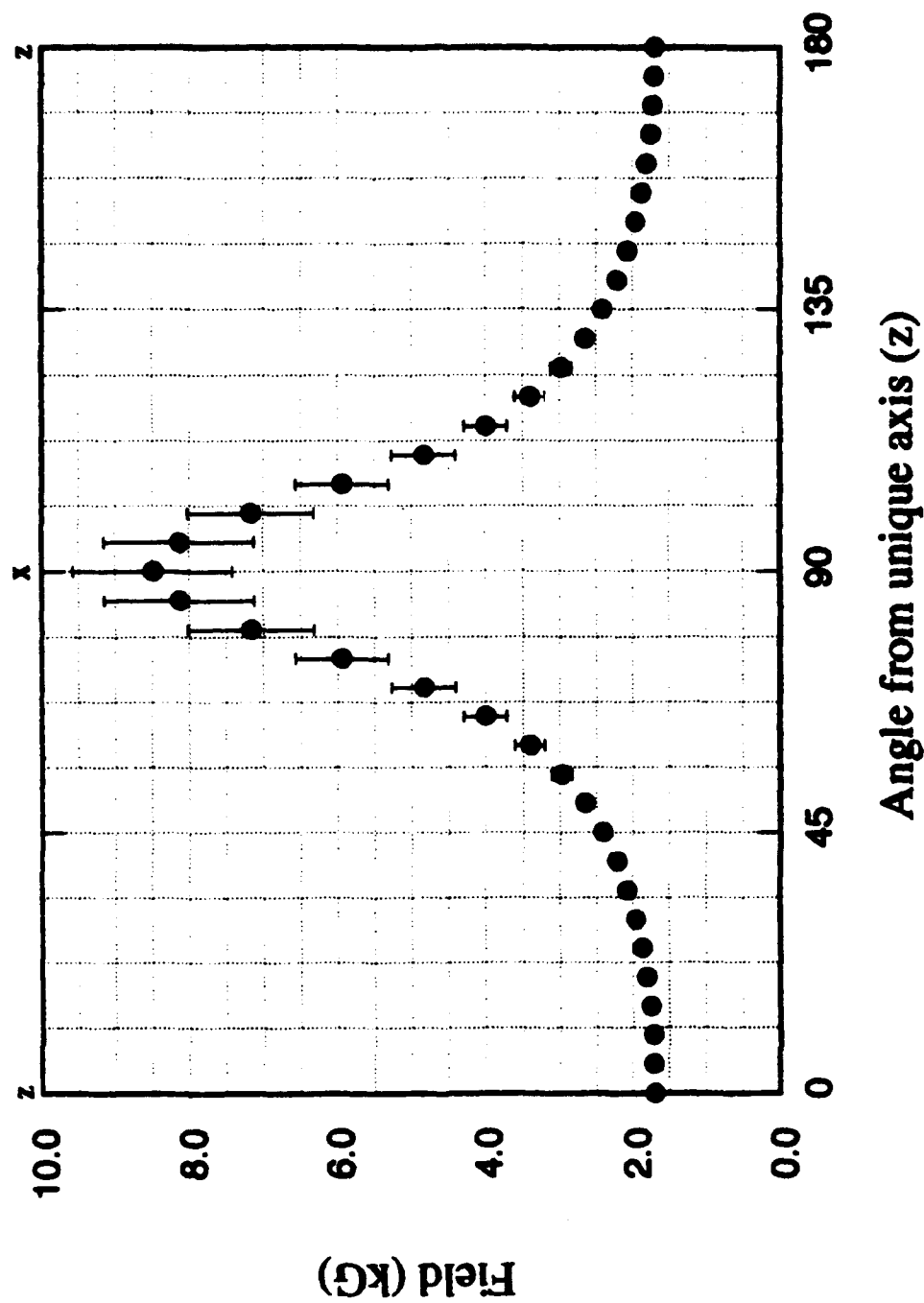
Spin 1 at 9.5 GHz  
 $D=16$  GHz,  $E=0.0$  GHz,  $g=2.0$



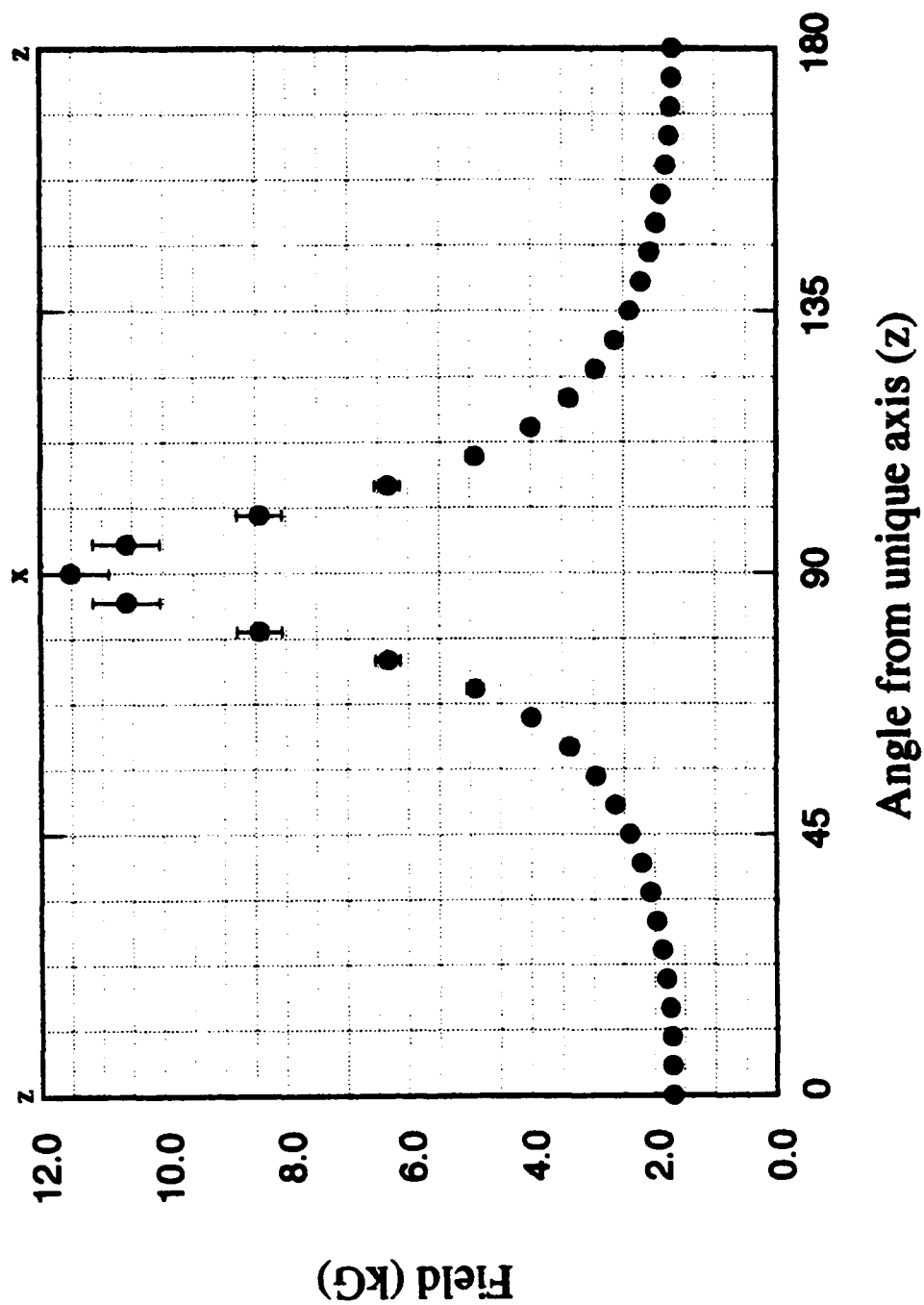
Spin 1 at 9.5 GHz  
 $D=20$  GHz,  $E=0.0$  GHz,  $g=2.0$



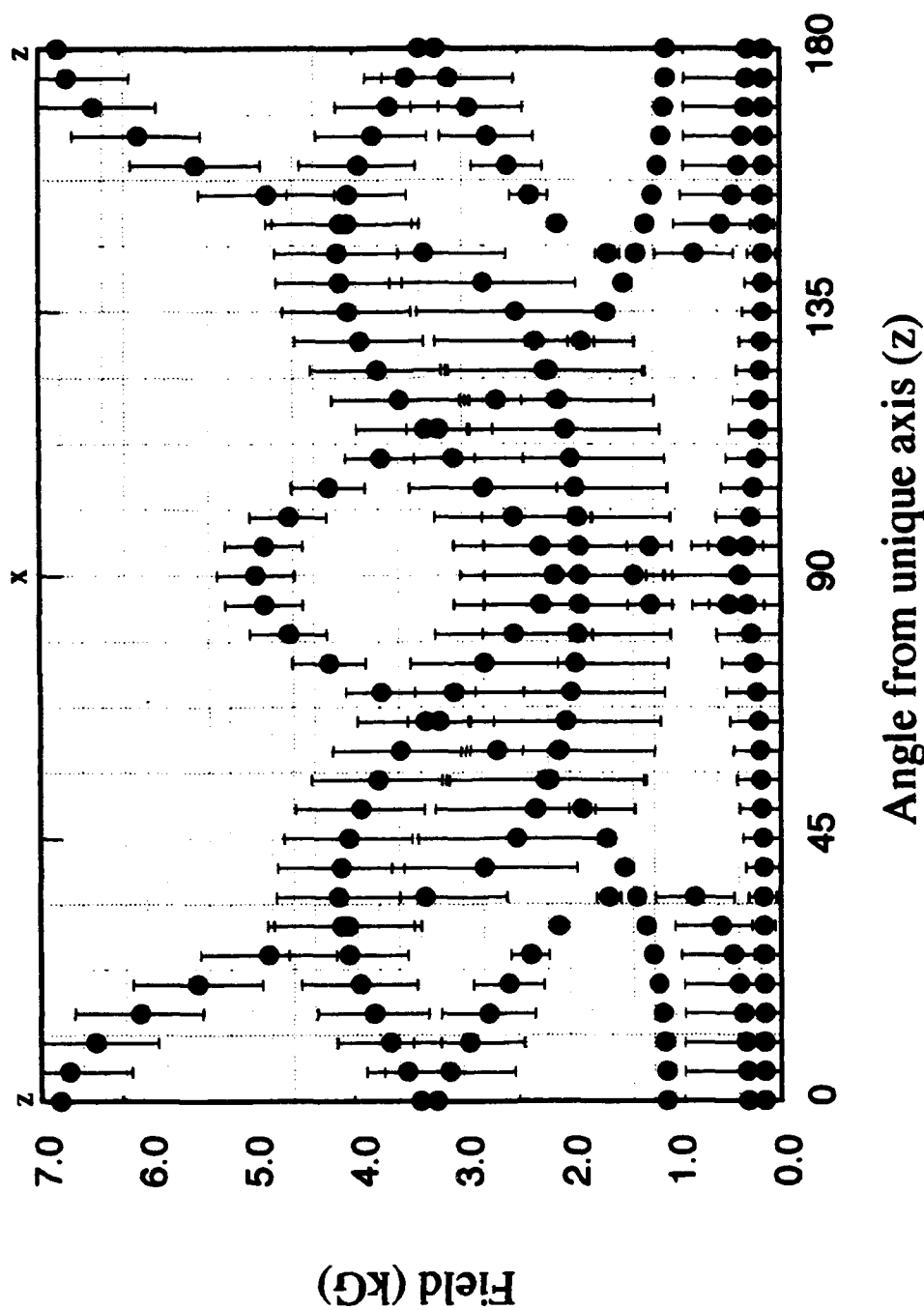
Spin 1 at 9.5 GHz  
 $D=50$  GHz,  $E=0.0$  GHz,  $g=2.0$



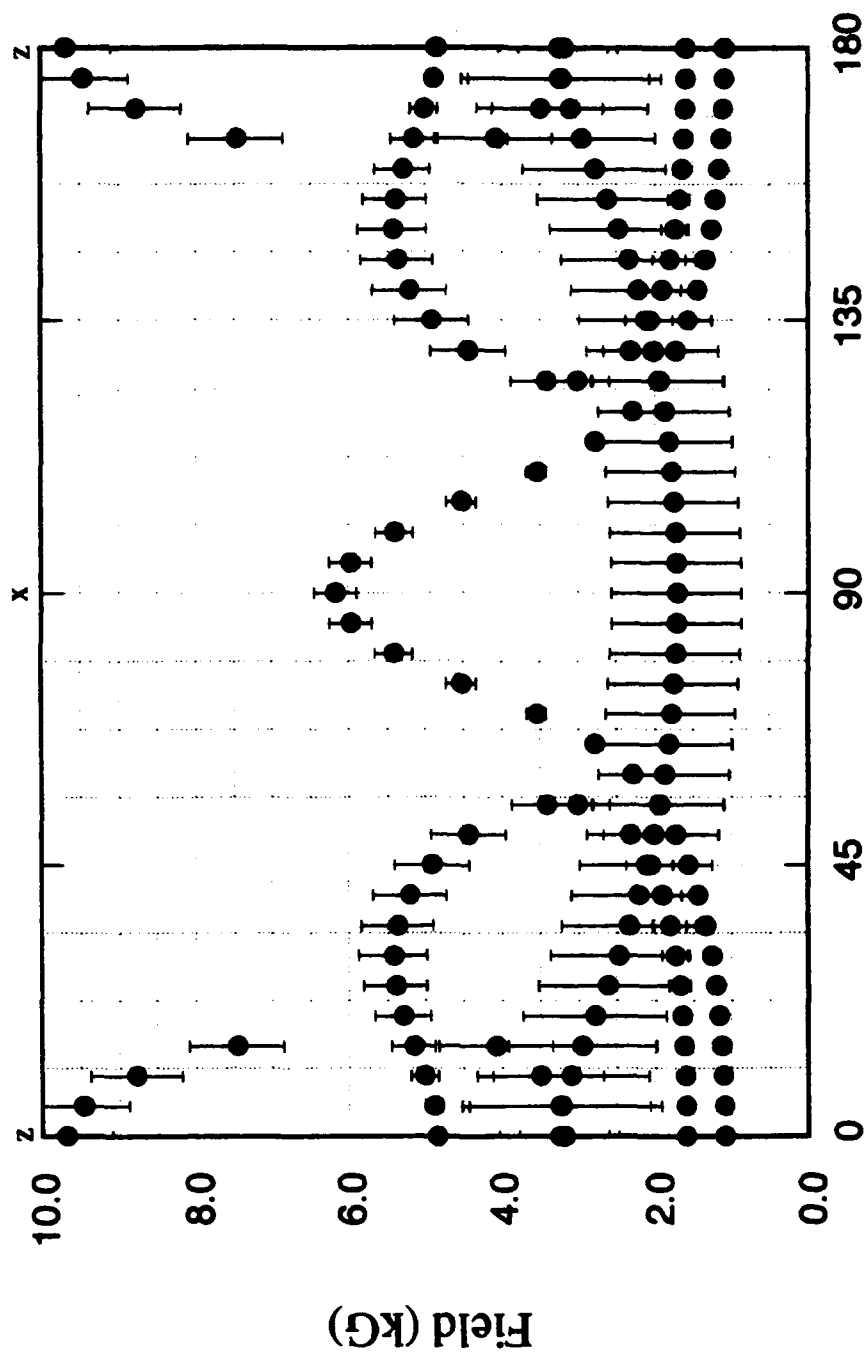
Spin 1 at 9.5 GHz  
 $D=100$  GHz,  $E=0.0$  GHz,  $g=2.0$



Spin 3/2 at 9.1 GHz  
 $D=5$  GHz,  $E=0.0$  GHz,  $g=2.0$



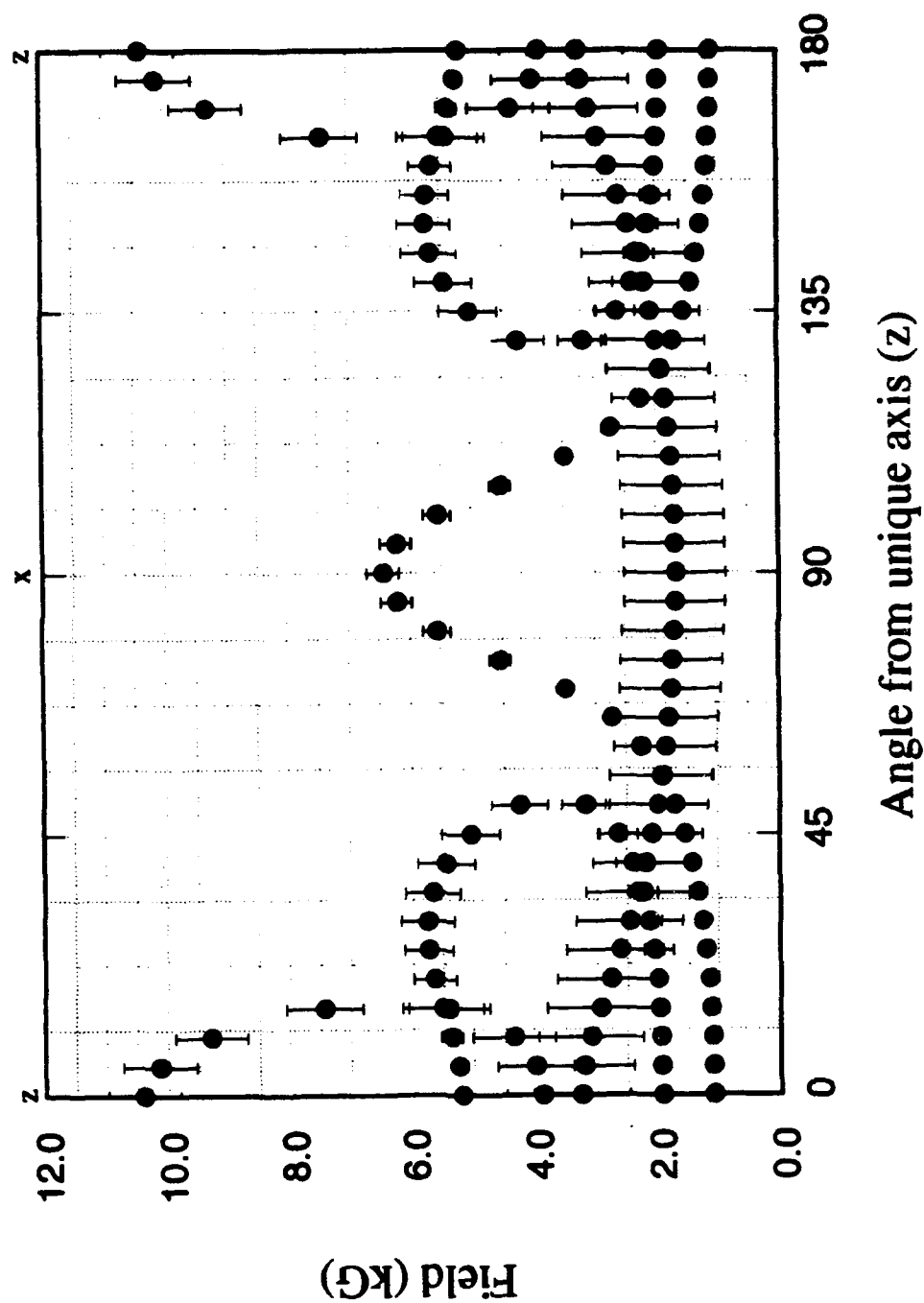
Spin 3/2 at 9.1 GHz  
 $D=9$  GHz,  $E=0.0$  GHz,  $g=2.0$



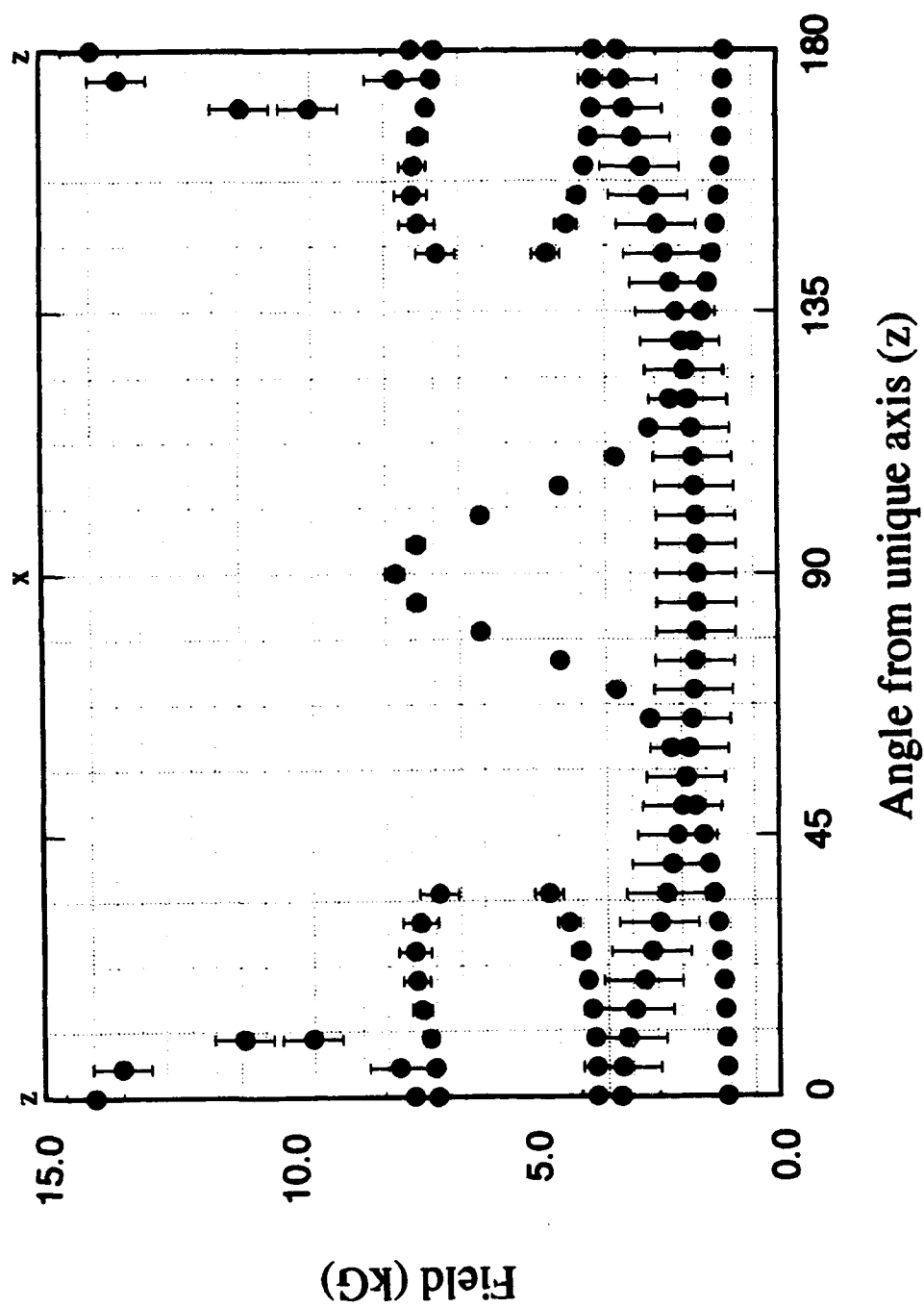
Angle from unique axis (z)



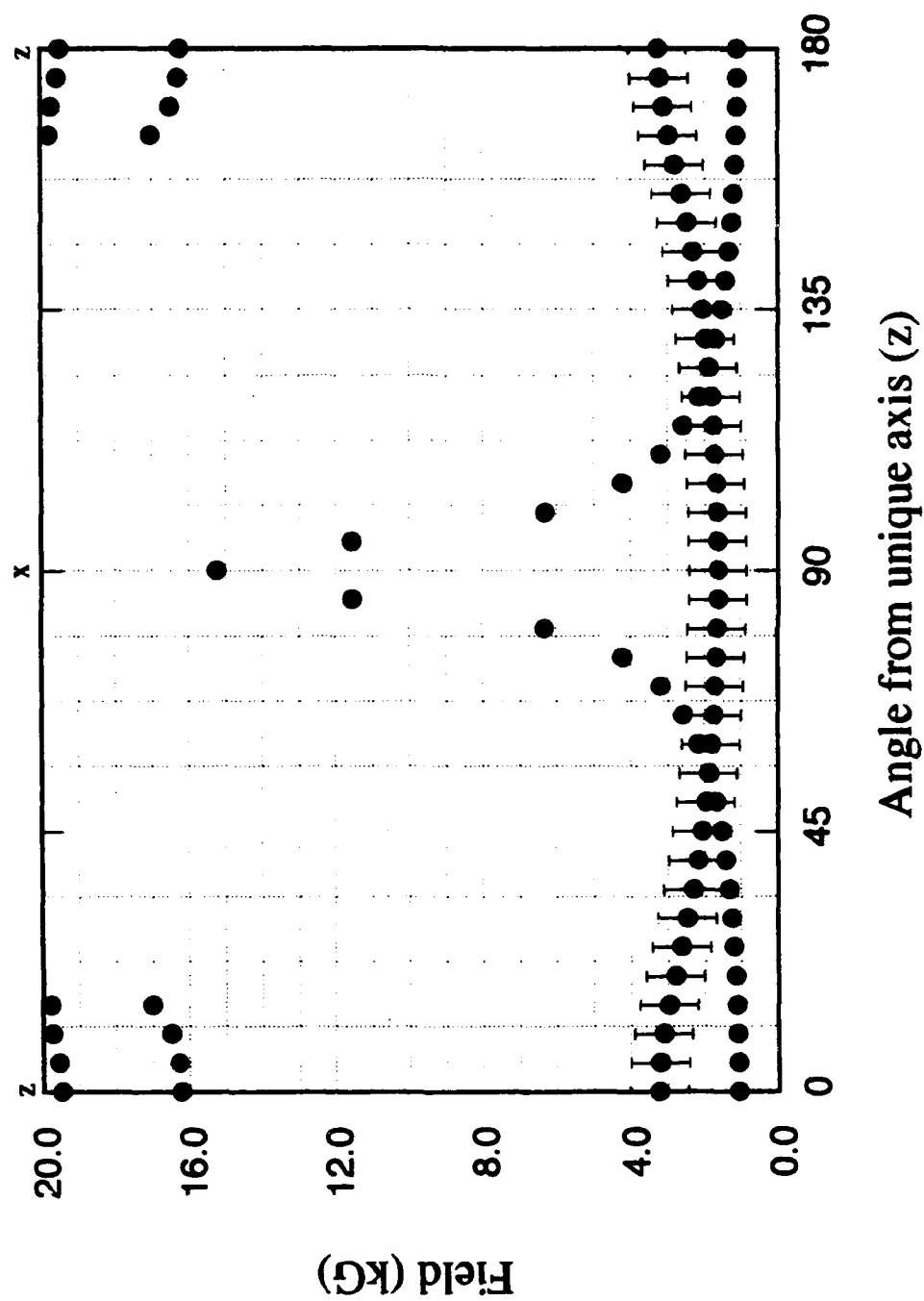
Spin 3/2 at 9.1 GHz  
 $D=10$  GHz,  $E=0.0$  GHz,  $g=2.0$



Spin 3/2 at 9.1 GHz  
 $D=15$  GHz,  $E=0.0$  GHz,  $g=2.0$



Spin  $3/2$  at 9.1 GHz  
 $D=50$  GHz,  $E=0.0$  GHz,  $g=2.0$



## REFERENCES

- [1] L.J. Schwoc and J.R.C. , J. Appl. Phys. **37**, 449 (1966).
- [2] G.I. Vetrogon, V.I. Danilenko, V.Y. Kabanchenko, V.V. Osiko, A.M. Prokhorov, A.N. Terent'evskii, and M.I. Timoscenchkin, Sov. Phys. Solid State. **24**, 434 (1982).
- [3] X. Bai and L. Zeng, Phys. Rev. B. **39**, 10 (1989).
- [4] E.A. Markosyan and O.S. Torosyan, Izv. Akad. Nauk. Arm. SSR Fiz. **9**, 229 (1974).
- [5] J.W. Carson and R.L. White, J. Appl. Phys. **32**, 1787 (1961).
- [6] S. Geschwind and J.M. Nielsen, Bull. Am. Phys. Soc. **5**, 252 (1960).
- [7] A.E. Nosenko, B.V. Padlyak, G.G. Krafnuk, and V.V. Kravchishin, Sov. Phys. Solid State. **25**, 1657 (1984).
- [8] W.B. Lewis, Appl. Phys. A**54**, 31 (1992).
- [9] M.H. Garrett, V.H.Chan, H.P. Jensen, M.H. Whitmore, A. Sacra, D.J. Singel, and D.J. Simkin, in *OSA Proceedings on Advanced Solid-State Lasers*, edited by G. Dubé and L. Chase (Optical Society of America, Washington, DC, 1991), Vol. 10, p. 76.
- [10] T.S. Rose, R.A. Fields, M.H. Whitmore, and D.J. Singel, in *OSA Proceedings on Advanced Solid-State Lasers*, edited by L.L. Chase and A.A. Pinto (Optical Society of America, Washington, DC, 1992), Vol. 13, p. 17.
- [11] M.H. Whitmore and D.J. Singel, J. Chem. Phys., in press.
- [12] T.S. Rose, M.H. Whitmore, R.A. Fields, and D.J. Singel, J. Am. Opt. Soc.:B, submitted for publication.
- [13] L.D. Merkle, A. Pinto, H.R. Verdún, and B. McIntosh, Appl. Phys. Lett. **61**, 2386 (1992).
- [14] M.H. Whitmore, H.R. Verdún, and D.J. Singel, Phys. Rev. B, in press.
- [15] N.B. Angert, N.I. Borodin, V.M. Garmash, V.A. Zhitnyuk, A.G. Okhrimchuk, O.G. Siyuchenko, and A.V. Shestakov, Sov. J. Quantum Electron. **18**, 73 (1988).
- [16] D.M. Andrauskas, L.M. Thomas, and H.R. Verdún, in *SPIE Technical Symposium on Aerospace Sensing*, (Orlando, Florida, 1989), p. 1104.
- [17] T.H. Allik, S.A. Stewart, D.K. Sardar, G.J. Quarles, R.C. Powell, C.A. Morrison, G.A. Turner, M.R. Kokta, W.W. Hovis, and A.A. Pinto, Phys. Rev. B. **37**, 9129 (1988).
- [18] J.B. Parise, R.L. Harlow, R.D. Shannon, G.H. Kwei, T.H. Allik, and J.T. Armstrong, J. Appl. Phys. **72**, 2152 (1992).
- [19] M. Tsukioka and H. Kojima, J. Phys. Soc. Jap. **35**, 818 (1973).
- [20] J.C.M. Henning, J. Liebertz, and R.P.V. Stapele, J. Phys. Chem. Solids **28**, 1109 (1967).

- [21] W. Mowat, A. Shortland, G. Yagupsky, N.J. Hill, M. Yagupsky, and G. Wilkinson, *J. C. S. Dalton* (7), 533 (1972).
- [22] E.C. Alyea, J.S. Basi, D.C. Bradley, and M.H. Chisholm, *Chem. Comm.*, 495 (1968).
- [23] D.J. Machin, D.F.C. Morris, and E.L. Short, *J. Chem. Soc.*, 4659 (1962).
- [24] D.H. Brown, *J. Chem. Soc.*, 3322 (1962).
- [25] I.S. Akhmadulin, V.A. Golenischev-Kutuzov, S.A. Migachev, A.G. Okhrimchuk, and A.V. Shestakov, *Sov. Phys. Solid State* 33, 2546 (1991).
- [26] W. Low and E.L. Offenbacher, *Electron Spin Resonance of Magnetic Ions in Complex Oxides: Review of ESR Results in Rutile, Perovskites, Spinel, and Garnet Structures*. pp. 186.
- [27] S. Geller, *Z. Kristal.* 125, 1 (1967).
- [28] S. Geschwind, *Phys. Rev.* 121, 363 (1961).

## Chapter 9

---

### **Characterization of Optical Centers in Mn:Ba<sub>3</sub>(VO<sub>4</sub>)<sub>2</sub> by Spin-Echo EPR Spectroscopy**

# Characterization of Optical Centers in $\text{Mn}:\text{Ba}_3(\text{VO}_4)_2$ by Spin-Echo EPR Spectroscopy

M.H. Whitmore, Christian T. Farrar

*Department of Chemistry Harvard University 12 Oxford Street,  
Cambridge, MA 02138*

B. Buysse, J. Coremans, and J. Schmidt

*Department of Physics, Huygens Laboratory, University of Leiden,  
Leiden, The Netherlands*

D.J. Singel

*Department of Chemistry Harvard University 12 Oxford Street, Cambridge, 02138*

## Abstract

Novel *cw*, time-resolved, and optical double resonance modes of EPR spectroscopy provide a detailed characterization of a new laser material,  $\text{Mn}:\text{Ba}_3(\text{VO}_4)_2$ . The presence of both  $\text{Mn}^{4+}$  and  $\text{Mn}^{5+}$  centers is shown by *cw* EPR spectroscopy. Spin-echo modulation effects provide experimental evidence that the manganese substitutes for vanadium at tetrahedral lattice sites. A new spin-echo optical double resonance technique is introduced to selectively probe the near IR absorption spectrum of the  $\text{Mn}^{5+}$  center, in order to prove that  $\text{Mn}^{5+}$  is the active ion.

## Introduction

The spectroscopic characterization of metal ions incorporated in insulator host crystals is an important source of information guiding the development of solid state lasers. The identification of active guest ions and their modes of incorporation into the host can play a critical role in enabling the development of materials with deliberately tailored optical properties. EPR (electron paramagnetic resonance) techniques - including both vintage single-crystal rotation methods and recently developed time-domain methods [1,2] - have proven to be well-suited to this task, and can be especially useful for materials designed for broad tunability: broadening of optical lines limits the utility of simple optical techniques. The lack of selectivity for optically active ions, however, can be a serious disadvantage of EPR in complex materials, and has motivated us to explore methods involving pulse laser, optical excitation and time-resolved, spin-echo EPR to correlate optical and paramagnetic centers. Here we report the detailed characterization of a new transition metal laser system,  $\text{Mn}:\text{Ba}_3(\text{VO}_4)_2$  [3], by the application of an array of EPR methods, including *cw*, pulsed, and optical double resonance techniques.

## Experimental Results and Discussion

Single crystals of  $\text{Ba}_3(\text{VO}_4)_2$  doped with manganese (0.25% by weight in the melt) were grown by laser heat pedestal growth method under an oxidizing atmosphere by Dr. H. R. Verdún of Fibertek, Inc. A  $\sim 4 \text{ mm}^3$  sample was used in all experiments described here.

An exemplary *cw* EPR spectrum is shown in Fig. 1. Four strong signals are evident, with characteristic multiplet structure from the coupling of the electron to the  $^{55}\text{Mn}$  nuclear moment. As detailed elsewhere [4], the variation of the resonant field strength as a function of field orientation reveals the presence of two distinct types of manganese paramagnetic centers.

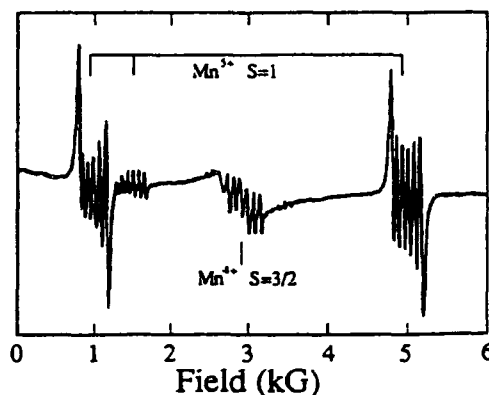


Figure 1. EPR spectrum of  $\text{Mn}:\text{Ba}_3(\text{VO}_4)_2$ . The spectrum was obtained with the magnetic field aligned with the crystal *c* axis at 9.09 GHz and ambient temperature. Multiplets assigned to the  $\text{Mn}^{4+}$  and  $\text{Mn}^{5+}$  centers are indicated.

One center, a spin triplet, is assigned to  $\text{Mn}^{5+}$ , while the second is a quartet spin,  $\text{Mn}^{4+}$  species. Both evidently substitute for cations at threefold symmetry sites in the  $\text{Ba}_3(\text{VO}_4)_2$  structure. Charge and size considerations ( $\text{Ba}^{2+}$ , 1.56 Å;  $\text{V}^{5+}$ , 0.50 Å;  $\text{Mn}^{5+}$  and  $\text{Mn}^{4+}$  0.47 and 0.53 Å, respectively) make substitution for  $\text{V}^{5+}$  more plausible, in which case the manganese ions would be lodged at tetrahedral sites.

We tested this conjecture experimentally by measuring the magnetic interaction of the guest ions with the  $^{51}\text{V}$  nuclei in the vanadate lattice. The technique used involves the spin-echo - a characteristic transient response of the electron spin system to resonant, pulsed (nsec) excitation. Sublevel structure from the coupled  $^{51}\text{V}$  appears as a quantum beat in the  $\text{Mn}^{5+}$  spin echo decay, as illustrated in Fig. 2. In the  $\text{Mn}:\text{Ba}_3(\text{VO}_4)_2$  system the beat occurs at the  $^{51}\text{V}$  Zeeman frequency (2.7 MHz) indicative of weak hyperfine coupling.

For such weakly coupled systems, the modulation amplitude varies as  $\langle n r^6 \sin 2\theta \rangle$ , where  $r$  is the Mn-V distance,  $\theta$  is the angle between the Mn-V line-of-centers and the external field, and  $n$  is the number of nuclei characterized by each  $(r, \theta)$  [1]. Because of the stark dependences on  $r$  and  $\theta$ , modulation effects often arise from a single shell of the neighboring nuclei

Our analysis of the time-domain waveform is consistent with assignment of the  $^{51}\text{V}$  Zeeman frequency modulation to the three second shell  $^{51}\text{V}$  nuclei that lie 4.6 Å from a  $\text{Mn}^{5+}$  ion hypothetically

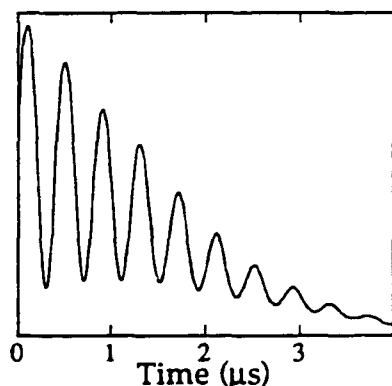


Figure 2. Spin Echo Decay with  $^{51}\text{V}$  Nuclear Modulation registered at 4.4 K by excitation of the  $\text{Mn}^{5+}$  EPR line at 9.23 GHz and 2303 G with the field along the  $a$  axis. The modulation occurs predominantly at the  $^{51}\text{V}$  Zeeman frequency (2.7 MHz).

situated at the tetrahedral,  $\text{V}^{5+}$  site [5]. This consistency provides additional support for the notion that  $\text{Mn}^{5+}$  substitutes for  $\text{V}^{5+}$  in  $\text{Ba}_3(\text{VO}_4)_2$ .

In order to prove that the  $\text{Mn}^{5+}$  is the laser center, we introduced a novel EPR-optical double resonance technique. We detect the spin-echo transient just after pulsed optical excitation within the narrow, near IR absorption band of the  $\text{Mn}:\text{Ba}_3(\text{VO}_4)_2$ , assigned by Merkle *et al.* [3] to the  ${}^3\text{A}_1\text{E}$  transition of tetrahedral  $\text{Mn}^{5+}$ .

Spin-echoes sample the population difference of electron spin levels on resonance. Laser induced optical transitions from the ground-state sublevels perturb the Boltzmann populations, and thus change the spin-echo amplitudes. This effect provides a means for EPR-selected optical excitation spectroscopy.

As the scanned excitation (Nd:YAG with Raman shifter) wavelength reaches the optical absorption, the spin-echo signal should decrease, as population is removed predominantly from the lower ground state spin sublevel, thereby decreasing the population difference between the resonant spin sublevels: conversely, at the high wavelength edge of the optical absorption the upper sublevel is preferentially depopulated and the echo signal should increase. A derivative spectral lineshape is thus expected.

This lineshape is evidenced in the experimental spectrum of Fig. 3, which otherwise reflects the position and width of the active ion absorption observed by Merkle *et al.* [3]. The spectrum in Fig. 3 (a light off/on difference spectrum) was obtained by scanning

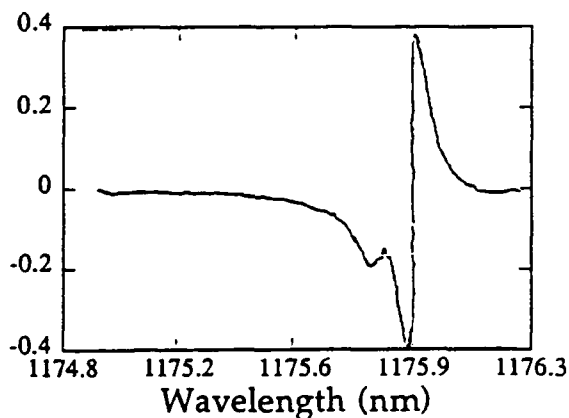


Figure 3.  $\text{Mn}^{5+}$ -selective near IR excitation spectrum of  $\text{Mn}:\text{Ba}_3(\text{VO}_4)_2$ , obtained, by the EPR-optical double resonance method described in the text, at 4.4 K with a field of 5160 G aligned with the  $c$  axis and EPR at 9.35 GHz. The delay between the optical and spin-echo excitation is 600 nsec, and the spin-echo interpulse delay is 350 nsec.



the near IR absorption while observing the high-field EPR signal of the  $S=1$ ,  $Mn^{5+}$  center with the external field (5160 G) along the crystal  $c$  axis (upper two triplet sublevels on EPR). The double resonance effect proves that the tetrahedral  $Mn^{5+}$  is the lasing ion.

The inherent time-resolved nature of this technique provides a route for gaining insight into the dynamics of the cycle of excitation and relaxation. For example, by scanning a delay interposed between the laser and microwave pulses [2], we have found that the recovery of the sublevels to thermal equilibrium is dominated by electron spin-lattice relaxation, not by the decay of the excited state. This observation rationalizes the presence of the additional spectral feature, in Fig. 3, at  $\sim 1175.8$  nm. When the lowest triplet sublevel (off EPR) is pumped by the laser pulse, some spin-lattice relaxation, predominantly from the middle sublevel, occurs. This relaxation (indirectly) decreases the probed population difference, and leads to a negative (difference) signal that occurs at  $\sim 10$  GHz to the high energy side of the trough of the main signal.

The feasibility of this type of pulsed EPR-optical double resonance experiment is contingent on high absorption cross-sections (to facilitate large, laser-induced changes the ground state populations), and sufficiently ( $>10^2$  nsec) long-lived excited states (to bottleneck the repopulating of the ground state). Paramagnetic centers that behave either as lasing centers or as saturable absorbers, increasingly used in Q-switch applications, can thus be probed. The other EPR methods - including both single crystal rotation methods and electron spin echo modulation techniques - are more broadly applicable for quantifying and characterizing paramagnetic centers regardless of their optical characteristics. They are therefore especially attractive for probing the nature radiation-induced or other extraneous defects that can affect laser performance.

#### Acknowledgements

The authors gratefully acknowledge Dr. H.R. Verdún of Fibertek Inc., who supplied the materials used in this work, Dr. A. Pinto of the Army Night Vision Laboratory for helpful discussions, and the Army Research Office, for support of this work through research grant DAAL-03-90-0113 (to DJS).

#### References

1. A. Schweiger, *Angew. Chem. Int. Ed.* 30, 265 (1991).
2. J. Schmidt and D.J. Singel, *Ann. Rev. Phys. Chem.*, 38, 141 (1987).
3. L. D. Merkle, A. Pinto, H.R. Verdún, B. McIntosh, *Appl. Phys. Lett.*, 61 2386 (1992).
4. M.H. Whitmore, H.R. Verdún, and D.J. Singel *Phys. Rev. B.*, 47 11479, (1993).
5. P. Süssé and M.J. Buerger, *Z. Kristallogr.* 131, 161 (1970).